Manuscript File Click here to view linked References

https://doi.org/10.1016/j.ijplas.2020.102918

This is the Pre-Published Version.

Constitutive modeling of size-dependent deformation behavior in nano-dual-phase glass-crystal alloys

Linli Zhu[1]*, Haihui Ruan[2], Ligang Sun[3], Xiang Guo[4], Jian Lu[5,6,7]

[1]Department of Engineering Mechanics, Key Laboratory of Soft Machines and Smart Devices of Zhejiang Province, Zhejiang University, Hangzhou 310027, Zhejiang Province, China

[2]Department of Mechanical Engineering, The Hong Kong Polytechnic University, Kong Kong, China

[3]School of Science, Harbin Institute of Technology, Shenzhen 518055, China

[4]School of Mechanical Engineering, Tianjin Key Laboratory of Nonlinear Dynamics and Control, Tianjin University, Tianjin 300072, China

[5]Department of Mechanical Engineering, City University of Hong Kong, Hong Kong, China.

[6]Hong Kong Branch of National Precious Metals Material Engineering Research Center (NPMM), City University of Hong Kong, Hong Kong, China

[7]Center for Advanced Structural Materials, City University of Hong Kong Shenzhen Research Institute, Greater Bay Joint Division, Shenyang National Laboratory for Materials Science, Shenzhen, China

---

* Author to whom correspondence should be addressed; E-mail: llzhu@zju.edu.cn (Linli Zhu)

© 2020. This manuscript version is made available under the CC-BY-NC-ND 4.0 license http://creativecommons.org/licenses/by-nc-nd/4.0/

Abstract

Nano-dual-phase glass-crystal (NDPGC) metallic materials as the novel nanostructured materials have been proved experimentally to possess excellent mechanical properties, e.g. the nearly ideal strength. The present work is concerned with the constitutive analysis of size-dependent deformation behaviors in micropillars of a NDPGC alloy based on the micromechanics approach. The mechanism-based constitutive models are developed to explore the sample-size dependent mechanical behaviors of NDPGC pillars. An energy-based criterion for shear-band nucleation is employed to predict the diameter-dependent number of shear bands in large micropillars subjected to compression. The flow activation in metallic glass, grain reorganization, and grain refinement are involved in the proposed constitutive model for small micropillars. Numerical results demonstrate that the proposed theoretical model can describe the constitutive behaviors of the Mg-based NDPGC alloy. Good agreements between the theoretical and experimental results are achieved for the stress-strain relations and the diameter-dependent number of shear bands in large micropillars. It is found that the critical pillar diameter for generating shear bands increases with grain size and that the yield strength of NDPGC micropillars increases with the reduction in grain size (from 50 to 10 nm) without causing the inverse Hall-Petch effect. Therefore, a good combination of high yield strength and excellent plasticity can be achieved with small micropillars under compression. These findings show that the proposed model can be applied to optimize the mechanical performance of NDPGC alloys by controlling the microstructural size and sample (or feature) size.

Keywords: Nano-dual-phase glass-crystal alloys; Micropillars; Constitutive model; Yield strength; Plasticity; Metallic glass flow; Grain size.

1. Introduction

Advanced metallic materials, widely used in the chemical, transportation, and aerospace industries (Rashid, 1981; Llewellyn and Hillis, 1996; Zinkle and Busby, 2009; Lu, 2010; Bouaziz et al., 2013), play a significant role in infrastructural and economic development (Ashby, 1999; Militzer, 2002; Davis et al., 2013). For most engineering applications, excellent mechanical properties—such as ultrahigh strength (e.g., close to the theoretical value) or a good combination of yield strength and ductility—are hoped for. It is however very challenging to have a material with nearly ideal strength (close to the theoretical value) especially when the sample or feature size is beyond nanoscale (Zhu and Li, 2010, Sun et al., 2020) because the enrichment of structural defects such as dislocations, voids, and impurities results in a yield strength far below the ideal strength of the material. Even though single-crystal whiskers, crystalline nanowires, and nanometre-sized metallic glasses (MG) with inhibited defects possess a nearly ideal strength (Richter et al., 2009; Deng and Sansoz, 2009; Tian et al., 2012), the complicated fabrication method and nano-sized feature obstruct practical applications. On the other hand, to meet the demands for the advanced metallic materials in energy-efficient and environmentally-benign engineering systems (Bleck, 1996; Frommeyer et al., 2003; De Cooman et al., 2011), it becomes another challenge to balance the mechanical properties between formability, strength, and hardening capacity. Strengthening is easy to achieve through various traditional methods such as the grain refinement, cold working, alloying, as well as the phase transformation; However, these methods are accompanied invariably with the loss of ductility and work-hardening capability (Meyers et al., 2006; Dao et al., 2007; Bouaziz et al., 2011; Kou et al., 2014). Since the mechanical properties of materials are dominated by the characteristic microstructures which are associated with the interactions between various microstructural defects, the key question in metallurgy, remaining unanswered, is how to design the microstructures to achieve a desired mechanical property, e.g., to overcome the strength-ductility tradeoff (Zhu and Liao, 2004; Ritchie, 2011; Ma and Zhu, 2017).

Many experimental studies based on the paradigm of defect engineering have indicated that refining grain size or generating nanoscale twins can effectively strengthen materials (Meyers et al., 2006; Hahn and Meyers, 2015; Lu et al., 2004; Lu et al., 2009; Tian et al., 2013; Huang et al., 2014; Beyerlein et al., 2014; Li and Lu, 2017) and that the effect of feature size, either grain size or twin spacing, follows the Hall-Petch relation (Lu et al., 2004; Pande and Cooper, 2009; Li et al., 2016; Sun et al., 2018). However, these approaches do not lead to a strength close to the ideal strength of the concerned material, instead, softening occurs when the microstructural size is below 10-15 nm, known as the inverse Hall-Petch effect (Schuh et al., 2002; Schioz and Jacobsen, 2003; Trelewicz and Schuh, 2007; Li et al., 2010; Wei, 2011; Zhu et al., 2011). The inverse Hall-Petch behavior comes from the transition of deformation mechanisms. In nanograined metals there exits the transition from dislocation motions to grain boundary activities or grain rotations (Trelewicz and Schuh, 2007; Pande and Cooper, 2009; Lim et al., 2011; Naik and Walley, 2020). In nanotwinned polycrystalline metals, dislocation-mediated deformation is replaced by the interactions between partial dislocations and twin boundaries when the twin spacing is less than a critical size (Dao et al., 2007; Li et al., 2010; Zhu et al., 2011; Tucker and Foiles, 2015). To mitigate the inverse Hall-Petch effect, grain-boundary engineering was proposed, which are essentially the approaches to stabilize grain boundaries, such as the grain-boundary relaxation (Rupert et al., 2012), texturing (Chen et al., 2012; Liu et al, 2013), and impurity segregation (Yu et al, 2017). Moreover, it has been found that high pressure can effectively stabilize grain boundaries, leading to the extension of the Hall-Petch relation into 3-nm nanograined metals without the occurrence of the inverse Hall-Petch effect (Zhou et al., 2020). Alternatively, a nanograined alloy can also be prepared through crystallizing the amorphous counterpart, in which grain boundaries may inherit the original amorphous arrangement with high stability. Such a material is called nano-dual-phase glass-crystal (NDPGC) alloy to emphasize the importance of the stable amorphous phase between nanocrystals (Wu et al., 2017; Sun et al., 2020).

Great efforts have also been carried out to achieve both high strength and high ductility in advanced metallic materials (Zhu and Liao, 2004; Ritchie, 2011; Ma and Zhu, 2017; Ovid’ko et al., 2018; Wu and Fan, 2020). To overcome the strength-ductility trade-off, many efforts were spent on optimizing microstructures, such as embedding the nanoscale twins in grains of a polycrystalline metal (Dao et al., 2007; Lu et al., 2009), generating a bi/multi-modal microstructure (Wang et al., 2002; Zhao et al., 2008; Simchi and Simchi, 2009; Farbaniec et al., 2014), achieving a hierarchical nanostructures (Liddicoat et al., 2010; Wei et al., 2014; Shin et al., 2016; Liu et al., 2018; Ming et al., 2019), or introducing gradient microstructures (Chen et al., 2011; Lu, 2014; Wu et al., 2014; Tan et al., 2015; Hasan et al., 2019). These approaches are applicable owing to the following mechanisms (Li et al., 2016; Hirth et al., 2016; Sun et al., 2018; Cao et al., 2018; Ovid'ko et al., 2018): (i) the high density of nanoscale twins provides additional obstacles preventing the dislocation motions, and the interaction between dislocations and twin boundaries, which allows partial penetration, is beneficial to ductility (Froseth et al., 2004; Zhu et al., 2007; Jin et al., 2008; Zheng et al., 2009; Tucker and Foiles, 2015; Chowdhury et al., 2016), and (ii) a reasonable distribution of both small and large grains leads to a balanced strength and ductility, in which nano-sized microstructures lead to strengthening and micro-sized ones delays the formation of large cracks (Fan et al., 2006; Lee et al., 2010; Fang et al., 2011; Lu, 2014; Wu et al., 2014; Tan et al., 2015; Yang et al., 2016). The corresponding theoretical models including mechanism-based plastic models (Jiang and Weng, 2004; Barai and Weng, 2009; Guerses and El Sayed, 2011; Gu et al., 2011; Zhu and Lu, 2012; Li et al., 2017; Zhu et al., 2017, 2019) and crystal plasticity models (El Kadiri and Oppedal, 2011; Mirkhani and Joshi, 2011; Aoyagi et al., 2014; Khan and Liu, 2016; Yuan et al., 2019; Haouala et al., 2020; Lu et al., 2020; Chen et al., 2020) have been developed to describe the deformation behavior and predict the mechanical properties in these advanced metallic materials.

Recently, an experimental study of Mg-based NDPGC alloy showed that the micropillars of this alloy possess ultrahigh yield strength and excellent plasticity under compression (Wu et al., 2020a), which indicates that achieving an NDPGC microstructure is an alternative approach to overcome the dilemma of strength and ductility. In addition, it was reported that the yield strength of the Mg-based NDPGC alloy was close to the ideal strength and that the increase of pillar diameter from the submicron scale to microscale led to a ductile to brittle transition. These new phenomena call for a mechanism-based constitutive model for NDPGC alloys, which will be described in the following text. The outline of the present work is as follows. The next section (Section 2) is to summarize the experimental observations for the Mg-based NDPGC alloy. Section 3 presents a micromechanics-based model to describe the constitutive behavior in NDPGC alloys and an energy-based criterion for generating the shear bands. Section 4 addresses the hierarchically micromechanical models for smaller-sized pillars based on the deformation mechanism. The comparisons between the theoretical and experimental results and the related discussions are provided in Section 5, followed by a conclusion.

2. Experimental observations

Mg-based NDPGC alloys with the nanoscale crystalline and glassy phases can be prepared through magnetron sputtering and appropriate annealing. This work concerns the Mg-based NDPGC alloy experimentally studied in the early

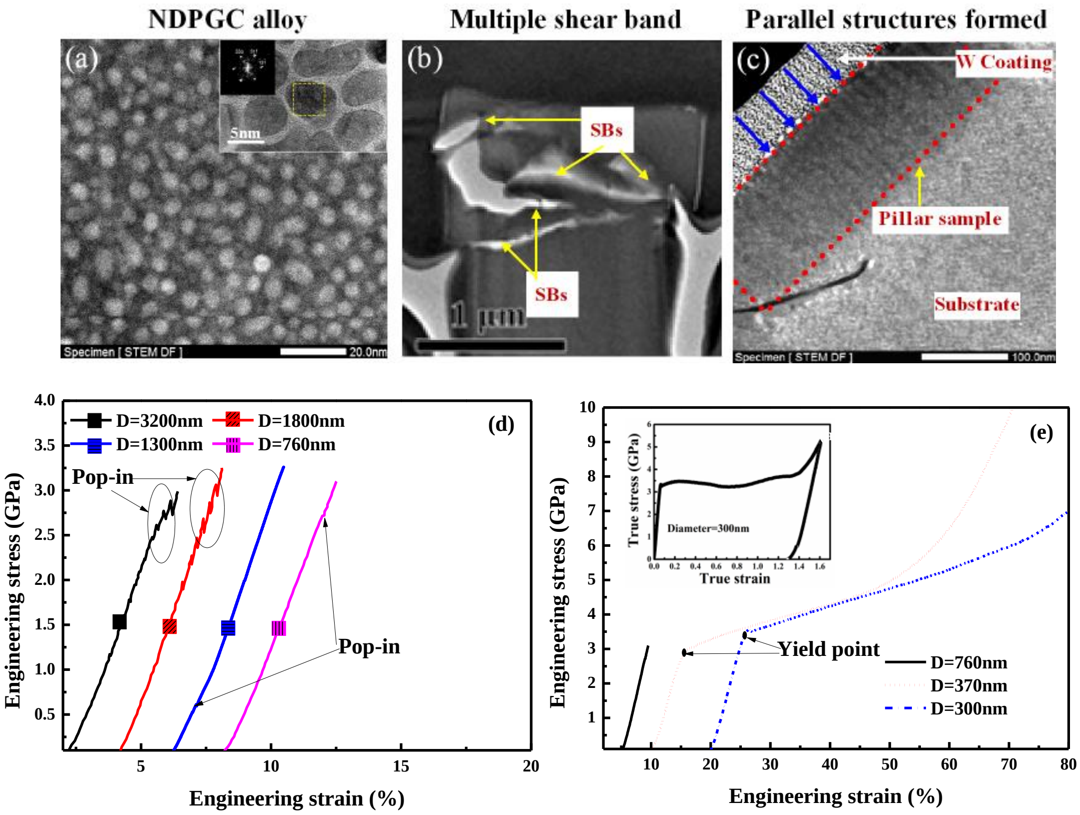

Figure 1. Transmission electron microscopy (TEM) images of (a)homogenous distribution of nanograins in the MG matrix, (b) the multiple shear bands in a larger micropillar, and (c) the cross-sction of a significanlly compressed small pillar exhibiting parallely arranged nanocrystals, where the blue arrowhead represents the compression direction. The stress-strain curves shown in (d) and (e) were obtained by compressing micropillars of Mg-based NDPGC alloy with different diameters (D), which shows brittle and ductile behaviors, respectively. The yield strength is defined as the stress at 0.2% plastic strain for the micropillars showing plasticiy.

publications (Wu et al., 2017, 2020a; Sun et al., 2020), where the average size of nanograins is 6 nm and the thickness of the MG phase around 2 nm, as exemplified in

Fig. 1(a). The corresponding compression tests of micropillar samples demonstrated distinct mechanical behaviors when the sample size changes. The pillars with diameters larger than 760 nm (large pillars) possess nearly ideal strength but no plasticity. There are pop-in behaviors in the stress-strain curves of these large pillars and the number of pop-in increases with the sample size, as shown in Fig. 1(d). **Note that each pop-in corresponds to the formation of a shear band running across the pillar, leading to a sudden increase in strain. Such a diameter-dependent pop-in number indicates that the transition of deformation mechanism will happen when pillar diameter reduces, i.e., the shear band running across a pillar could vanish when the pillar diameter is sufficiently small. This is indeed the case as small pillars exhibit large ductility.** For example, the small pillars with diameters of 370 and 300 nm (or more generally with diameters smaller than 500 nm) possess both ultrahigh yield strength and excellent plasticity, as shown in Fig. 1(e).

It is supposed that the nearly ideal strength comes from the homogenous flow behavior in the nanosized MG phase. In this deformation process, multiple shear bands may generate during deformation as shown in Fig. 1(b) (Wu et al., 2017, 2020). **Note that because the the lower density (atoms are more alienated) in shear bands after the severe deformation, shear bands in a TEM image appear brighter as shown in Fig. 1(b).** These localized deformation bands may accumulate and covalence, resulting in a global crack and the brittle behavior in the large pillars. However, in small pillars exhibiting large plasticity, the plastic flow in the MG phase is homogenous and free of shear band; instead, it results in the reorganization, migration, and even refinement of nanograins. This is evident by the parallelly arranged nanograins after the pillar is significantly compressed, as shown in figure 1(c).

Motivated by these experimental observations, we propose a constitutive model to describe the plastic flow in the MG phase and a criterion to evaluate the condition of transition from shear banding to homogenous deformation when sample size reduces. The model can describe the observed mechanical behaviors and predict the size-dependent deformation behavior of NDPGC alloys.

3. Theoretical model for larger micropillars of NDPGC alloy

3.1 Micromechanical model of NDPGC alloy

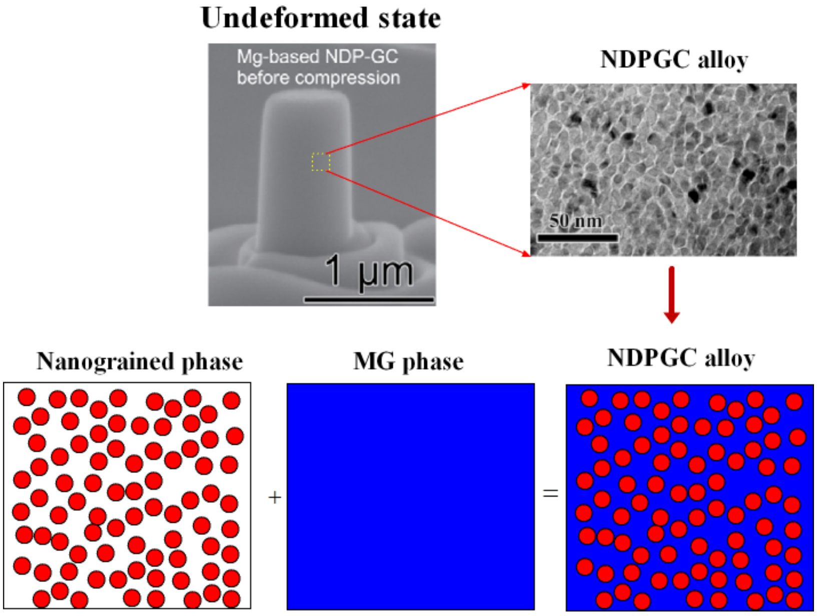
Undeformed state
Mg-based NDP-GC
before compression
1 µm
NDPGC alloy
50 nm
Nanograined phase
+
MG phase
=
NDPGC alloy

Figure 2. Schematic drawings of the composite structure model for the NDPGC alloys, consisting of nanosized crystals and MG phase with feature dimensions (size and spacing of nanocrystals) less than 10 nm.

Experimental observations demonstrated that nanocrystals distribute uniformly in the MG matrix in the concerned NDPGC alloy as shown in Figs. 1(a) and 2. Therefore, a NDPGC alloy can be treated as a composite material, in which the matrix and the reinforcing phase are MG and nanocrystals respectively, as shown schematically in Fig. 2. Because the crystalline and MG phases can be plastically deformed, the micromechanical model developed by G. Weng (1990) can be adopted to rationalize the stress-strain relation of NDPGC alloys. It is a modified mean-field model based on Hill’s recognition of weakening constraint power and the Mori-Tanaka approach that deals with inclusion-inclusion interactions. This model has been employed to describe various dual-phase metallic materials, which agrees well with experimental results (Zhu and Lu, 2012; Zhu et al., 2017, 2019). Based on this micromechanical framework, stress-strain relations can be expressed as:

$$\begin{aligned} \bar{\sigma}_{kk} &= 3\kappa_{\mathrm{G}}\left[1+\frac{c_{\mathrm{C}}(\kappa_{\mathrm{C}}-\kappa_{\mathrm{G}})}{c_{\mathrm{C}}\alpha_{\mathrm{C}}^{s}(\kappa_{\mathrm{C}}-\kappa_{\mathrm{G}})+\kappa_{\mathrm{G}}}\right]\bar{\varepsilon}_{kk}, \\ \bar{\sigma}'_{ij} &= 2\mu_{\mathrm{G}}^{s}\left\{\left[1+\frac{c_{\mathrm{C}}(\mu_{\mathrm{C}}-\mu_{\mathrm{G}}^{s})}{c_{\mathrm{G}}\beta_{\mathrm{G}}^{s}(\mu_{\mathrm{C}}-\mu_{\mathrm{G}}^{s})+\mu_{\mathrm{G}}^{s}}\right]\bar{\varepsilon}'_{ij}-\frac{c_{\mathrm{C}}\mu_{\mathrm{C}}}{c_{\mathrm{G}}\beta_{\mathrm{G}}^{s}(\mu_{\mathrm{C}}-\mu_{\mathrm{G}}^{s})+\mu_{\mathrm{G}}^{s}}\varepsilon_{ij}^{p(\mathrm{C})}\right\} \end{aligned} , \qquad (1)$$

where, $\bar{\sigma}_{kk}$ and $\bar{\sigma}'_{ij}$ are effective dilatational and deviatoric stresses, respectively, $\bar{\varepsilon}_{ij}$ effective strains, c_i the volume fraction with i being G or C pertaining to the glass or crystalline phase, respectively, α_i^s and β_i^s the components of Eshelby’s tensor for spherical inclusions denoted by $S_i^s = (\alpha_i^s, \beta_i^s)$ with $\alpha_i^s = (1+v_i^s)/3(1-v_i^s)$ and $\beta_i^s = 2(4-5v_i^s)/15(1-v_i^s)$. The relations between the hydrostatic and deviatoric strains of the constituent phases and the effective ones of the composite are given by:

$$\varepsilon_{kk}^{(\mathrm{G})}=\frac{\alpha_{\mathrm{G}}^{s}(\kappa_{\mathrm{C}}-\kappa_{\mathrm{G}})+\kappa_{\mathrm{G}}}{c_{\mathrm{G}}\alpha_{\mathrm{G}}^{s}(\kappa_{\mathrm{C}}-\kappa_{\mathrm{G}})+\kappa_{\mathrm{G}}}\bar{\varepsilon}_{kk},\ \varepsilon_{kk}^{(\mathrm{C})}=\frac{\kappa_{\mathrm{G}}}{c_{\mathrm{G}}\alpha_{\mathrm{G}}^{s}(\kappa_{\mathrm{C}}-\kappa_{\mathrm{G}})+\kappa_{\mathrm{G}}}\bar{\varepsilon}_{kk}$$
$$\varepsilon_{ij}^{(\mathrm{G})\prime}=\frac{\beta_{\mathrm{G}}^{s}(\mu_{\mathrm{C}}-\mu_{\mathrm{G}}^{s})}{c_{\mathrm{G}}\beta_{\mathrm{G}}^{s}(\mu_{\mathrm{C}}-\mu_{\mathrm{G}}^{s})+\mu_{\mathrm{G}}^{s}}\bar{\varepsilon}_{ij}'-\frac{c_{\mathrm{G}}\beta_{\mathrm{G}}^{s}\mu_{\mathrm{C}}}{c_{\mathrm{G}}\beta_{\mathrm{G}}^{s}(\mu_{\mathrm{C}}-\mu_{\mathrm{G}}^{s})+\mu_{\mathrm{G}}^{s}}\varepsilon_{ij}^{p(\mathrm{C})}\quad , \tag{2}$$
$$\varepsilon_{ij}^{(\mathrm{G})\prime}=\frac{\mu_{\mathrm{G}}^{s}}{c_{\mathrm{G}}\beta_{\mathrm{G}}^{s}(\mu_{\mathrm{C}}-\mu_{\mathrm{G}}^{s})+\mu_{\mathrm{G}}^{s}}\bar{\varepsilon}_{ij}'+\frac{c_{\mathrm{G}}\beta_{\mathrm{G}}^{s}\mu_{\mathrm{C}}}{c_{\mathrm{G}}\beta_{\mathrm{G}}^{s}(\mu_{\mathrm{C}}-\mu_{\mathrm{G}}^{s})+\mu_{\mathrm{G}}^{s}}\varepsilon_{ij}^{p(\mathrm{C})}$$

where $\kappa_i = E_i / 3(1-2v_i)$ and $\mu_i = E_i / 2(1+v_i)$ with E_i and v_i (i = G, C) being the elastic modulus and Poisson's ratio of the *i*th phase respectively, $\varepsilon_{ij}^{p(\mathrm{C})}$ is the plastic strain of the crystalline phase, $\varepsilon_{ij}^{(\mathrm{G})}$ and $\varepsilon_{ij}^{(\mathrm{C})}$ are strains of MG and crystalline phases, respectively.

We assume that the secant bulk and shear moduli of the *i*th phase satisfy the isotropic relations:

$$k_i^S = \frac{E_i^S}{3(1-2v_i^S)},\ \mu_i^S = \frac{E_i^S}{2(1+v_i^S)}. \tag{3}$$

Employing the secant moduli approach, the secant Young's moduli and secant Poisson's ratio of the *i*th phase can be written as

$$E_i^S = \frac{\sigma^{(i)}}{\varepsilon^{e(i)}+\varepsilon^{p(i)}} = \frac{E_i}{1+\frac{E_i\varepsilon^{(i)}}{\sigma_{flow}^{(i)}}\left(\frac{\sigma_{11}^{(i)}}{\sigma_{flow}^{(i)}}\right)^{m_0-1}},\ v_i^S = \frac{1}{2}-\left(\frac{1}{2}-v_i\frac{E_i^S}{E_i}\right). \tag{4}$$

3.2 Constitutive relations in MG phase and crystalline phase

We assume that the total strain rate $\dot{\boldsymbol{\varepsilon}}$ can always be written as:

$$\dot{\boldsymbol{\varepsilon}} = \dot{\boldsymbol{\varepsilon}}^{\mathbf{e}} + \dot{\boldsymbol{\varepsilon}}^{\mathbf{p}}, \tag{5}$$

which includes the elastic part $\dot{\boldsymbol{\varepsilon}}^{\mathbf{e}} = \mathbf{M}:\dot{\boldsymbol{\sigma}}$ (M is the elastic compliance tensor) and the plastic part $\dot{\boldsymbol{\varepsilon}}^{\mathbf{p}}$. For the MG phase, the carriers of plastic deformation are shear transformation zones (Argon, 1979; Falk and Langer, 1998; Pan et al., 2008) or flow defects such as free volume (Spaepen, 1977, 2006). The plastic part of the strain rate is caused by viscous deformation. Therefore, Eq. (5) can be recast as:

$$\dot{\boldsymbol{\varepsilon}} = \dot{\boldsymbol{\varepsilon}}^{\mathbf{e}} + \dot{\boldsymbol{\varepsilon}}^{\mathbf{p}} = \mathbf{M} : \dot{\boldsymbol{\sigma}} + \boldsymbol{\sigma}'/\eta \,, \qquad (6)$$

where, η is the shear viscosity depending on, temperature T, equivalent stress $\sigma_e = \sqrt{3\sigma'_{ij}\sigma'_{ij}/2}$, and free volume concentration ξ (Steif,1983), given as,

$$\eta = \sigma_{\mathrm{e}} / f_0 \exp(-\frac{\Delta G^m}{k_B T}) \exp(-\frac{1}{\xi}) \sinh(\frac{\sigma_e \Omega}{2 k_B T}) \,, \qquad \mathbf{(7)}$$

where f_0 is the frequency of atomic vibration, ΔG^m the activation energy, k_B the Boltzmann's constant, and Ω the atomic volume. In metallic materials, free volume can be created by shear deformation when an atom is squeezed into a void smaller than its own volume. The free volume concentration can also be changed by other mechanisms such as the diffusion. Herein, the diffusion-production equation is employed as its evolution law of free volume concentration, expressed as (Huang et al., 2002; Jiang et al., 2009):

$$\dot{\xi} = D \cdot \nabla^2 \xi + \frac{1}{\alpha} f_0 \exp(-\frac{\Delta G^m}{k_B T}) \exp(-\frac{1}{\xi}) \{ \frac{2 k_B T}{\xi v^* S} [\cosh(\frac{\sigma_e \Omega}{2 k_B T}) - 1] - \frac{1}{n_D} \} \,, \qquad (8)$$

where α is a geometrical factor of order unity, v^* a critical volume, S the Eshelby modulus given by $S = 2(1+v)\mu / 3(1-v)$, and n_D is the number of atomic jumps needed to annihilate a free volume equal to v^*. The first term on the right-hand side of the equation represents the diffusion of free volume, and the second one is related to the annihilation and generation of free volume which is a thermally activated process. The temperature T in Eqs. (7) and (8) is determined from the heat conduction equation, given by (Yang et al., 2006):

$$\dot{T} = \lambda \nabla^2 T + \frac{\beta_{TQ}}{\rho C_V} \sigma'_e \dot{\varepsilon}_e^p \,, \qquad (9)$$

where λ is thermal conductivity, β_{TQ} the Taylor-Quinney coefficient, ρ the density, and C_V the heat capacity. Because the MG phase surrounds nanograins in NDPGC alloys with the thickness in the order of several nanometers, it is safe to ignore the diffusion of free volume.

For the crystalline phase, plastic strain rate is proportional to the deviatoric stress $\boldsymbol{\sigma}'$ based on the conventional J2-flow theory of plasticity, given by

$$\dot{\boldsymbol{\varepsilon}}^{\mathrm{p}} = \frac{3\dot{\varepsilon}^{\mathrm{p}}}{2\sigma_{\mathrm{e}}}\boldsymbol{\sigma}', \tag{10}$$

where $\dot{\varepsilon}^{\mathrm{p}}$ is the equivalent plastic strain rate, expressed as

$$\dot{\varepsilon}^{\mathrm{p}} = \dot{\varepsilon}\left[\frac{\sigma_{\mathrm{e}}}{\sigma_{flow}}\right]^{\mathrm{m}_0}, \tag{11}$$

where $\dot{\varepsilon} = \sqrt{2\dot{\varepsilon}'_{ij}\dot{\varepsilon}'_{ij}/3}$ is the equivalent strain rate with $\dot{\varepsilon}'_{ij} = \dot{\varepsilon}_{ij} - \dot{\varepsilon}_{kk}\delta_{ij}/3$, m_0 the rate-sensitivity exponent, and σ_{flow} is a reference flow stress. For nanograins with the size of a few nanometers, the strength could be close to the ideal strength because the activity of lattice dislocations is blocked by inner boundaries. In order to account for the effect of inner boundaries, we assumed a dislocation pile-up zone adjacent to each of the boundaries, leading to the additional dislocation-density term in the Taylor-type law of flow stress, expressed as,

$$\sigma_{flow} = M\alpha\mu b\sqrt{\rho_{IC} + \rho_{IB}}, \tag{12}$$

where α, μ, b and M are the empirical constant, shear modulus, Burger constant and Taylor factor, respectively, ρ_{IB} and ρ_{IC} are the dislocation densities in the dislocation pileup zones adjacent to inner boundaries and inside the grains, respectively. ρ_{IB} can be expressed given by $\rho_{IB} = k^{IB}\eta^{IB}/b$, where $k^{IB} = 6d_{IBZ}/\phi^{IB}d_G$, d_{IBZ} is the thickness of dislocation pile-up zones, d_G is the grain size, η^{IB} is the strain gradient in dislocation pile-up zones (Zhu et al., 2011, 2019). ρ_{IC} can be derived from Kocks and Mecking's model (Kocks and Mecking, 2003). Based on the Taylor model of flow stress, the other deformation mechanisms can also be involved in the crystalline phase when there exit the nanoscale twins or nanolamellaes in grains (Zhu et al, 2011; Cao et al., 2018).

3.3 Criterion for generating shear bands in NDPGC pillars

During the deformation of a NDPGC alloy, multiple shear bands can be formed before fracture, as shown in Fig. 1 and in the references (Wu et al., 2017; Sun et al., 2020). The energy dissipation rate in shear bands determines the intrinsic resistance to the shear band propagation. When the deformation energy increases more swiftly than dissipation through shear banding, additional shear bands may be generated. Therefore, a criterion based on energy competition is proposed for shear band multiplication in NDPGC alloys. Following Grady (1992), the critical energy dissipation per unit area within shear band of crystalline phase, considering thermal and momentum dissipations, can be expressed as

$$\Pi_{\mathrm{C}} = \frac{\rho c}{S_T}\left(\frac{9\rho^3 c^2 D_T^3}{S_T^2 \dot{\gamma} \sigma_y^3}\right)^{1/4}, \tag{13}$$

in which ρ is the density of the material, S_T is the thermal softening coefficient, c bulk specific heat, D_T the thermal diffusivity coefficient, $\dot{\gamma}$ shear strain rate, and σ_y the yield strength. Note that σ_y is grain size-dependent (the Hall-Petch relation) but independent of sample size as the latter is caused by the effect of free surface, which becomes prominent only when the sample size is in the ten-nanometer scale (Zhang et al., 2010; Zhu et al., 2014).

For the MG phase, the critical energy dissipation per unit area within shear band can be given by (Jiang et al., 2011)

$$\Pi_{\mathrm{B}} = \frac{\sigma_e}{S_v R}\left(\frac{9\rho D_f{}^3}{S_v^2 R^2 \dot{\gamma}\sigma_e}\right)^{1/4}, \tag{14}$$

in which S_v is free volume softening coefficient, R the local dilatation ability, D_f the diffusion coefficient. Note that the deformation mechanism in MG is sample-size-dependent (Greer et al., 2013). For a purely MG pillar, if the diameter is smaller than 100 nm, the shear band-dominant deformation (which is brittle) transforms to a homogeneous flow behavior (which is ductile) during compression. However, in the NDPGC pillars, this brittle-to-ductile transition (BDT) occurs in the much larger diameter, as shown in Fig. 1, which must be ascribed to the nanograins. Therefore, we assume herein that the critical dissipation energy within a MG shear band is also independent of sample size.

The critical dissipation energy within shear bands of NDPGC alloys can be expressed based on the simple rule of mixture:

$$\Pi_{\mathrm{NGL}} = f_C \Pi_{\mathrm{C}} + f_B \Pi_{\mathrm{B}}. \tag{15}$$

Here, f_C and f_B are the volume fractions of crystalline and MG phases, respectively. During the compression of a NDPGC micropillar, the deformation energy per unit area within the cross-section of the specimen can be expressed as:

$$\Pi_{\mathrm{Def}} = \sigma_1 \varepsilon_1 \mathrm{L}/2. \tag{16}$$

Here, σ_1 and ε_1 are the compressive stress and strain in the loading direction, respectively, L the length of the sample. Thus, the criterion for generating one more shear band is:

$$\Pi_{\text{Def}} \geq N \cdot \Pi_{\text{NGL}}, \tag{17}$$

where N is the number of global shear bands in NDPGC alloy. Denoted by α_r the aspect ratio of a pillar, i.e., $\text{L}=\alpha_r D$, the criterion for generating multiple shear bands (Eq. (17)) is recast as

$$D \geq \frac{2N \cdot \Pi_{\text{NGL}}}{\alpha_r \sigma_1 \varepsilon_1}. \tag{18}$$

With Eq. (18) the critical sample size can be determined, at which the deformation mechanism transits from shear banding to the homogeneous plastic flow given that shear band has a finite thickness that determines maximum N in a nanopillar.

4. Hierarchical micromechanical model for smaller micropillars of NDPGC alloy

4.1 First type of hierarchical composite during activating MG flow behavior

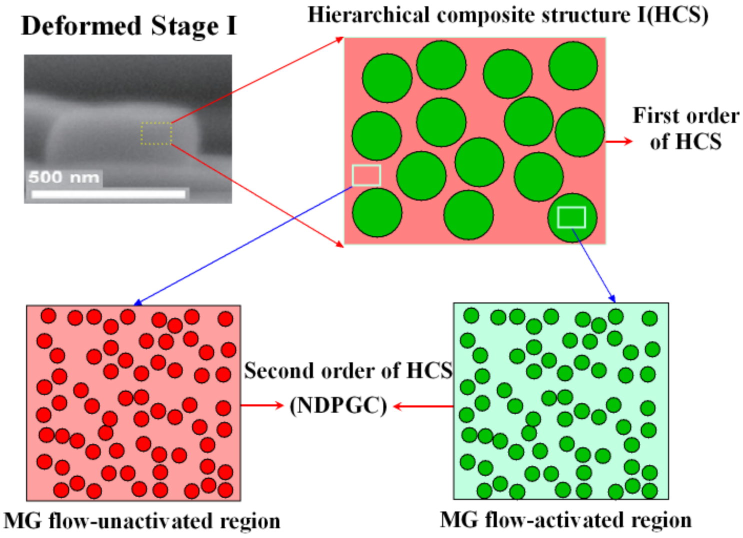
Deformed Stage I
Hierarchical composite structure I(HCS)
500 nm
First order of HCS
Second order of HCS (NDPGC)
MG flow-unactivated region
MG flow-activated region

Figure 3. The schematic drawings of the first type of hierarchical structure in NDPGC alloys, in which the material is separated into two regions in micrometer scale. They are named MG flow-activated and MG flow unactivated regions, which possess both MG and crystalline phases.

Because the atomic composition in a NDPGC alloy varies continuously from the MG phase to crystal phase (Wu et al., 2017; Sun et al., 2020), we expect strong interactions between the atoms in both side of the MG-crystalline interface. Because of the constraint of atoms in the crystalline phase, the MG phase is more prone to homogenous plastic flow than pure MG, which leads to the BDT size larger than that of pure MG. However, the occurrence of homogenous flow also depends on the exact distribution of nanograins in a MG matrix; therefore, it is proposed that the NDPGC materials can be divided into the MG-flow activated (MG-FA) and the MG-flow unactivated (MG-FUA) regions, which are both MG–crystalline composites, as illustrated schematically in Fig. 2. It is anticipated that small NDPGC pillars mainly consist of MG-FA regions as suggested by the experimental results. We shall further clarify this point in the following text. It should be emphasized that the MG-FA region appears to be soft owing to the activated flow. In contrast, the MG-FUA region appears harder. Therefore, the total stress and strain of NDPGC micropillars, consisting of the soft and hard regions, can be obtained based on the modified Mori-Tanaka model (Zhu and Lu, 2012). The relations between the hydrostatic/deviatoric stresses $(\overline{\sigma}_{kk}\ or\ \overline{\sigma}'_{ij})$ and strains $(\overline{\varepsilon}_{kk}\ or\ \overline{\varepsilon}'_{ij})$ are given by

$$\overline{\sigma}_{kk} = 3k_{UA}\left[1 + \frac{c_A(k_A - k_{UA})}{c_A\alpha_A^s(k_{UA} - k_{UA}) + k_{UA}}\right]\overline{\varepsilon}_{kk}$$

$$\overline{\sigma}'_{ij} = 2\mu_{UA}^s\left\{\left[1 + \frac{c_A(\mu_A - \mu_{UA}^s)}{c_{UA}\beta_{UA}^s(\mu_A - \mu_{UA}^s) + \mu_{UA}^s}\right]\overline{\varepsilon}'_{ij} - \frac{c_A(\mu_A - \mu_{UA}^s)}{c_{UA}\beta_{UA}^s(\mu_A - \mu_{UA}^s) + \mu_{UA}^s}\varepsilon_{ij}^{p(A)}\right\}. \quad (19)$$

Here, A refers to the MG-FA region, and UA represents the MG-FUA region. k_A and μ_A^s are the bulk and shear moduli of MG-FA region, respectively. k_{UA} and μ_{UA}^s are the bulk and shear moduli of MG-FUA region, respectively. $\varepsilon_{ij}^{p(A)}$ is the plastic strain of MG-FA region. α_A^s and β_{UA}^s are the components of Eshelby's tensor. c_A and c_{UA} represent the volume fraction of the MG-FA region and MG-FUA region which may vary with plastic strain. The relations between the hydrostatic and deviatoric strains of the constituent phases (the MG-FA region and MG-FUA region) and the averaged ones of a pillar are:

$$\varepsilon_{kk}^{(UA)} = \frac{\alpha_{UA}^s(k_A - k_{UA}) + k_{UA}}{c_{UA}\alpha_{UA}^s(k_A - k_{UA}) + k_{UA}}\bar{\varepsilon}_{kk}, \varepsilon_{kk}^{(A)} = \frac{k_{UA}}{c_{UA}\alpha_{UA}^s(k_A - k_{UA}) + k_{UA}}\bar{\varepsilon}_{kk}$$

$$\varepsilon_{ij}^{(UA)\prime} = \frac{\beta_{UA}^s(\mu_A - \mu_{UA}^s)}{c_{UA}\beta_{UA}^s(\mu_A - \mu_{UA}^s) + \mu_{UA}^s}\bar{\varepsilon}_{ij}' - \frac{c_{UA}\beta_{UA}^s\mu_A}{c_{UA}\beta_{UA}^s(\mu_A - \mu_{UA}^s) + \mu_{UA}^s}\varepsilon_{ij}^{p(A)}$$

$$\varepsilon_{ij}^{(A)\prime} = \frac{\mu_{UA}^s}{c_{UA}\beta_{UA}^s(\mu_A - \mu_{UA}^s) + \mu_{UA}^s}\bar{\varepsilon}_{ij}' + \frac{c_{UA}\beta_{UA}^s\mu_A}{c_{UA}\beta_{UA}^s(\mu_A - \mu_{UA}^s) + \mu_{UA}^s}\varepsilon_{ij}^{p(A)}, \qquad (20)$$

where $\varepsilon_{kk}^{(UA)}$ and $\varepsilon_{kk}^{(A)}$ are the hydrostatic strains of MG-FUA region and MG-FA region, respectively. $\varepsilon_{ij}^{(UA)\prime}$ and $\varepsilon_{ij}^{(A)\prime}$ are the deviatoric strains of MG-FUA region and MG-FA region, respectively. $k_i = E_i/3(1 - 2v_i^s), \mu_i = E_i/2(1 + v_i^s)$, in which $E_i(i = A, UA)$ and $v_i(i = A, UA)$ are the elastic modulus and Poison's ratio. In the proposed model, the interfaces between MG and crystalline phases are assumed to be cohesive. This is also the case for the interfaces between MG-FA and MG-FUA regions.

For the part of MG phase exhibiting activated flow (or a homogenous plastic deformation), the free volume concentration must be in a steady state. Therefore, the annihilation of free volume induced by structural relaxation is taken into account, i.e., (Thamburaja and Ekambaram, 2007; Cheng and Ghosh, 2013; Dutta et al., 2018),

$$\dot{\xi} = D \cdot \nabla^2 \xi + \frac{f_0}{\alpha}\exp(-\frac{\Delta G^m}{k_B T})\exp(-\frac{1}{\xi})\{\frac{2k_B T}{\xi v^* S}[\cosh(\frac{\sigma_e \Omega}{2k_B T}) - 1] - \frac{1}{n_D}\} - \frac{\xi - \xi_T}{\sigma_e / (\mu \dot{\varepsilon}^p)}. \quad (21)$$

Here, ξ_T is the a stress-free and temperature dependent equilibrium free volume concentration, which can be described by the Cohen-Grest model (Grest and Cohen, 1981), given as

$$\xi_T = \left(\hat{T} + \sqrt{\hat{T}^2 - d_2 T}\right) / 2d_1 \quad , \tag{22}$$

where $\hat{T} = T - T_{ref}$. T_{ref} is the reference temperature, d_1 and d_2 are constants.

4.2 Second type of hierarchical composite during constituent re-organization

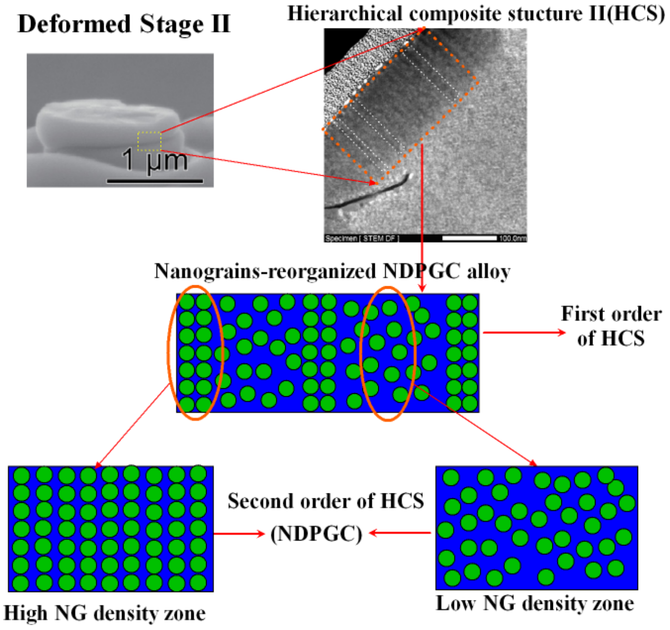
Deformed Stage II
Hierarchical composite stucture II(HCS)
1 μm
Specimen | STEM DF |
100.0nm
Nanograins-reorganized NDPGC alloy
First order of HCS
Second order of HCS
(NDPGC)
High NG density zone
Low NG density zone

and

Figure 4. The schematic drawings for the second type of hierarchical structure in a NDPGC alloy in which the reorganization of nanograins occurs, forming the high NG and low NG density zones.

In small micropillars, all MG regions may be activated to deform homogenously. Because the flow of MG can bring about the sliding and rotation of nanograins, the re-organization of nanograins occurs in a severely deformed micropillar. Such a re-organization causes some nanograins to become closer and aligned and other nanograins more separate. As a result, the high-density nanograin zone (HDGZ) and low-density nanograin zone (LDGZ) are formed during plastic deformation, as shown in Fig. 1(c) and Fig. 4. These HDGZ and LDGZ gradually arrange layer by layer along the loading direction. The micropillar then can be regarded as a composite laminate consisting of the HDGZ and LDGZ. It is reasonable to assume that the strain in the cross-section pedicular to the loading direction distributes uniformly and that the strains in the HDGZ and LDGZ are the same. The averaged stress-strain relation can be expressed as:

$$\begin{aligned} &\bar{\sigma}_{\mathrm{zz}} = f_H(\varepsilon_0)\sigma_{\mathrm{zz}}^{(H)}(\varepsilon_0, \mathrm{d_G}) + f_L(\varepsilon_0)\sigma_{\mathrm{zz}}^{(L)}(\varepsilon_0, \mathrm{d_G}) \\ &\varepsilon_{\mathrm{zz}}^{(H)} = \varepsilon_{\mathrm{zz}}^{(L)} = \varepsilon_0 \quad . \end{aligned} \tag{23}$$

Here, $f_i(i = H, L)$ is the volume fraction of the *i*th phase which is the function of the strain ε_0 with the subscripts H and L pertaining to the HDGZ and LDGZ, respectively. $\sigma_{\mathrm{zz}}^{(i)}(\varepsilon_0, \mathrm{d_G})$ is the normal stress of the *i*th phase along the loading direction Z, which is the function of the grain size $\mathrm{d_G}$ and strain ε_0. Although both of HDGZ and LDGZ consist of the crystalline and MG phases, the volume fractions of them are no longer constant but varied with the plastic strain. Suppose the volume fraction of MG phase in HDGZ to be f_H^{MG} as a constant, the volume fraction of MG phase in LDGZ can be given as

$$f_L^{MG} = c_G - f_H f_H^{MG}. \tag{24}$$

Then, the volume fraction of crystalline phase in LDGZ is

$$f_L^C = c_C - f_L(1 - f_H^{MG}). \tag{25}$$

Because the volume fractions of HDGZ and LDGZ changes during deformation, f_L^{MG} and f_L^C are both the functions of the strain. On the other hand, since the nanograins could touch each other during further compression and the crystalline grains may also be refined upon further loading, the average grain size also varies with plastic strain.

5. Results and discussion

In this section, we apply the constitutive model presented in Sections 3 and 4 to describe the size-dependent mechanical properties of Mg-based NDPGC alloys. The objective is to explore the effects of sample size and grain size. Table 1 lists the value of parameters in the proposed model for simulations, which were extracted from the literature (Huang et al., 2002; Gao, 2006; Jiang et al., 2009, 2011) or by fitting the experimental data (Wu et al., 2017, 2020a; Sun et al., 2020).

5.1 Comparisons between simulations and experiments

5.1.1 Constitutive behavior and multiple shear band generation in large micropillars

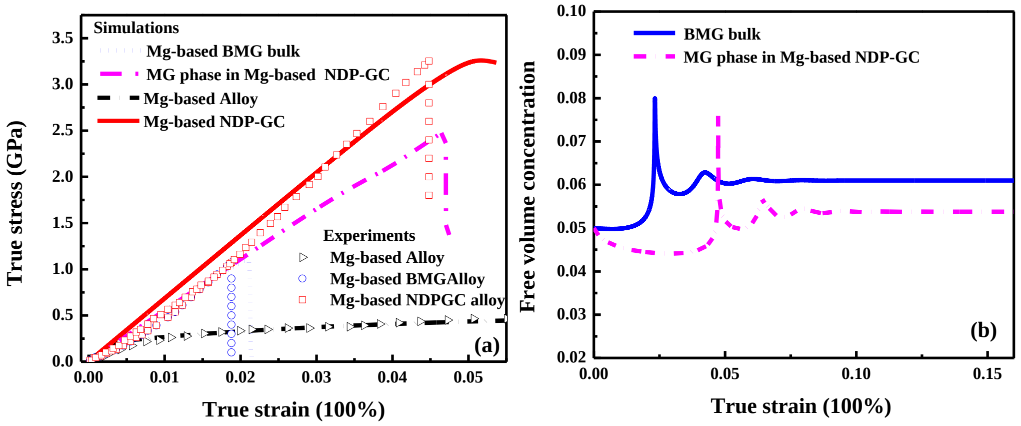

Figure 5. (a) The comparison of the simulation and experimental results in terms of stress-strain curves and (b) the variations of free volume concentration with strain in a bulk metallic glass (BMG) and in the MG phase of a Mg-based NDPGC alloy.

The stress-strain curves calculated by the proposed model for the large pillar of Mg-based NDPGC alloy, coarse-grained $MgCu_2$, Mg-based bulk metallic glass (BMG) and the metallic glass phase in Mg-based NDPGC alloy are presented in Fig. 5(a), accompanied by the experimental measurements. It is noted that the simulation results agrees well with experimental results as shown in Fig. 5(a) and that the simulated ultimate strength of the Mg-based NDPGC alloy is around 3.26 GPa close to the experimental one of 3.3 GP for large pillars. Such an ultrahigh strength arises from the strengthening effect of dislocation-free-nanosized $MgCu_2$ and the delayed generation of global shear band in metallic glass phase. The comparison of the stress-strain curves of the Mg-based BMG and the MG phase in the NDPGC alloy, as shown in Fig. 5 (a), indicates that the shear-band-induced crack appears at the strain of around 2% for the BMG and around 5% for the MG phase in Mg-based NDPGC alloy. The delay of shear-band-induced cracking is originated from the difference in the evolution of free-volume concentration in MG phase and in a BMG, as shown in Fig. 5(b). The maximum free volume concentration in the MG phase of the NDPGC alloy occurs at the larger strain.

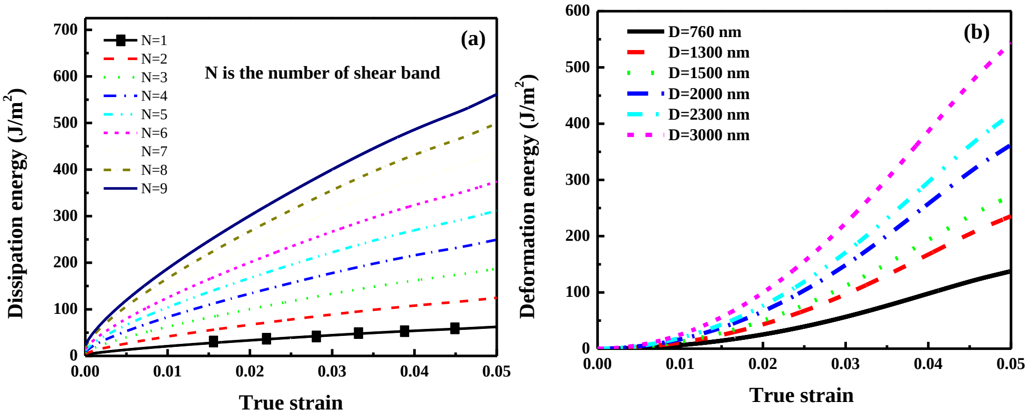

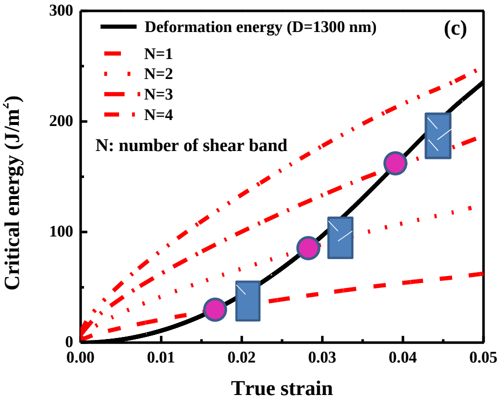

Figure 6. Energy criterion for shear band multiplication: (a) energy dissipation for generating multiple shear bands, (b) deformation energy as functions of strain in a Mg-based NDPGC alloy, and (c) the number of shear band determined by the intersections of dissipation energy and deformation energy curves for the micropillar with the diameter of 1300 nm.

Experiments have demonstrated pop-in behaviors in compressing large pillars (Wu et al., 2017), as shown in Fig. 1(d). Each pop-in is associated with the generation of a new shear band. For large pillars, the number of pop-ins increases with pillar diameter. This can be well explained using the energetic criterion for shear-band multiplication (see Section 3.4). Figs. 6(a) and 6(b) illustrate the energy dissipated within shear bands and the deformation energy in pillars, which are both functions of the applied strain. It is apparent that the increase of the number of shear band leads to the larger critical energy for generating an additional shear band (Fig. 6(a)) and that increasing the diameter of pillars leads to more deformation energy (Fig. 6(b)). When the curve of deformation energy intersects the curves of energy dissipation one more shear band must be formed. Give the diameter of 1300 nm as exemplified in Fig. 6(c), the three

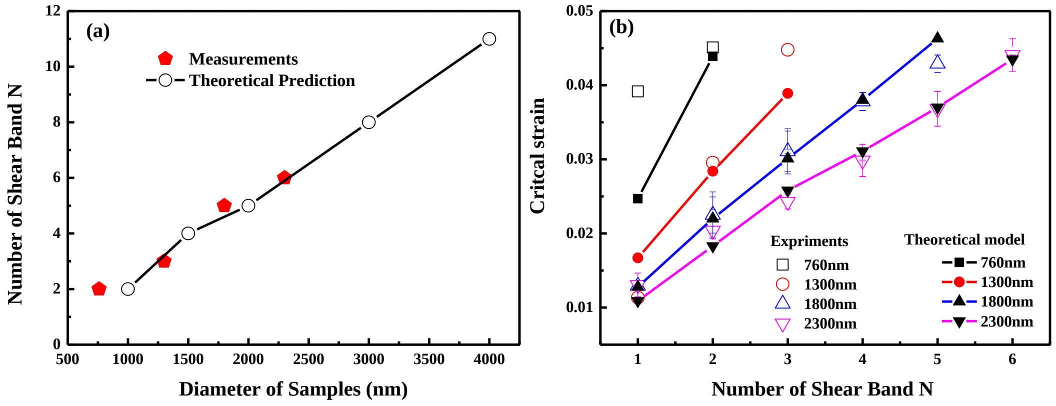

Figure 7. The comparisons between the simulations and experimental measurements for the number of shear band varied with the diameter of micropillars (a), and for the critical strain at which the corresponding shear band generated (b).

intersections before the fracture strain of 0.5% indicate that three shear bands formed in the 1300 nm pillar.

With the energy criterion, the maximum number of shear band varied with the dimeter of pillars can be determined and the comparison with experimental results (by counting the number of pop-ins) is shown in Fig. 7(a). It is clear that the number of shear band increases with pillar diameter and that the theoretical results agree well with experimental ones. Fig. 7(b) shows the strain corresponds to each shear band formation with different pillar diameter. It is interesting to note is that the strain for the first shear band decreases with pillar diameter, but the strain for the final shear band is almost the same. Also, it is noted that the predictions based on the proposed criterion are in line with experimental results obtained when the pillar diameter is larger than 700 nm. There exits the difference between the simulation and experimental results. In particular, the discrepancy increases when the pillar diameter becomes smaller (but still larger than 700 nm). Such inconsistency could be attributed to two causes. First, the perfect cylindrical samples cannot be prepared through focused-ion-beam milling. The deviation from a cylindrical shape is more significant when pillar diameter becomes smaller. Second, the deformation mechanism in MG phase would change from shear banding or homogenous flow when pillar diameter decreases. This transition is not abrupt, namely that the two deformation mechanisms could both operate when pillar diameter is in the submicron regime.

5.1.2 Constitutive behavior of small micropillars

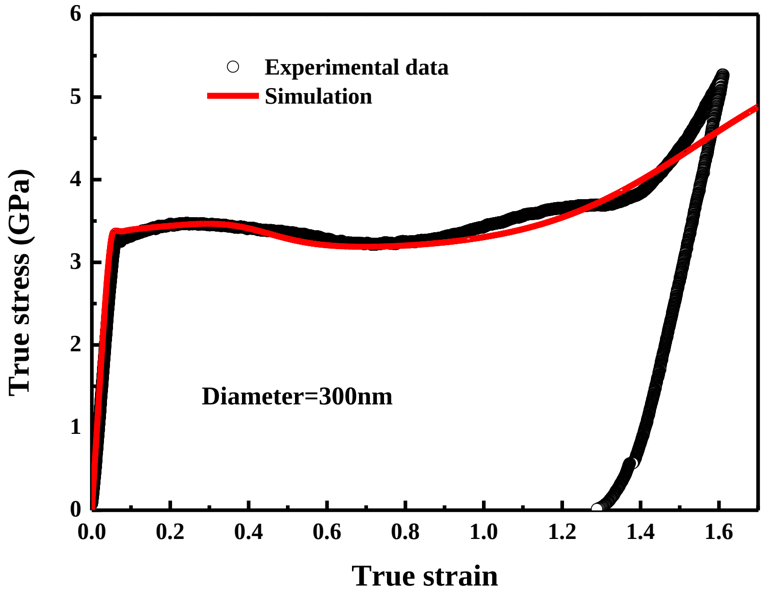

Figure 8. The comparisons between the simulation and experimental data for the constitutive behavior of smaller micropillars of Mg-based NDPGC alloy with the diameter of 300 nm.

In Fig. 7(b), it has been shown that the critical strain for generating the first shear band increases with the reduction in pillar diameter. In experiments, small Mg-based

NDPGC micropillars with diameters less than 500 nm are ductile under compression as shown in Fig. 1(e). Shear band does not form during deformation (Wu et al., 2020), and homogenous flow occurs in the MG phase associated with grain re-organization and grain refinement. With the proposed model, the calculated stress-strain curve is compared with the experimental results for a 300 nm pillar in Fig. 8, showing a very good agreement as the proposed model successfully captures the yielding, softening, and hardening behaviors.

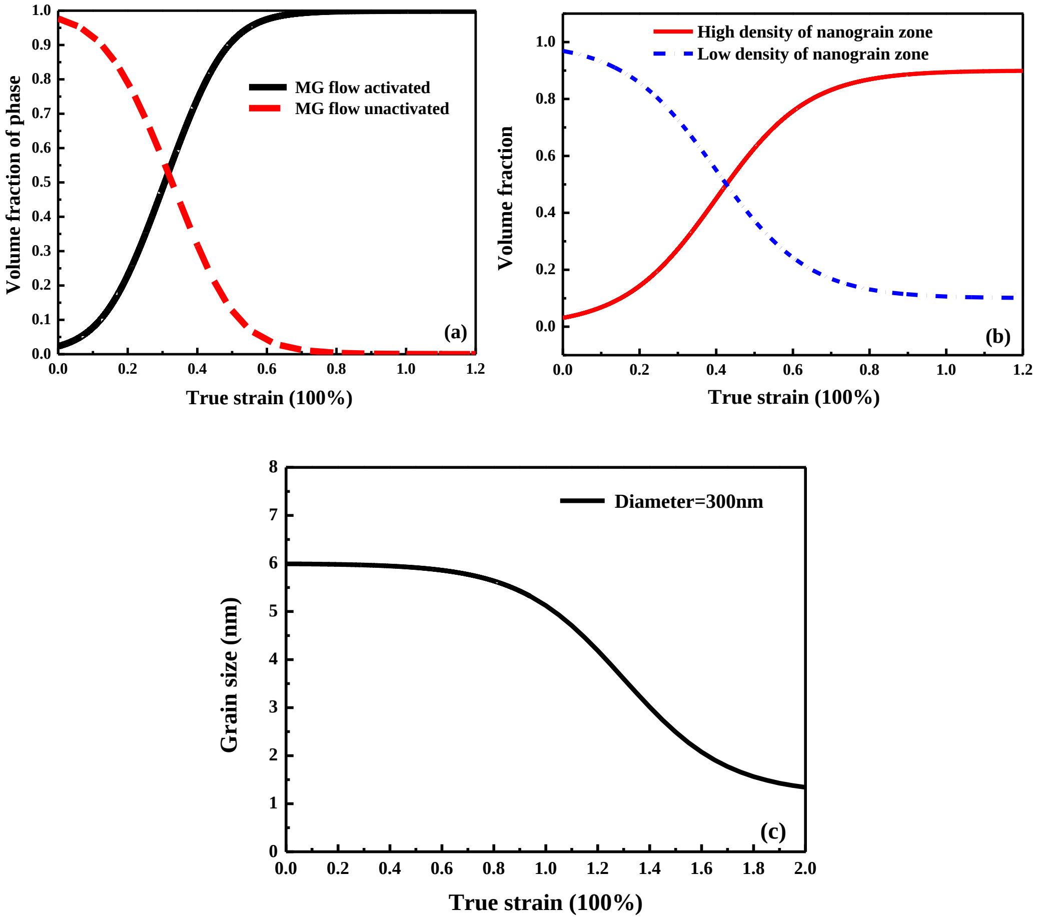

Figure 9. The volume fractions of MG-FA and MG-FUA regions (a), the ones of HDGZ and LDGZ (b), and the grain size (c) as the functions of strain in Mg-based NDPGC alloy.

The excellent agreement between the theoretical and experimental results for small pillars indicates that the presumed variations of the volume fractions of constituent regions or phases are necessary. In the early stage of plasticity, the harder MG-FUA regions are gradually active to become the softer MG-FA regions, resulting in the softening behavior. Afterward, the grain re-organization and refinement increase the HDGZ layers, resulting in hardening. In the proposed model, the volume fractions of MG-FA region and HDGZ as well as the grain size are assumed to be functions of the applied strain, expressed as:

$$c_A = 1 - \frac{1}{1+\exp\frac{(\varepsilon-a_1)}{a_2}}, \quad f_H = b_0 - \frac{b_0}{1+\exp\frac{(\varepsilon-b_1)}{b_2}}, \quad d_{\mathrm{G}} = \frac{c_0}{1+\exp\frac{(\varepsilon-c_1)}{c_2}} + c_3. \quad \text{(26a,b,c)}$$

Here, ε is the strain, $a_{\mathrm{i}}(i = 1,2)$, $b_{\mathrm{i}}(i = 0,1,2)$, $c_{\mathrm{i}}(i = 0,1,2,3)$ are the fitting parameters as shown in Table 1. Fig. 9(a) shows the volume-fraction curves of MG-FA and MG-FUA regions against strain. Since the MG-FUA region is the harder phase, the strain hardening behavior occurs when the volume fraction of MG-FUA region dominates (>50 %). With further deformation, MG-FA regions gradually overwhelm (>50% when ε > 0.3), as shown in Fig. 9(a), leading to the softening behavior (see Fig. 8). One can find from Fig. 9(a) that MG-FUA region almost vanishes at the strain around 0.7; consequently, the softening behavior ceases at this strain, as shown in Fig. 8. When flow activation process ceases, the formation of HDGZ takes place causing further hardening. Figs. 9(b) and 9(c) show the volume fractions of HDGZ/LDGZ and grain size with strain, respectively. It is noted that grain-reorganization causes an increase in HDGZ, which ceases at ε ≈ 0.9. The subsequent sharp hardening as shown in Fig. 8 is caused by grain refinement as shown in Fig. 9(c).

5.2 Predictions of constitutive behaviors of NDPGC pillars

5.2.1 Grain size-dependent constitutive behavior and shear band generation in large NDPGC pillars

Since the NDPGC alloy consists of crystalline and MG phases, the mechanical properties of such a composite material are functions of the properties of these constituents. While there are limitations in experiments to freely adjust the properties of constituent phases, we may employ our model to make some predictions. For large NDPGC pillars exhibiting brittle behavior, the effect of grain size (d_G) is on stress-strain relation is shown Fig. 10. Decreasing the grain size from 50 nm to 10 nm, the yield strength increases because the softening mechanisms in nanocrystalline materials, such as the grain boundaries activities (grain boundary migration, diffusion, and grain rotation), no longer operate.

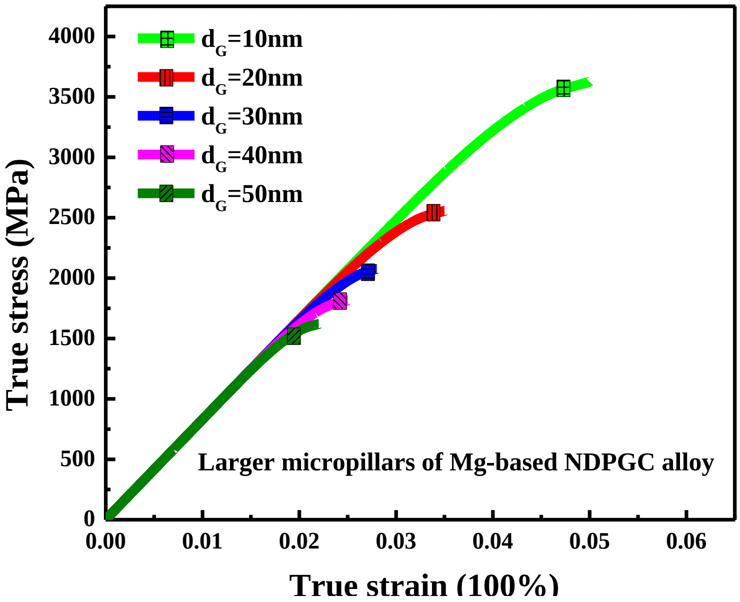

Figure 10. The predicted stress-strain relations of larger micropillars of Mg-based NDPGC alloy with different grain size.

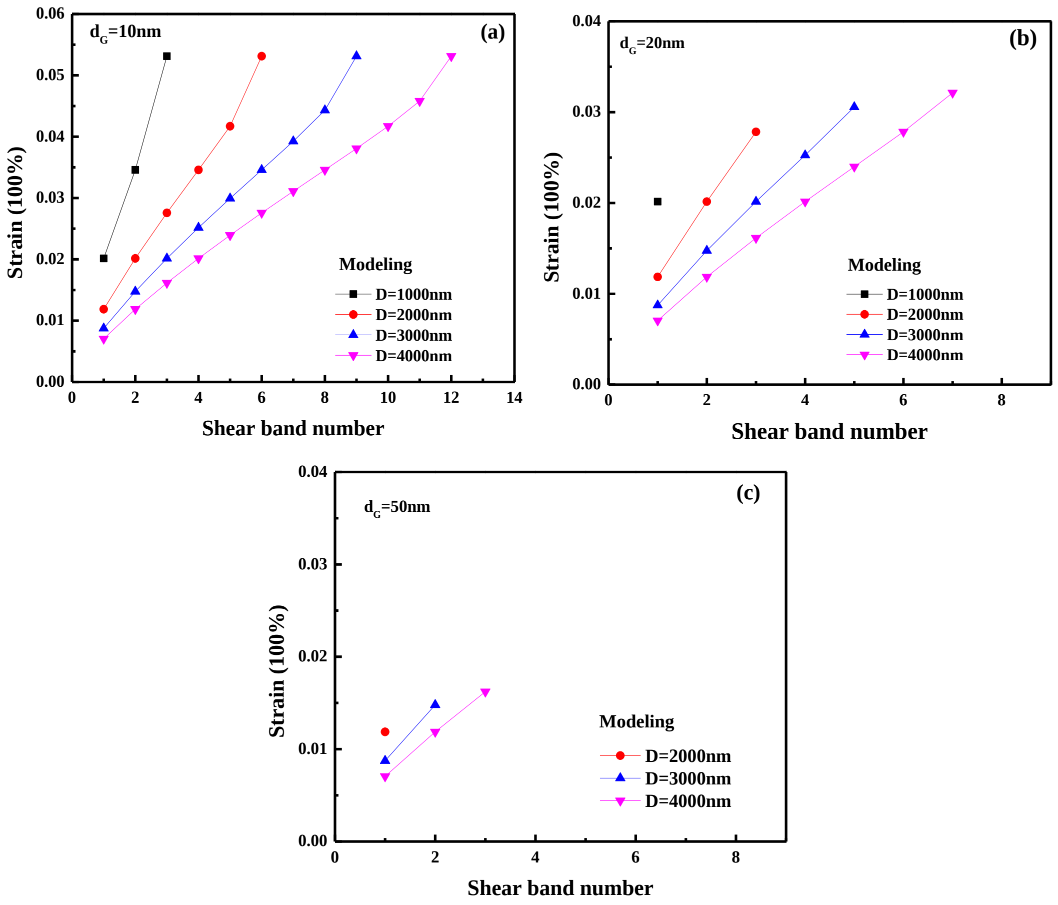

Figure 11. The predictions based on the proposed criterion for the critical strain vs the shear band number for different diameters of pillars with the grain size of (a) 10 nm, (b) 20 nm and (c) 50 nm.

Changing grain size leads to the change of deformation energy and the shear banding behavior. The number of shear band in large NDPGC pillars is therefore also grain-size-dependent. Figs. 11(a-c) demonstrate that the strains for generating different number of shear bands vary with grain size. The number of shear bands decreases when the grain size increases from 10 to 50 nm, because the deformation energy reduces with larger grain size. We further investigated the effect of pillar diameter on pop-in strains and shear band numbers, as shown in Figs. 12(a) and 12(b), respectively. It is shown that increasing the pillar diameter (for large pillars) results in smaller pop-in strains and more shear band number. As the maximum number of shear bands is also grain-size-dependent, we show the combined effect of d_G and pillar diameter in Fig. 12(b) and (c). These figures demonstrate that smaller grain size and pillar diameter both lead to more shear bands.

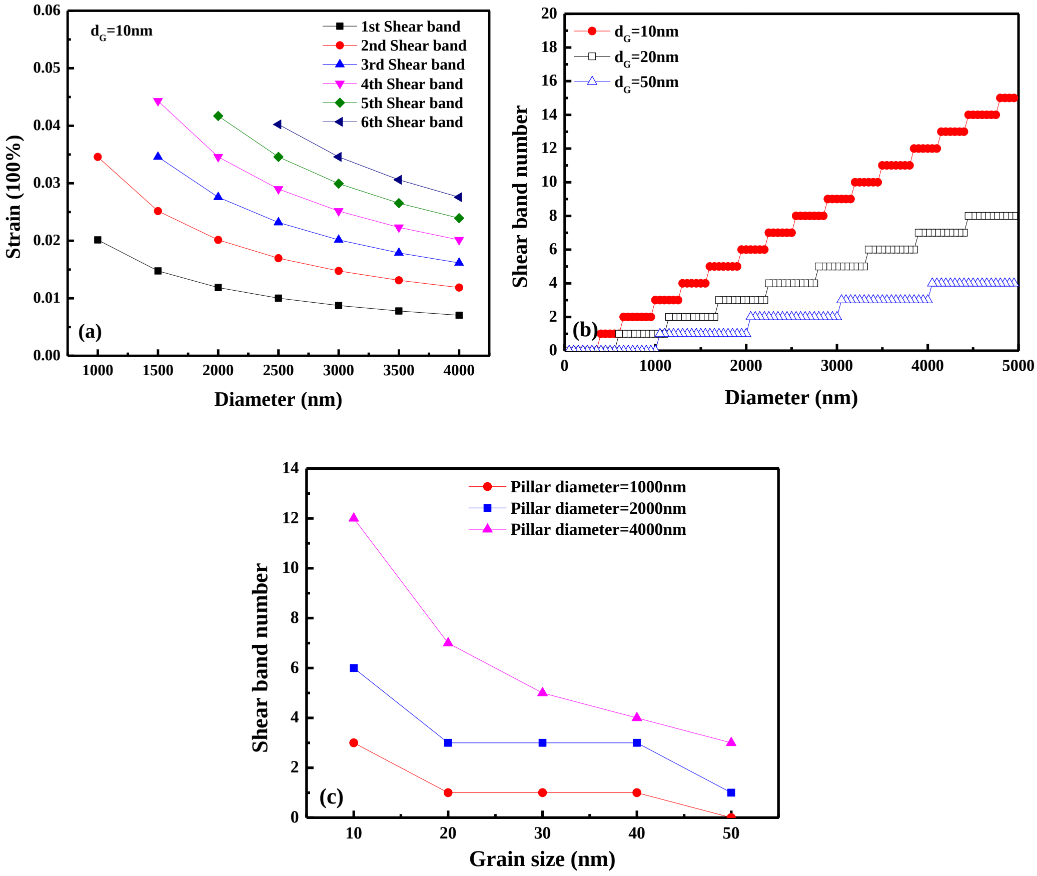

Figure 12. The predictions based on the proposed criterion for the critical strain vs the diameter with different shear band number (a), the shear band number vs the diameter with different grain size (b), and the shear band number vs grain size with different dimeter (c).

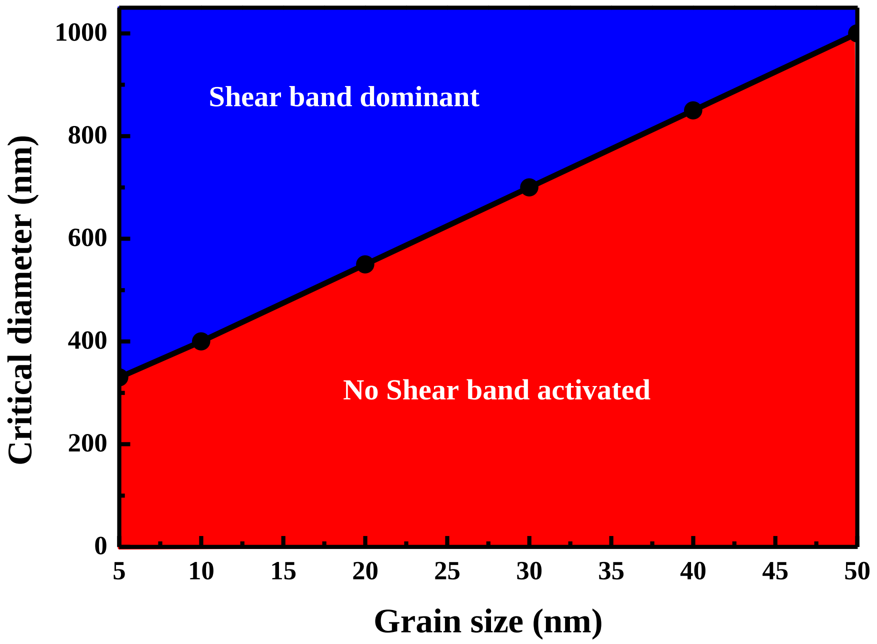

Figure 13. The critical diameter of micropillars for generating the shear band as the function of the grain size. The blue region is for enabling to generate the shear band, and the red region is for no shear band generation.

Additionally, one can also conclude from figures 11 and 12 that with further decreasing the pillar diameter of NDPGC alloy, there will be no shear band during deformation, as observed in the experiments. Therefore, there exists the critical pillar diameter for generating shear band which depends on grain size. Figure 13 shows the map of deformation mechanism which is governed by pillar diameter and grain size. It is noted that the critical pillar diameter for generating shear band increases with grain size. In Fig. 13, the blue region indicates shear-band dominant deformation mode, and the red region is for homogenous flow in the MG phase.

5.2.2 Plastic deformation in small pillars of Mg-based NDPGC alloy

For small pillars, the effect of grain sizes is shown in Fig. 14(a) and 14(b), which are stress-stain curves and grain size variations respectively. It is assumed that the volume fractions of MG-FA region and HDGZ change according to those shown in Figs. 9 (a) and 9 (b), respectively. Fig. 14 demonstrates that the yield strength increase with decreasing grain size and the plastic behaviors are almost identical. It means that for the micropillars with diameters less than the critical size for generating the shear band, excellent plasticity can be achieved under compression. A better combination of strength and ductility can be expected in NDPGC pillars with smaller grain size and diameter.

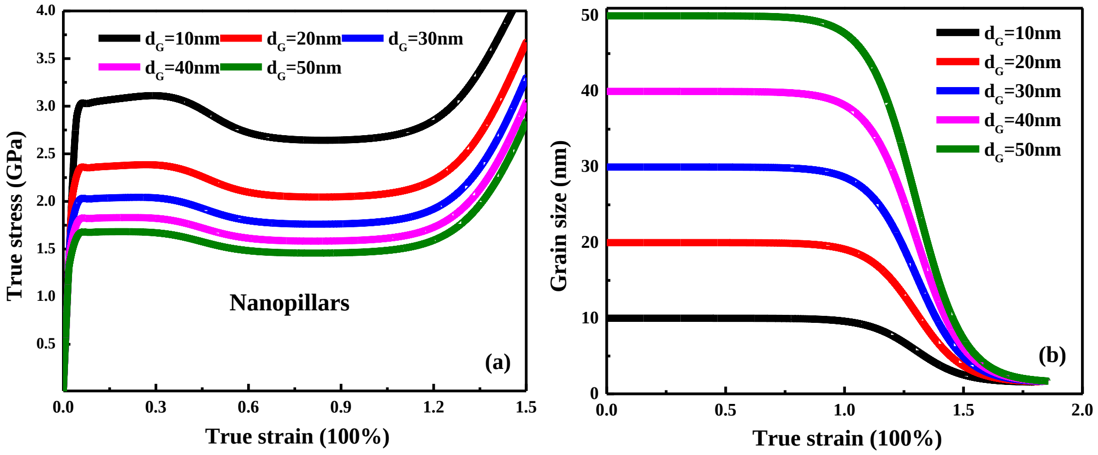

Figure 14. The predictions based on the proposed model for the constitutive behavior (a), and the grain size varied with strain during deformation for the smaller pillars of Mg-based NDPGC alloys with different grain size.

We further explore the influence of various parameters in the equations governing the evolution of volume fraction and grain size. Figure 15(a) and (b) demonstrate the effect of a_2 (Eq. (26a)) on stress-strain relations of small NDPGC pillars and the volume fraction of MG-FA region, respectively. It is shown that the increase in a_2 makes the hardening and softening behaviors less prominent and slightly reduces the yield strength because the volume faction of MG-FA region is changed more gently with larger a_2. The reduced yield strength with larger a_2 is owing to the increment of MG-FA regions before the apparent yielding. Figure 16(a) shows the effect of c_2 (Eq. (26c)) on stress-strain relations of small NDPGC pillars. It is clear that increasing c_2 leads to stronger hardening when MG-FA region dominates because grain refinement becomes easier, as shown in Fig. 16(b). One may also notice that the change of grain refinement behavior does not influence the yield strength and early stage of plastic deformation as grain refinement occurs in the late stage of plastic deformation.

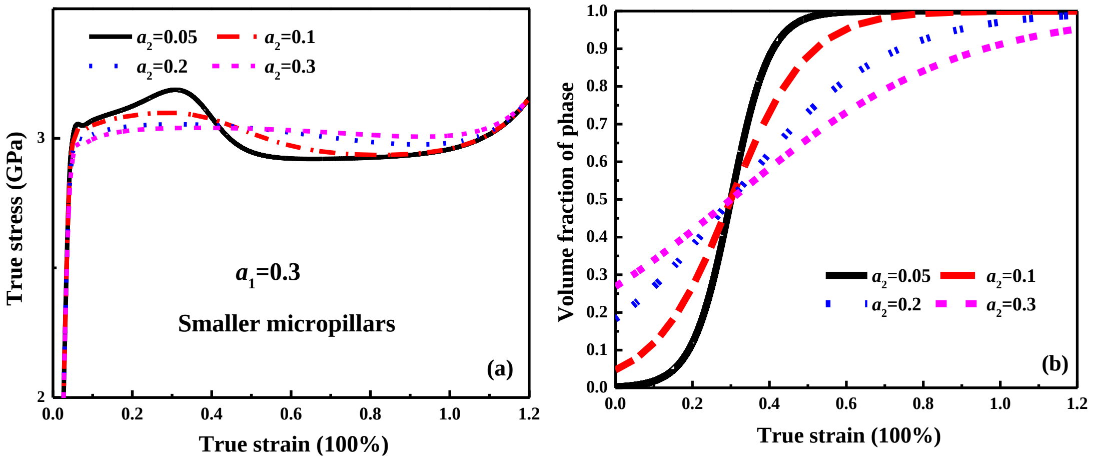

Figure 15. The effect of a_2 on (a) the stress-strain relations of small micropillars and (b) the volume fraction of MG-FA region.

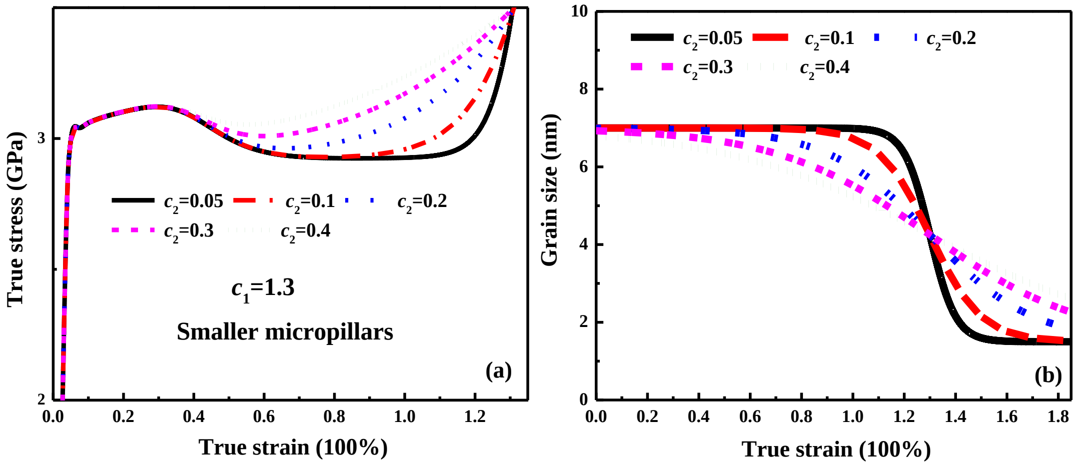

Figure 16. The predictions for the stress-strain relations of smaller micropillars with different parameter c_2 (a), the grain size as the function of strain with different c_2 (b)

6. Conclusions

In summary, the present work developed the constitutive model to describe the deformation behaviors of NDPGC micropillars. The constitutive relations of polycrystalline phase and metallic glass (MG) phase are presented for determining the stress-strain relations based on the micromechanics approach. The energy criterion for shear-band multiplication was also proposed to describe the pop-in behaviors in large pillars that possess the nearly ideal strength but no plasticity. For small pillars, the activation of MG flow, grain-reorganization and grain refinement are involved to capture the complicated plastic behavior, as featured by the hardening-softening-hardening process. The proposed model can describe the deformation behaviors of NGPGC micropillars, such as the ultrahigh strength, the multiple shear bands in larger pillars, and the excellent plasticity in smaller pillars. With the good agreements between the theoretical and experimental results, the proposed constitutive model and the energetic criterion are further employed to predict the effects of grain size and pillar diameter as well as the brittle-to-ductile transition. For small pillars, the model can capture the strain hardening and softening behaviors successfully. The constitutive behaviors of NDPGC alloys with different grains size are also investigated based on the proposed model, suggesting that the nearly ideal strength and excellent ductility can both be achieved in these small NDPGC pillars, overcoming the strength-ductility trade-off. In this sense, the model reported in this work could be an efficient tool to guide the alloy design based on the

NDPGC paradigm to achieve extreme properties of metallic materials.

Finally, we must remark that the proposed model and the associated parameter findings are based on experimental results of Mg-based NDPGC micropillars. Since the deformation mechanisms for the tensile behaviors of NDPGC micropillar could be different from those of compression (Wu et al., 2020b), the proposed constitutive models may not be applicable in the cases of tension.

Acknowledgements

The authors gratefully acknowledge the support received from the National Natural Science Foundation of China (Grant No. 12072317), the Natural Science Foundation of Zhejiang Province (Grant No. LZ21A020002), the National Key R&D Program of China (Grant No. 2017YFA0204403), the Major Program of the National Natural Science Foundation of China (Grant No. 51590892), General Research Fund (GRF) Scheme (CityU 11247516, CityU 11209918, CityU 11216219, PolyU 15213619), Hong Kong; the Hong Kong Collaborative Research Fund (CRF) Scheme (C4026-17W) and the Theme-based Research Scheme (Ref. T13-402/17-N), and the Tianjin Research Program of Application Foundation and Advanced Technology of China (Grant no. 18JCYBJC20300).

References

Aoyagi, Y., Tsuru, T., Shimokawa, T., 2014. Crystal plasticity modeling and simulation considering the behavior of the dislocation source of ultrafine-grained metal. Int. J. Plast. 55, 43-57.

Argon, A.S., 1979. Plastic-deformation in metallic glasses. Acta Metall. 27, 47-58.

Ashby, M.F., 1999. Materials section in mechanical design. Butterworth-Heinemann.

Barai, P., Weng, G.J., 2009. Mechanics of very fine-grained nanocrystalline materials with contributions from grain interior, GB zone, and grain-boundary sliding. Int. J. Plast. 25, 2410-2434.

Beyerlein, I.J., Zhang, X., Misra, A., 2014. Growth twins and deformation twins in metals. Annu. Rev. Mater. Res. 44, 329-363.

Bleck, W., 1996. Cold-rolled, high-strength sheet steels for auto applications. JOM 48, 26-30.

Bouaziz, O., Allain, S., Scott, C.P., Cugy, P., Barbier, D., 2011. High manganese austenitic twinning induced plasticity steels: a review of the microstructure properties relationships. Curr. Opin. Solid State Mat. Sci. 15,141-168.

Bouaziz, O., Zurob, H., Huang, M., 2013. Driving force and logic of development of advanced high strength steels for automotive applications. Steel Res. Int. 84, 937-947.

Cao, S.C., Zhu, L.L., Liu, J.B., Wu, G., Huang, W.X., Lu, J., 2018. Light-weight isometric-phase steels with superior strength-hardness-ductility combination. Scripta Mater. 154, 230-235.

Cao, Y., Ni, S., Liao, X., Song, M., Zhu, Y., 2018. Structural evolutions of metallic materials processed by severe plastic deformation. Mater. Sci. Eng. R 133, 1-59.

Chen, A.Y., Ruan, H.H., Wang, J., Chan, H.L., Wang, Q., Li, Q., Lu, J., 2011. The influence of strain rate on the microstructure transition of 304 stainless steel. Acta

Mater. 59, 3697-3709.

Chen, B., Lutker, K., Raju, S.V., Yan, J.Y., Kanitpanyacharoen, W., Lei, J.L., Yang, S.Z., Wenk, H.R., Mao, H.K., Williams, Q., 2012. Texture of nanocrystalline Nickel: Probing the lower size limit of dislocation activity. Science 338, 1448-145.

Chen, T.J., Yuan, R., Beyerlein, J., Zhou, C.Z., 2020. Predicting the size scaling in strength of nanolayered materials by a discrete slip crystal plasticity model. Int. J. Plast. 124, 247-260.

Cheng, J., Ghosh, S., 2013. Computational modeling of plastic deformation and shear banding in bulk metallic glasses. Comp. Mater. Sci. 69, 494-504.

Chowdhury, P., Sehitoglu, H., Maier, H.J., Rateick, R., 2016. Strength prediction in NiCo alloys-The role of composition and nanotwins, Int. J. Plast. 79, 237-258.

Dao, M., Lu, L., Asaro, R.J., De Hosson, J.T.M., Ma, E., 2007. Toward a quantitative understanding of mechanical behavior of nanocrystalline metals. Acta Mater. 55, 4041-4065.

Davis, S., Diegel, S. and Boundy, R., 2013. Transportation Energy Data Book. Oak Ridge National Laboratory, 4-17.

De Cooman, B.C., Chin, K.G. and Kim, J.K., 2011. High Mn TWIP steels for automotive applications. In: New Trends and Developments in Automotive System Engineering, Ed. Chiaberge, M., 101-128.

Deng, C., Sansoz, F., 2009. Near-ideal strength in gold nanowires achieved through microstructural design. ACS Nano 3, 3001-3008.

Dutta, T., Chauniyal, A., Singh, I., Narasimhan, R., Thamburaja, P., Ramamurty, U., 2018. Plastic deformation and failure mechanisms in nano-scale notched metallic glass specimens under tensile loading. J. Mech. Phys. Solids 111, 393-413.

El Kadiri, H., Oppedal, A.L., 2010. A crystal plasticity theory for latent hardening by glide twinning through dislocation transmutation and twin accommodation effects. J. Mech. Phys. Solids 58, 613-624.

Falk, M.L., Langer, J.S., 1998. Dynamics of viscoplastic deformation in amorphous solids. Phys. Rev. E 57, 7192-7205.

Fan, G.J., Choo, H., Liaw, P.K., Lavernia, E.J., 2006. Plastic deformation and fracture of ultrafine-grained Al-Mg alloys with a bimodal grain size distribution. Acta Mater. 54, 1759-1766.

Fang, T.H., Li, W.L., Tao, N.R., Lu, K., 2011. Revealing extraordinary intrinsic tensile plasticity in gradient nano-grained copper. Science 331, 1587-1590.

Farbaniec, L., Dirras, G., Krawczynska, A., Mompiou, F., Couque, H., Naimi, F., Bernard, F., Tingaud, D., 2014. Powder metallurgy processing and deformation characteristics of bulk multimodal nickel. Mater. Character. 94, 126-137.

Frommeyer, G., Brux, U. and Neumann, P., 2003. Supra-ductile and high-strength manganese-TRIP/TWIP steels for high energy absorption purposes. ISIJ Int43, 438-446.

Froseth, A., Derlet, P.M. and Van Swygenhoven, H., 2004. Grown-in twin boundaries affecting deformation mechanisms in nc-metals. Appl. Phys. Lett. 85, 5863-5865.

Gao, Y. F., 2006. An implicit finite element method for simulating inhomogeneous deformation and shear bands of amorphous alloys based on the free-volume model. Modelling Simul. Mater. Sci. Eng. 14, 1329-1345.

Grady, D. E., 1992. Properties of a n adiabatic shear band process zone. J. Mech. Phys. Solids 40, 1197-1215.

Greer, A.L., Cheng, Y.Q., Ma, E., 2013. Shear bands in metallic glasses. Mater. Sci. Eng. R 74, 71-132.

Grest, G.S., Cohen, M.H., 1981. Liquids, Glasses, and the Glass Transition: A Free-Volume Approach. Adv. Chem. Phys. 48, 455-525.

Gu, P., Dao, M., Asaro, R.J., Suresh, S., 2011. A unified mechanistic model for size dependent deformation in nanocrystalline and nanotwinned metals. Acta Mater. 59, 6861-6868.

Guerses, E., El Sayed, T., 2011. A variational multiscale constitutive model for nanocrystalline materials. J. Mech. Phys. Solids 59, 732-749.

Hahn, E. N., Meyers, M. A., 2015. Grain-size dependent mechanical behavior of nanocrystalline metals. Mater. Sci. Eng. A 646, 101-134.

Haouala, S., Lucarini, S., LLorca, J., Segurado, J., 2020. Simulation of the Hall-Petch effect in FCC polycrystals by means of strain gradient crystal plasticity and FFT homogenization. J. Mech. Phys. Solids 134, 103755.

Hasan, M.N., Liu, Y.F., An, X.H., Gu, J., Song, M., Cao, Y., Li, Y.S., Zhu, Y.T., Liao, X.Y., 2019. Simultaneously enhancing strength and ductility of a high-entropy alloy via gradient hierarchical microstructures. Int. J. Plast. 123, 178-195.

Hirth, J.P., Wangb, J., Tomé, C.N., 2016. Disconnections and other defects associated with twin interfaces. Prog. Mater. Sci. 83, 417-471

Huang, Q., Yu, D., Xu, B., Hu, W., Ma, Y., Wang, Y., Zhao, Z., Wen, B., He, J., Liu, Z., Tian, Y., 2014. Nanotwinned diamond with unprecedented hardness and stability. Nature 510, 250-253.

Huang, R., Suo, Z., Prevost, J. H., Nix, W. D., 2002. Inhomogeneous deformation in metallic glasses. J. Mech. Phys. Solids 50, 1011-1027.

Jiang, B., Weng, G.J., 2004. A theory of compressive yield strength of nano-grained ceramics. Int. J. Plast. 20, 2007-2026.

Jiang, M. Q., Dai, L. H., 2011. Shear band toughness of bulk metallic glass. Acta Mater. 59, 4525-4537.

Jiang, M.Q., Wang, W.H., Dai, L.H., 2009. Prediction of shear-band thickness in metallic glasses. Scripta Mater. 60, 1004-1007.

Jin, Z.H., Gumbsch P, Albe K, Ma E, Lu K, Gleiter H and Hahn H., 2008. Interactions between non-screw lattice dislocations and coherent twin boundaries in face-centered cubic metals. Acta Mater.56, 1126-1135.

Khan, A. and Liu, J., 2016. A deformation mechanism based crystal plasticity model of ultrafine-grained/nanocrystalline FCC polycrystals. Int. J. Plast. 86, 56-69.

Kocks, U. F., Mecking, H., 2003. The physics and phenomenology of strain hardening. Prog. Mater. Sci. 48, 171-273.

Kou, H.N., Lu, J., Li, Y., 2014. High-strength and high-ductility nanostructured and amorphous metallic materials. Adv. Mater 26, 5518-5524.

Lee, Z.H., Radmilovic, V., Ahn, B., Lavernia, E.J., Nutt, S.R., 2010. Tensile deformation and fracture mechanism of bulk bimodal ultrafine-grained Al–Mg alloy. Metall. Mater. Trans. A 41, 795-801.

Li, J., Weng, G.J., Chen, S., and Wu, X., 2017. On strain hardening mechanism in gradient nanostructures. Int. J. Plast. 88, 89-107.

Li, X., Dao, M., Eberl, C., Hodge, A.M., Gao, H., 2016. Fracture, fatigue, and creep of nanotwinned metals. MRS Bull. 41, 298-304.

Li, X.Y., Lu. K., 2017. Playing with defects in metals. Nat. Mater. 16, 700-701.

Li, X.Y., Wei, Y.J., Lu, L., Lu, K., Gao, H.J., 2010. Dislocation nucleation governed softening and maximum strength in nano-twinned metals. Nature 464, 877-880.

Liddicoat, P.V., Liao, X.Z., Zhao, Y.H., Zhu, Y.T., Murashkin, M.Y., Lavernia, E.J., Valiev, R.Z. and Ringer, S.P., 2010. Nanostructural hierarchy increases the strength of aluminium alloys. Nat. Commun. 1, 63(1-7).

Lim, H., Lee, M.G., Kim, J.H., Adams, B.L., Wagoner, R.H., 2011. Simulation of polycrystal deformation with grain and grain boundary effects. Int. J. Plast. 27, 1328-1354.

Liu, X., Sun, L., Zhu, L., Liu, J., Lu, K., Lu, J., 2018. High-order hierarchical nanotwins with superior strength and ductility. Acta Mater. 149, 397-406.

Liu, X.C., Zhang, H.W., Lu, K., 2013. Strain-induced ultrahard and ultrastable nanolaminated structure in Nickel. Science 342, 337-340.

Llewellyn, D.T., Hillis, D.J., 1996. Dual phase steels. Ironmak Steelmak 23, 471-478.

Lu, K., 2010. The future of metals. Science328, 319-320.

Lu, K., 2014. Making strong nanomaterials ductile with gradients. Science 345, 1455-1456.

Lu, K., Lu, L., Suresh, S., 2009. Strengthening materials by engineering coherent internal boundaries at the nanoscale. Science 324, 349-352.

Lu, L., Shen, Y., Chen, X., Qian, L., Lu, K., 2004. Ultrahigh strength and high electrical conductivity in copper. Science 304, 422-426.

Lu, L., Chen, X., Huang, X., Lu, K., 2009. Revealing the maximum strength in nanotwinned copper. Science 323, 607-610.

Lu, X.C., Zhao, J.F., Wang, Z.W., Gan, B., Zhao, J.W., Kang, G.Z., Zhang, X., 2020. Crystal plasticity finite element analysis of gradient nanostructured TWIP steel. Int. J. Plast. 130, 102703.

Ma, E., Zhu, T., 2017. Towards strength-ductility synergy through the design of heterogeneous nanostructures in metals. Mater. Today 20, 323-331.

Meyers, M.A., Mishra, A., Benson, D.J., 2006. Mechanical properties of nanocrystalline materials. Prog. Mater. Sci. 51, 427-556.

Militzer, M., 2002. Materials science: a synchrotron look at steel. Science 298, 975-976.

Ming, K.S., Bi, X.F., Wang, J., 2019. Strength and ductility of CrFeCoNiMo alloy with hierarchical microstructures. Int. J. Plast. 113, 255-268.

Mirkhani, H., Joshi, S.P., 2011. Crystal plasticity of nanotwinned microstructures: A discrete twin approach for copper. Acta Mater. 59,5603-5617.

Naik, S.N., Walley, S.M., 2020. The Hall-Petch and inverse Hall-Petch relations and the hardness of nanocrystalline metals. J. Mater. Sci. 55, 2661-2681.

Ovid’ko I.A., Valiev, R.Z., Zhu, Y.T., 2018. Review on superior strength and enhanced ductility of metallic nanomaterials. Prog. Mater. Sci. 94, 462-540.

Pan, D., Inoue, A., Sakurai, T., Chen, M.W., 2008. Experimental characterization of shear transformation zones for plastic flow of bulk metallic glasses. Proc. Natl. Acad. Sci. USA 105, 14769-14772.

Pande, C. S., Cooper, K. P., 2009. Nanomechanics of Hall-Petch relationship in nanocrystalline materials. Prog. Mater. Sci. 54, 689-706.

Rashid, M.S. 1981. Dual phase steels. Annu. Rev. Mater. Sci. 11, 245-266.

Ritchie, R.O., 2011. The conflicts between strength and toughness. Nat. Mater. 10, 817-822.

Richter, G., Hillerich, K., Gianola, D. S., Monig, R., Kraft, O., Volkert, C. A., 2009. Ultrahigh strength single crystalline nanowhiskers grown by physical vapor deposition. Nano Lett. **9,** 3048-3052.

Rupert, T.J., Rupert, T.J., Trelewicz, J.R., Schuh, C.A., 2012. Grain boundary relaxation strengthening of nanocrystalline Ni-W alloys. J. Mater. Res. 27, 1285-1294.

Schioz, J., Jacobsen, K. W., 2003. A maximum in the strength of nanocrystalline copper. Science 301, 1357-1359.

Schuh, C., Nieh, T. & Yamasaki, T., 2002. Hall-Petch breakdown manifested in abrasive wear resistance of nanocrystalline nickel. Scr. Mater. 46, 735-740.

Shin,Y.A., Yin, S., Li, X.Y., Lee, S., Moon, S., Jeong, J., Kwon, M., Yoo, S.J., Kim, Y.M., Zhang, T., Gao, H.J., Oh, S.H., 2016. Nanotwin-governed toughening mechanism in hierarchically structured biological materials. Nat. Commun. 7, 10772(1-10).

Simchi, H., Simchi, A., 2009. Tensile and fatigue fracture of nanometric alumina reinforced copper with bimodal grain size distribution. Mater. Sci. Eng. A 507, 200-206.

Spaepen, F., 1977. A microscopic mechanism for steady state inhomogeneous flow in metallic glasses. Acta Metall. 25, 407-415.

Spaepen, F., 2006. Homogeneous flow of metallic glasses: a free volume perspective. Scripta Mater. 54, 363-367

Steif, P.S., 1983. Ductile versus brittle behavior of amorphous metals. J. Mech. Phys.Solids 31, 359-388.

Sun, L.G., He, X.Q., Lu, J., 2018. Nanotwinned and hierarchical nanotwinned metals: a review of experimental, computational and theoretical efforts. npj Comput. Mater., 4, 1-18.

Sun, L.G., Wu, G., Wang, Q., Lu, J., 2020. Nanostructural metallic materials: Structures and mechanical properties. Mater. Today 38, 114-135.

Tan, X.P., Kok, Y.H., Tan, Y.J., Descoins, M., Mangelinck, D., Tor, S.B., Leong, K.F., Chua, C.K., 2015. Graded microstructure and mechanical properties of additive manufactured Ti-6Al-4V via electron beam melting. Acta Mater. 97, 1-16.

Thamburaja, P., Ekambaram, R., 2007. Coupled thermo-mechanical modelling of bulk metallic glasses: Theory, finite-element simulations and experimental verification. J. Mech. Phys. Solids 55, 1236-1273.

Tian, L., Cheng, Y. Q., Shan, Z. W., Li, J., Wang, C. C., Han, X. D., Sun, J., Ma, E., 2012. Approaching the ideal elastic limit of metallic glasses. Nat. Commun. **3,** 609 (2012).

Tian, Y., Xu, B., Yu, D., Ma, Y., Wang, Y., Jiang, Y., Hu, W., Tang, C., Gao, Y., Luo, K., Zhao, Z., Wang, L., Wen, B., He, J., Liu Z. Y., 2013. Ultrahard nanotwinned cubic boron nitride. Nature 493, 385-388.

Trelewicz, J.R., Schuh, C.A., 2007. The Hall-Petch breakdown in nanocrystalline metals: a crossover to glass-like deformation. Acta Mater. 55, 5948-5958.

Tucker, G.J., Foiles, S.M., 2015. Quantifying the influence of twin boundaries on the deformation of nanocrystalline copper using atomistic simulations. Int. J. Plast. 65, 191-205.

Wang, H.T., Tao, N.R., Lu, K., 2013. Architectured surface layer with a gradient nanotwined structure in a Fe-Mn austenitic steel. Scr. Mater. 68, 22-27.

Wang, Y.M., Chen, M.W., Zhou, F.H., Ma, E., 2002. Extraordinarily high tensile ductility in a nanostructured metal. Nature 419, 912-915.

Wei, Y.J., 2011. Scaling of maximum strength with grain size in nanotwinned fcc metals. Phys. Rev. B 83,132104.

Wei, Y.J., Li, Y.Q., Zhu, L.C., Liu, Y., Lei X.Q., Wang, G., Wu, Y.X., Mi, Z.L., Liu J.B., Wang, H.T., Gao, H.J., 2014. Evading the strength-ductility trade-off dilemma in steel through gradient hierarchical nanotwins. Nat. Comm. 5, 3580(1-8).

Weng, G. J., 1990. The overall elastoplastic stress–strain relation of dual-phase metals.

J. Mech. Phys. Solids 38, 419-441.

Wu, H., Fan, G., 2020. An overview of tailoring strain delocalization for strength-ductility synergy. Prog. Mater. Sci. 113, 100675.

Wu, G., Chan, K.C., Zhu, L., Sun, L., Lu, J., 2017. Dual-phase nanostructuring as a route to high-strength magnesium alloys. Nature 545, 80-83.

Wu, G., Sun, L.G., Zhu, L.L., Liu, C., Wang, Q., Bao, Y., Lu., J., 2020a. Near-ideal strength and larger compressive deformability of a nano-dual-phase glass-crystal alloy in sub-micron. Scripta Mater. 188, 290-295.

Wu, G., Zhang, J.Y., Liu, C., Wang, Q., Lu., J., 2020b. Ductility of an ultrastrong glass-crystal nano-dual-phase alloy in sub-micron. Scripta Mater. 183, 17-21.

Wu, X.L., Jiang, P., Chen, L., Yuan, F.P., Zhu, Y.T., 2014. Extraordinary strain hardening by gradient structure. Proc. Natl. Acad. Sci. U. S. A. 111, 7197-7201.

Yang, M.X., Pan, Y., Yuan F.P., Zhu, Y.T., Wu, X.L., 2016. Back stress strengthening and strain hardening in gradient structure. Mater. Res. Lett. 4, 145-151.

Yang, Q., Mota, A., Ortiz, M. A., 2006. Finite-Deformation Constitutive Model of Bulk Metallic Glass Plasticity. Comput. Mech. 37, 194-204.

Yuan, S.L., Zhu, Y.X., Liang, S., Huang, M.S., Li, Z.H., 2019. Dislocation-density based size-dependent crystal plasticity framework accounting for climb of piled up dislocations at elevated temperature. Mech. Mater. 134, 85-97.

Yu, Z.Y., Cantwell, P.R., Gao, Q., Yin, D., Zhang, Y.Y., Zhou, N.X., Rohrer, G.S., Widom, M., 2017.Segregation-induced ordered superstructures at general grain boundaries in a nickel-bismuth alloy. Science 358, 97-101.

Zhang, W. X., Wang, T. J., and Chen, X., 2010. Effect of Surface/Interface Stress on the Plastic Deformation of Nanoporous Materials and Nanocomposites. Int. J. Plast. 26, 957-975.

Zhao, Y.H., Topping, T., Bingert, J.F., Thornton, J.J., Dangelewicz, A.M., Li, Y., Liu, W., Zhu, Y.T., Zhou, Y.Z., Lavernia, E.J., 2008. High tensile ductility and strength in bulk nanostructured nickel. Adv. Mater. 20, 3028-3033.

Zheng, Y.G., Lu, J., Zhang, H.W. and Chen, Z., 2009. Strengthening and toughening by interface-mediated slip transfer reaction in nanotwinned copper. Scr. Mater. 60, 508-511.

Zhou, X., Feng, Z., Zhu, L., Xu, J., Miyagi, L., Dong, H., Sheng, H., Wang, Y., Li, Q., Ma, Y., Zhang, H., Yan, J., Tamura, N., Kunz, M., Lutker, K., Huang, T., Hughes, D.A., Huang, X., Chen, B., 2020. High pressure strengthening in ultra-fine-grained metals. Nature 579, 67-72.

Zhu, L.L., Lu, J., 2012. Modelling the plastic deformation of nanostructured metals with bimodal grain size distribution. Int. J. Plast. 30-31, 166-184.

Zhu, L.L, Guo, X., Lu, J, 2014. Surface stress effects on the yield strength in nanotwinned polycrystal fcc metallic nanowires. ASME-J. Appl. Mech. 81, 101002.

Zhu, L.L., Ruan, H.H., Li, X.Y., Dao, M., Gao, H.J., Lu, J., 2011. Modeling grain size dependent optimal twin spacing for achieving ultimate high strength and related high ductility in nanotwinned metals. Acta Mater. 59, 5544-5557.

Zhu, L.L., Ruan, H.H., Chen, A.Y., Guo, X., Lu, J., 2017. Microstructures-based constitutive analysis of mechanical properties of gradient-nanostructured 304 stainless steels. Acta Mater.128, 375-390.

Zhu, L.L., Wen, C.S., Gao, C.Y, Guo, X., Chen, Z., Lu, J., 2019. Static and dynamic mechanical behaviors of gradient-nanotwinned stainless steel with a composite structure: Experiments and modeling. Int. J. Plast. 114, 272-288.

Zhu, T., Li, J., 2010. Ultra-strength materials. Prog. Mater. Sci. 55, 710-757.

Zhu, T., Li, J., Samanta, A., Kim, H.G. and Suresh, S., 2007. Interfacial plasticity governs strain rate sensitivity and ductility in nanostructured metals. Proc. Natl. Acad. Sci. 104, 3031-3036.

Zhu, Y. T., Liao, X. Z., 2004. Nanostructured metals: retaining ductility. Nat. Mater. 3, 351-352.

Zinkle, S.J., Busby, J.T., 2009. Structural materials for fission & fusion energy. Mater. Today 12, 12-19.

Table 1.

Description, symbol, magnitude, and equation in which the different parameters of the models appear

Parameter (Unit)	Symbol	Magnitude
Grain size (nm)	d_{G0}	6
Elastic modulus (GPa)	E_C, E_G	88,45.1
Shear modulus (GPa)	μ_C, μ_G	38,22
Poisson's ratio	ν_C, ν_G	0.31,0.309
Magnitude of the Burgers vector (nm)	b	0.256
Taylor factor	M	3.06
Taylor constant	α	0.33
Thickness of GBDPZ (nm)	d_{GBDPZ}	3.6
Dislocation density related parameters	C_0, C_1, C_2	3.75×10^{-5}, 2.12×10^{4}, 1.74×10^{4}
Dynamic recovery constant	k_{20}	18.5
Proportionality factor	ψ	0.2
Dynamic recovery constant	n	12.25
Reference strain rate (s^{-1})	$\dot{\varepsilon}_r$	1.75
Geometric factor	$\phi^{TB}, \phi_i (i = 1, 2)$	0.5~1.5
Frequency of atomic vibration(s^{-1})	f_0	$\sim1.0\times10^{13}$
The activation energy (J)	ΔG^m	1×10^{-19}
Geometrical factor of order unity	α_o	0.05
Critical volume (m^3)	$v*$	15×10^{-30}
Number of atomic jumps	n_D	10
Atomic volume (m^3)	Ω	2.0×10^{-30}
Thermal softening coefficient (K^{-1})	S_T	7.0×10^{-2}
Thermal diffusivity coefficient (m^2s^{-1})	D_T	8.2×10^{-6}
Shear strain rate(s^{-1})	$\dot{\gamma}$	1.0×10^{-6}
Free volume softening coefficient	S_v	1.5×10^{-2}
Characterizes the local dilatation ability	R	2.0×10^{-2}
The diffusion coefficient (m^2s^{-1})	D_f	2.4×10^{-15}
Aspect ratio of the samples	α_r	3
Grain size evolution function parameters(nm)	c_0, c_3	4.5, 1.5
Grain size evolution function parametera	c_1, c_2	1.3, 0.1
Volume fraction evolution function parameter	a_1, a_2	0.3, 0.05
Volume fraction evolution function parameter	b_0, b_1, b_2	0.9,0.4, 0.12

Figure Captions

Figure 1. Transmission electron microscopy (TEM) images showing (a) homogenous distribution of nanograins in the MG matrix, (b) the multiple shear bands in a larger micropillar, and (c) the fiber-like structures in smaller micropillars. The stress-strain curves shown in (d) and (e) were obtained by compressing micropillars of Mg-based NDPGC alloy with different diameters (D), which shows brittle and ductile behaviors, respectively. The yield strength is defined as the stress at 0.2% plastic strain for the micropillars showing plasticiy.

Figure 2. Schematic drawings of the composite structure model for the NDPGC alloys, consisting of nanosized crystals and MG phase with feature dimensions (size and spacing of nanocrystals) less than 10 nm.

Figure 3. The schematic drawings of the first type of hierarchical structure in NDPGC alloys, in which the material is separated into two regions in micrometer scale. They are named MG flow-activated and MG flow unactivated regions, which possess both MG and crystalline phases.

Figure 4. The schematic drawings for the second type of hierarchical structure in a NDPGC alloy in which the reorganization of nanograins occurs, forming the high NG and low NG density zones.

Figure 5. (a) The comparison of the simulation and experimental results in terms of stress-strain curves and (b) the variations of free volume concentration with strain in a bulk metallic glass (BMG) and in the MG phase of a Mg-based

NDPGC alloy.

Figure 6. Energy criterion for shear band multiplication: (a) energy dissipation for generating multiple shear bands, (b) deformation energy as functions of strain in a Mg-based NDPGC alloy, and (c) the number of shear band determined by the intersections of dissipation energy and deformation energy curves for the micropillar with the diameter of 1300 nm.

Figure 7. The comparisons between the simulations and experimental measurements for the number of shear band varied with the diameter of micropillars (a), and for the critical strain at which the corresponding shear band generated (b).

Figure 8. The comparisons between the simulation and experimental data for the constitutive behavior of smaller micropillars of Mg-based NDPGC alloy with the diameter of 300 nm.

Figure 9. The volume fractions of MG-FA and MG-FUA regions (a), the ones of HDGZ and LDGZ (b), and the grain size (c) as the functions of strain in Mg-based NDPGC alloy.

Figure 10. The predicted stress-strain relations of larger micropillars of Mg-based NDPGC alloy with different grain size.

Figure 11. The predictions based on the proposed criterion for the critical strain vs the shear band number for different diameters of pillars with the grain size of (a) 10 nm, (b) 20 nm and (c) 50 nm.

Figure 12. The predictions based on the proposed criterion for the critical strain vs the

diameter with different shear band number (a), the shear band number vs the diameter with different grain size (b), and the shear band number vs grain size with different dimeter (c).

Figure 13. The critical diameter of micropillars for generating the shear band as the function of the grain size. The blue region is for enabling to generate the shear band, and the red region is for no shear band generation.

Figure 14. The predictions based on the proposed model for the constitutive behavior (a), and the grain size varied with strain during deformation for the smaller pillars of Mg-based NDPGC alloys with different grain size.

Figure 15. The effect of a_2 on (a) the stress-strain relations of small micropillars and (b) the volume fraction of MG-FA region.

Figure 16. The predictions for the stress-strain relations of smaller micropillars with different parameter c_2 (a), the grain size as the function of strain with different c_2 (b)

Click here to access/download;Figure;fig1abc-ok3.tif

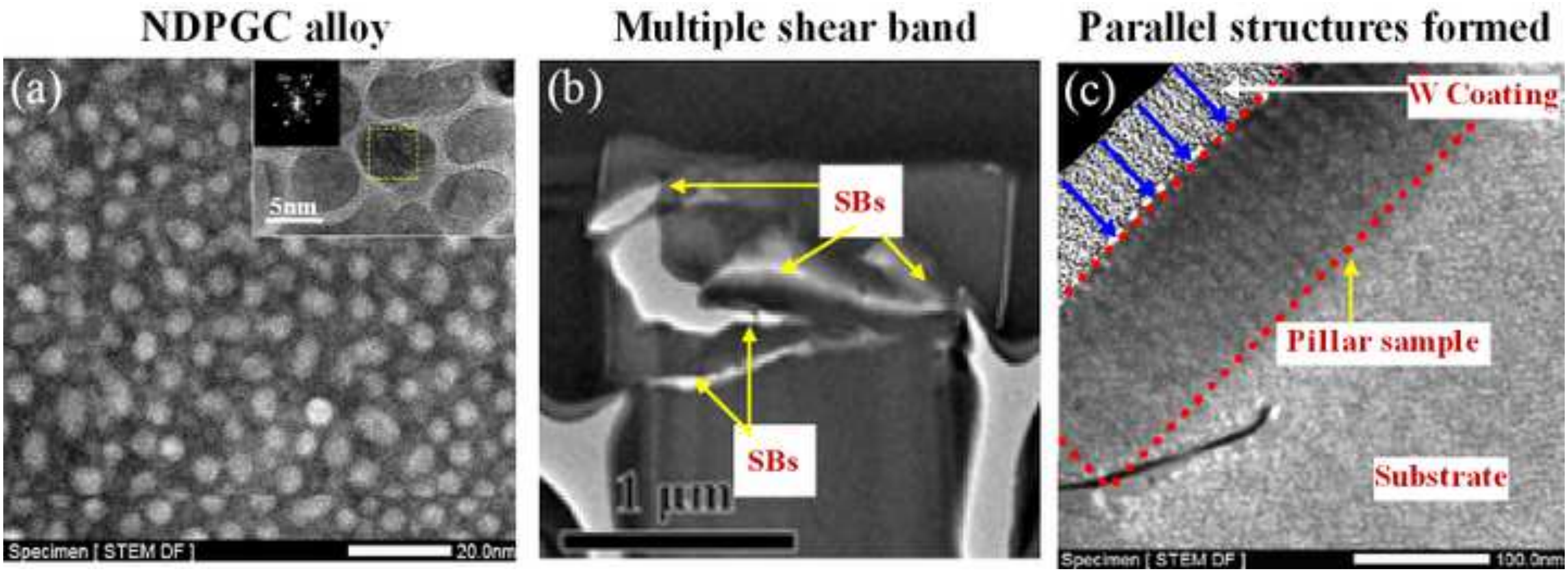
NDPGC alloy
Multiple shear band
Parallel structures formed
(a)
5nm
Specimen [STEM DF]
20.0nm
(b)
SBs
SBs
1 μm
(c)
W Coating
Pillar sample
Substrate
Specimen [STEM DF]
100.0nm

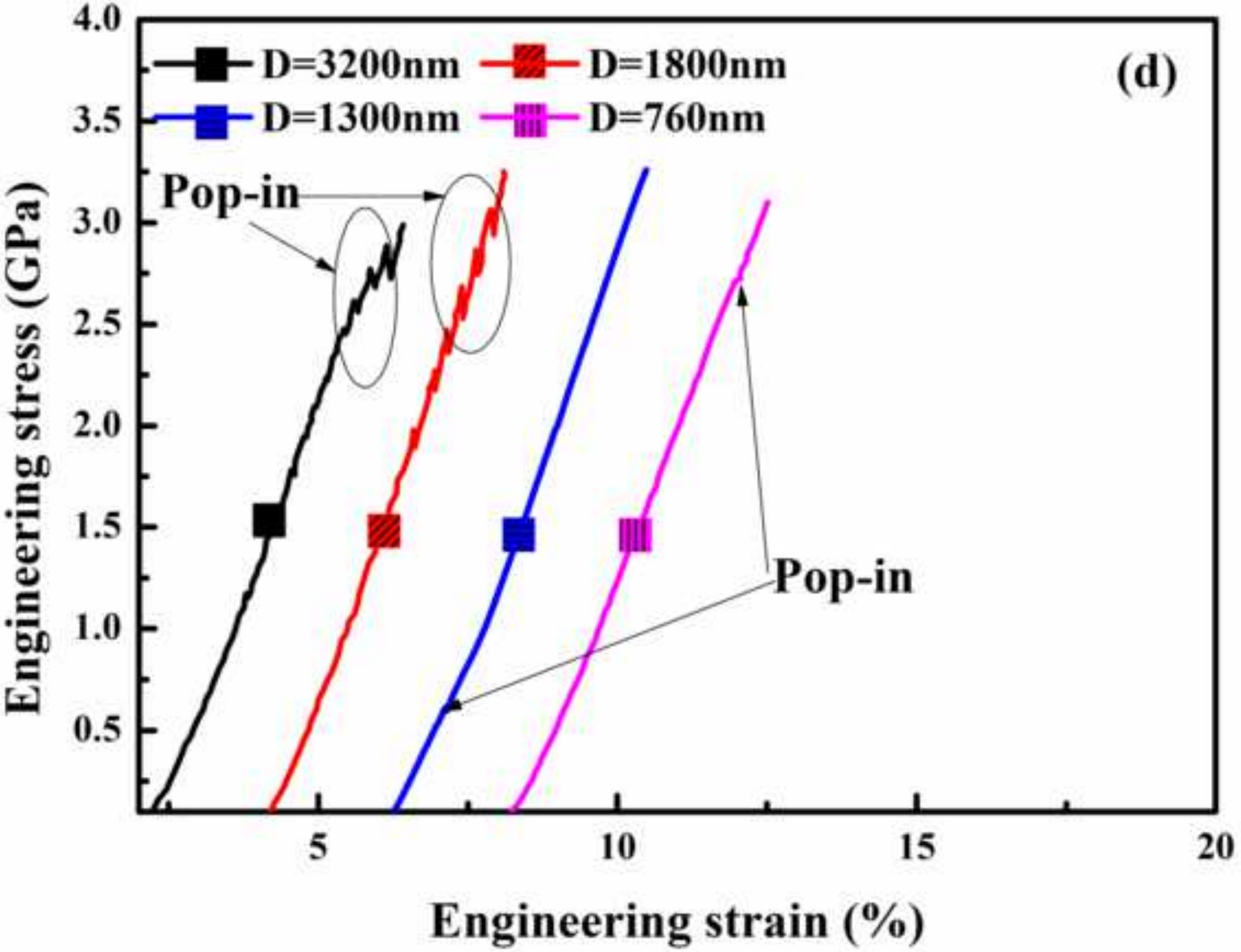
(d)
D=3200nm
D=1800nm
D=1300nm
D=760nm
Pop-in
Pop-in
Engineering stress (GPa)
Engineering strain (%)
4.0
3.5
3.0
2.5
2.0
1.5
1.0
0.5
5
10
15
20

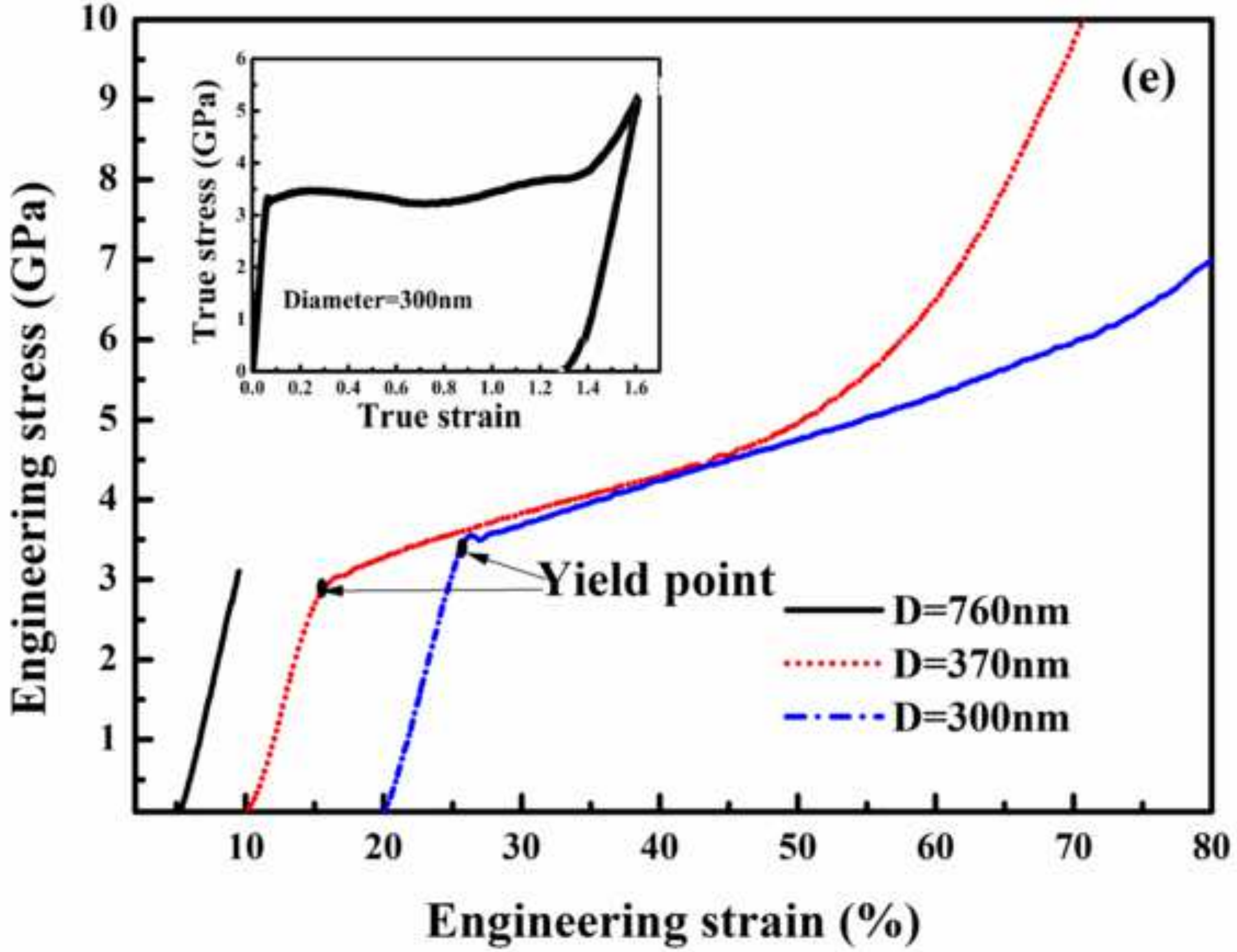
(e)
Engineering stress (GPa)
Engineering strain (%)
0
1
2
3
4
5
6
7
8
9
10
10
20
30
40
50
60
70
80
Yield point
D=760nm
D=370nm
D=300nm
True stress (GPa)
True strain
Diameter=300nm
0
1
2
3
4
5
6
0.0
0.2
0.4
0.6
0.8
1.0
1.2
1.4
1.6

fig2

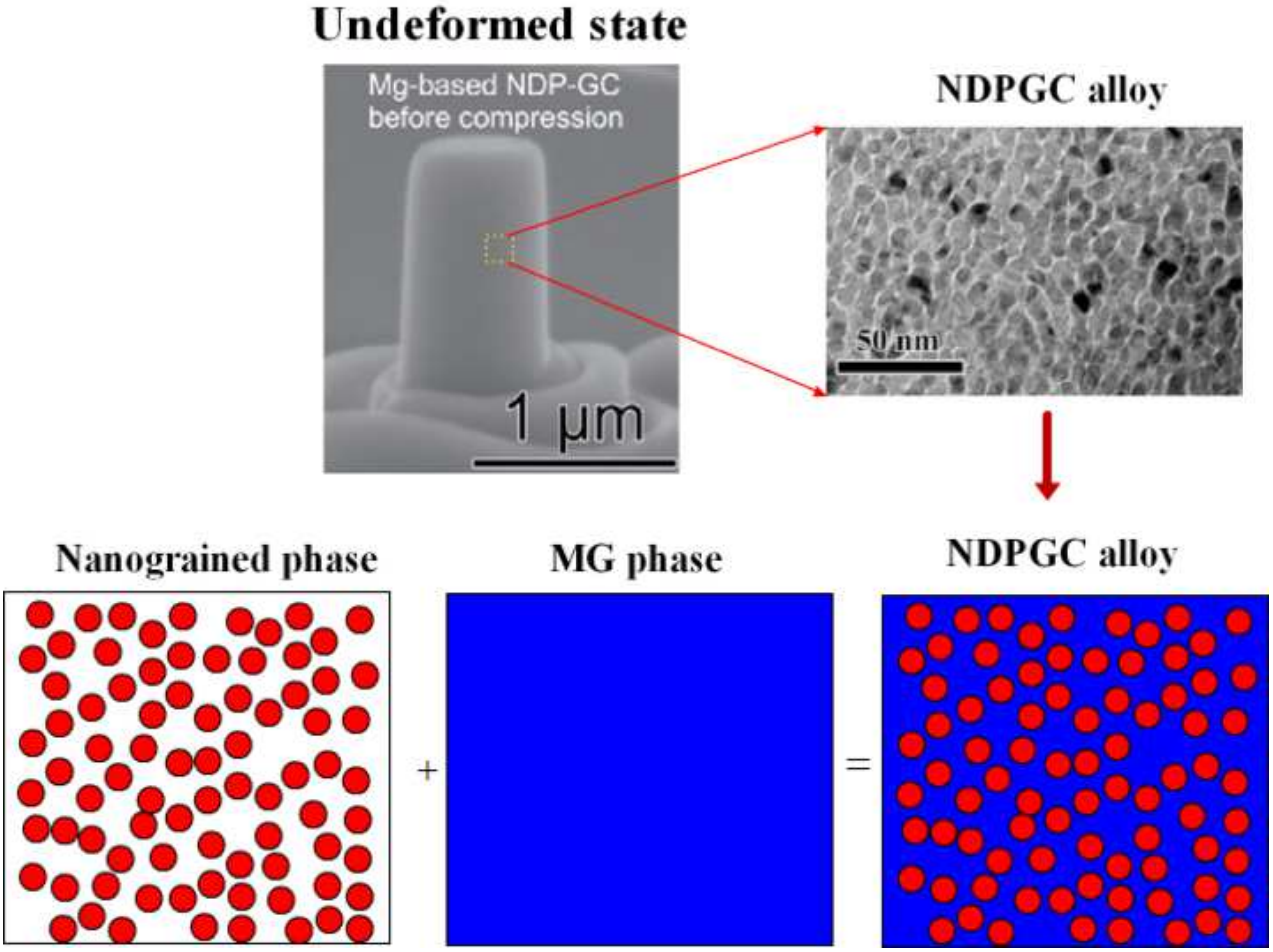
Undeformed state
Mg-based NDP-GC
before compression
1 µm
NDPGC alloy
50 nm
Nanograined phase
+
MG phase
=
NDPGC alloy

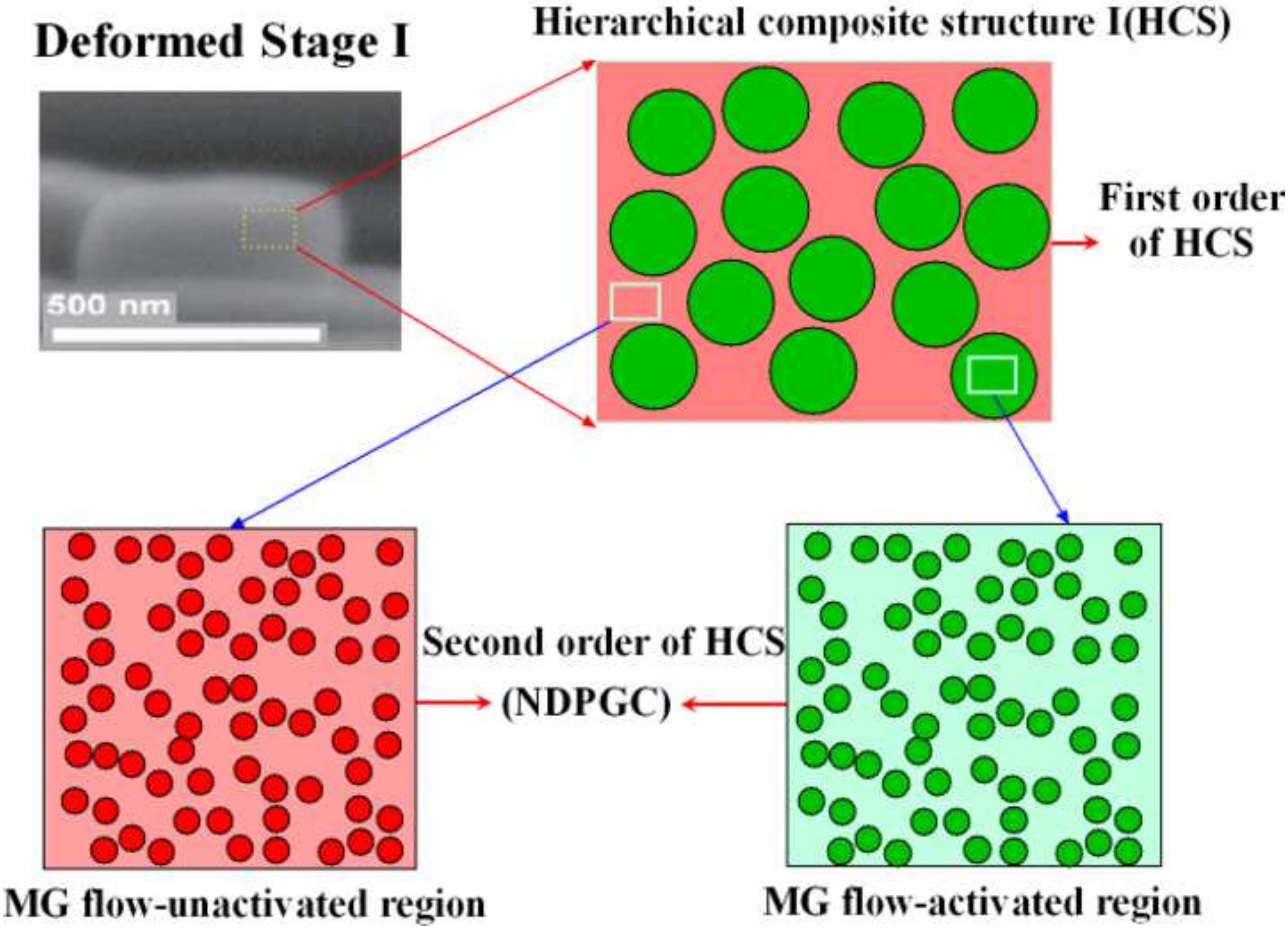
Deformed Stage I
Hierarchical composite structure I(HCS)
500 nm
First order of HCS
Second order of HCS
(NDPGC)
MG flow-unactivated region
MG flow-activated region

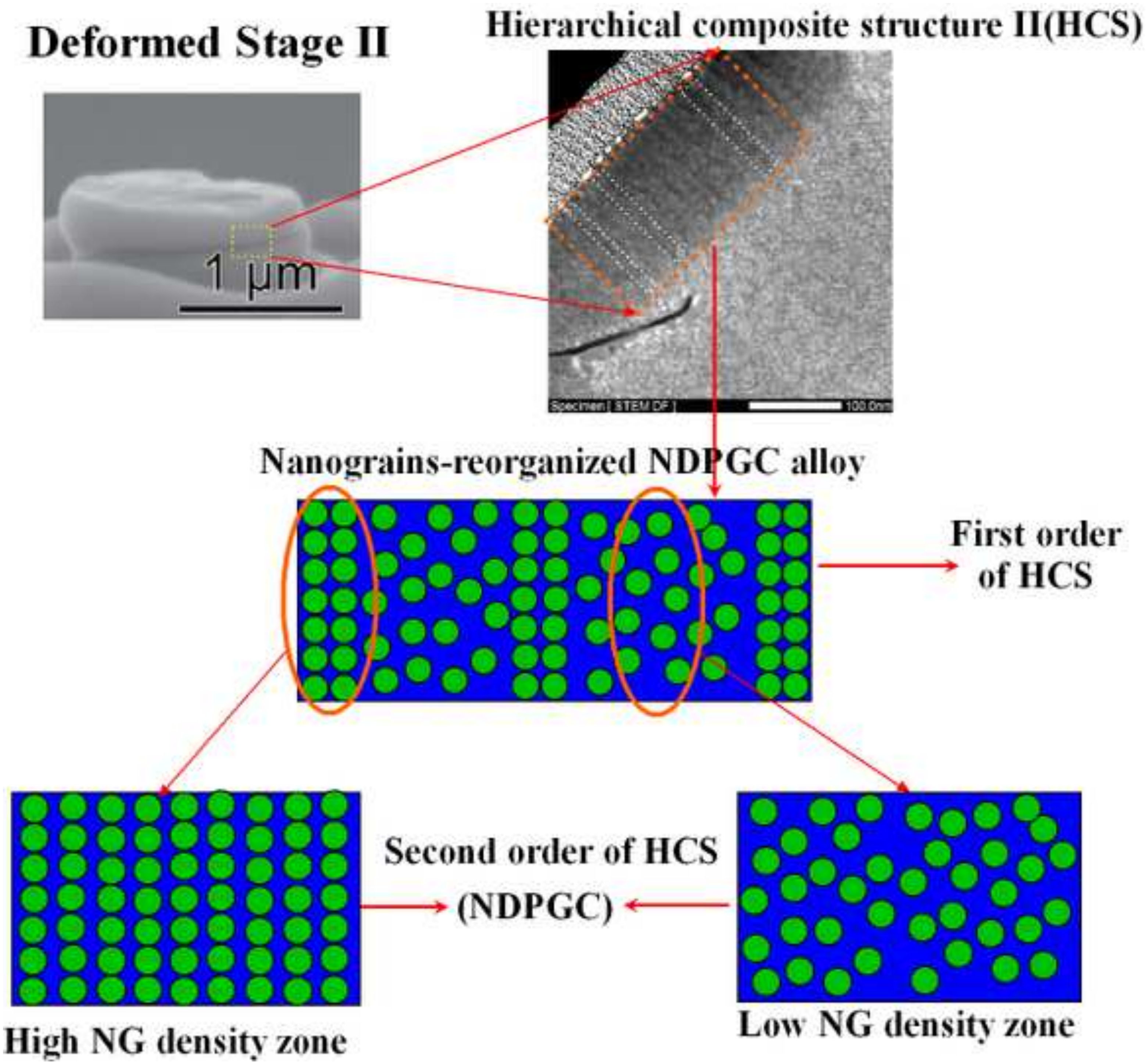
Deformed Stage II
Hierarchical composite structure II(HCS)
1 μm
Specimen [STEM DF]
100.0nm
Nanograins-reorganized NDPGC alloy
First order of HCS
Second order of HCS (NDPGC)
High NG density zone
Low NG density zone

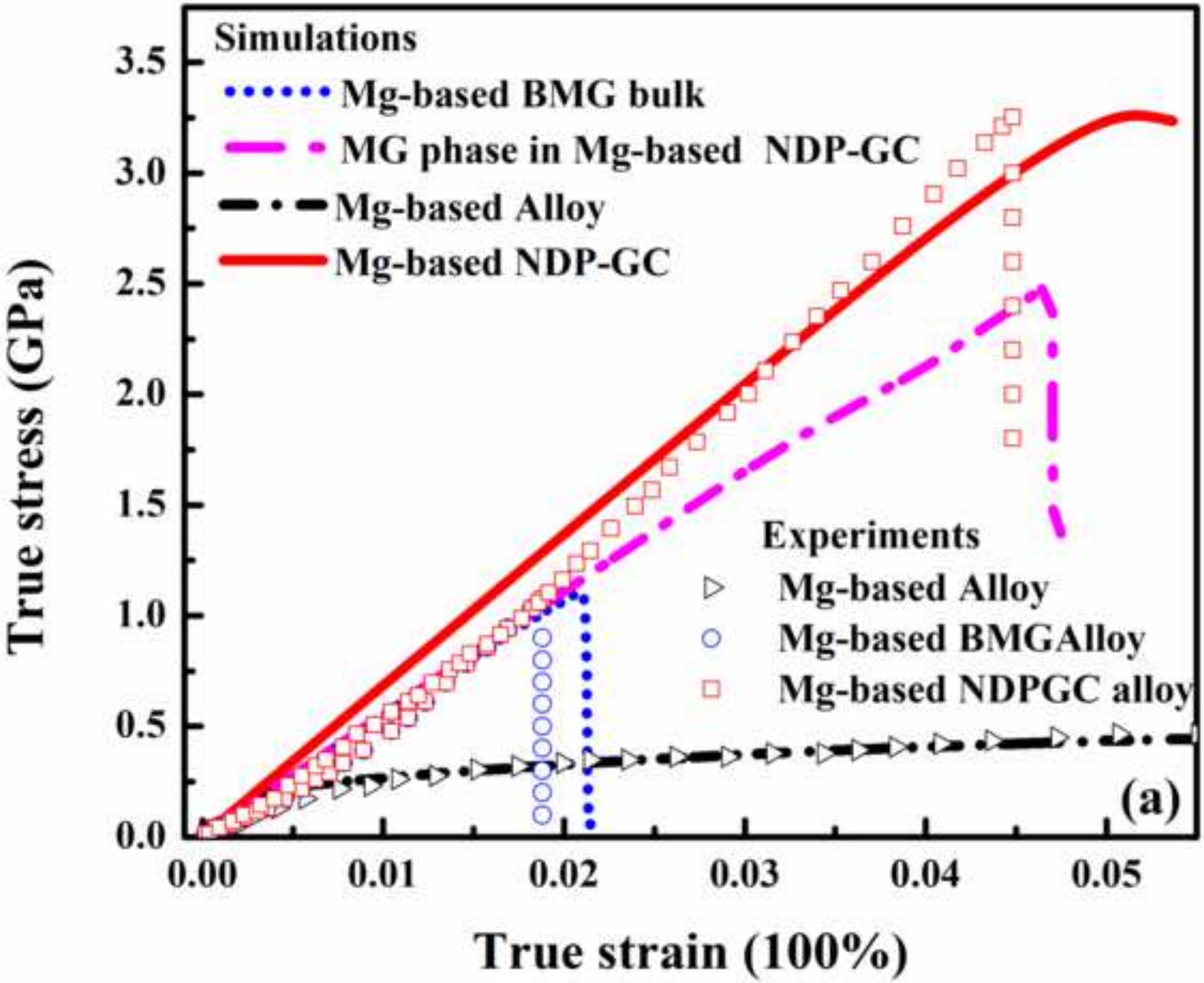
Simulations
Mg-based BMG bulk
MG phase in Mg-based NDP-GC
Mg-based Alloy
Mg-based NDP-GC
Experiments
▷ Mg-based Alloy
○ Mg-based BMGAlloy
□ Mg-based NDPGC alloy
(a)
True stress (GPa)
0.0
0.5
1.0
1.5
2.0
2.5
3.0
3.5
True strain (100%)
0.00
0.01
0.02
0.03
0.04
0.05

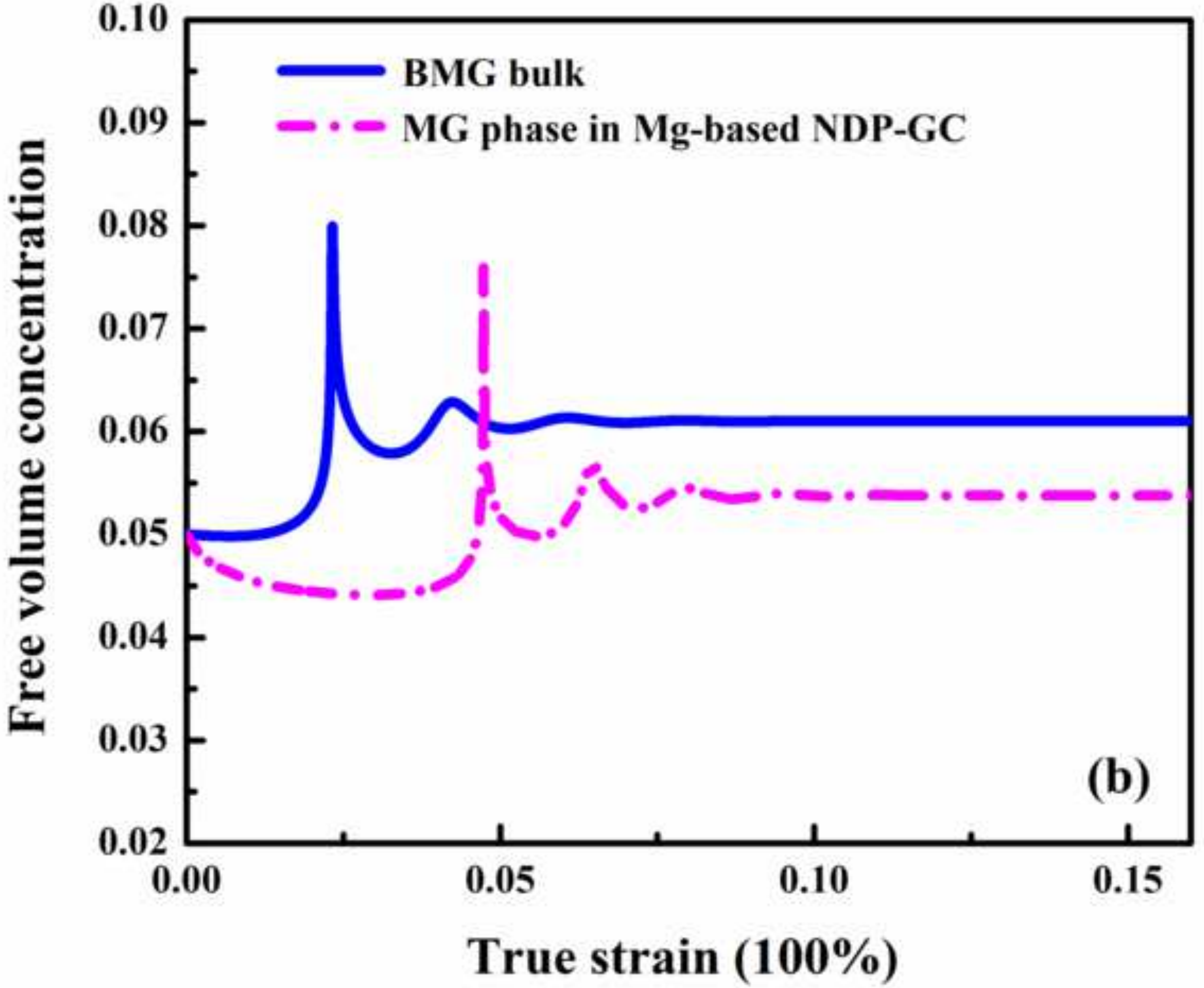
Free volume concentration
0.10
0.09
0.08
0.07
0.06
0.05
0.04
0.03
0.02
0.00
0.05
0.10
0.15
True strain (100%)
BMG bulk
MG phase in Mg-based NDP-GC
(b)

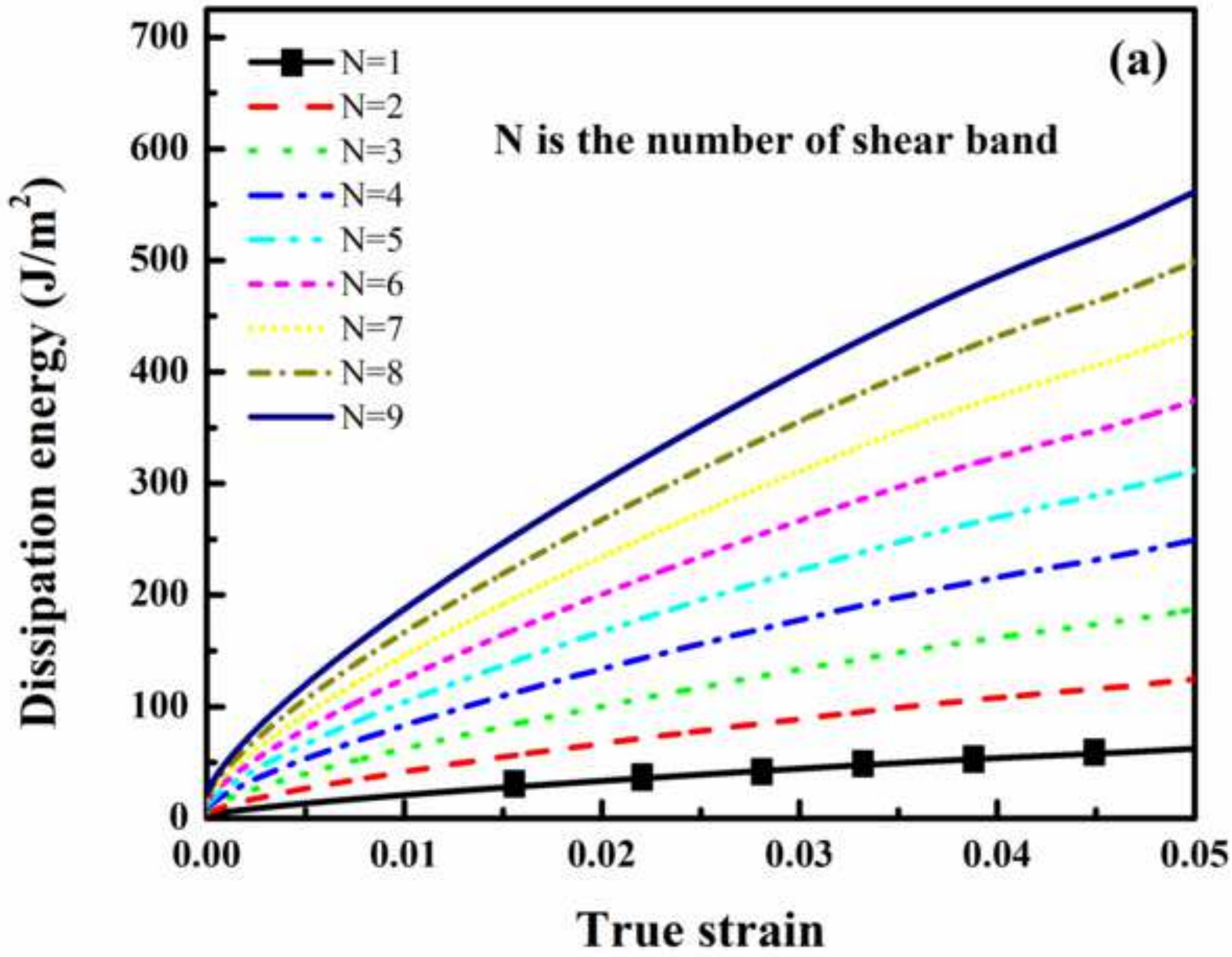
(a)
N is the number of shear band
N=1
N=2
N=3
N=4
N=5
N=6
N=7
N=8
N=9
Dissipation energy (J/m²)
0
100
200
300
400
500
600
700
True strain
0.00
0.01
0.02
0.03
0.04
0.05

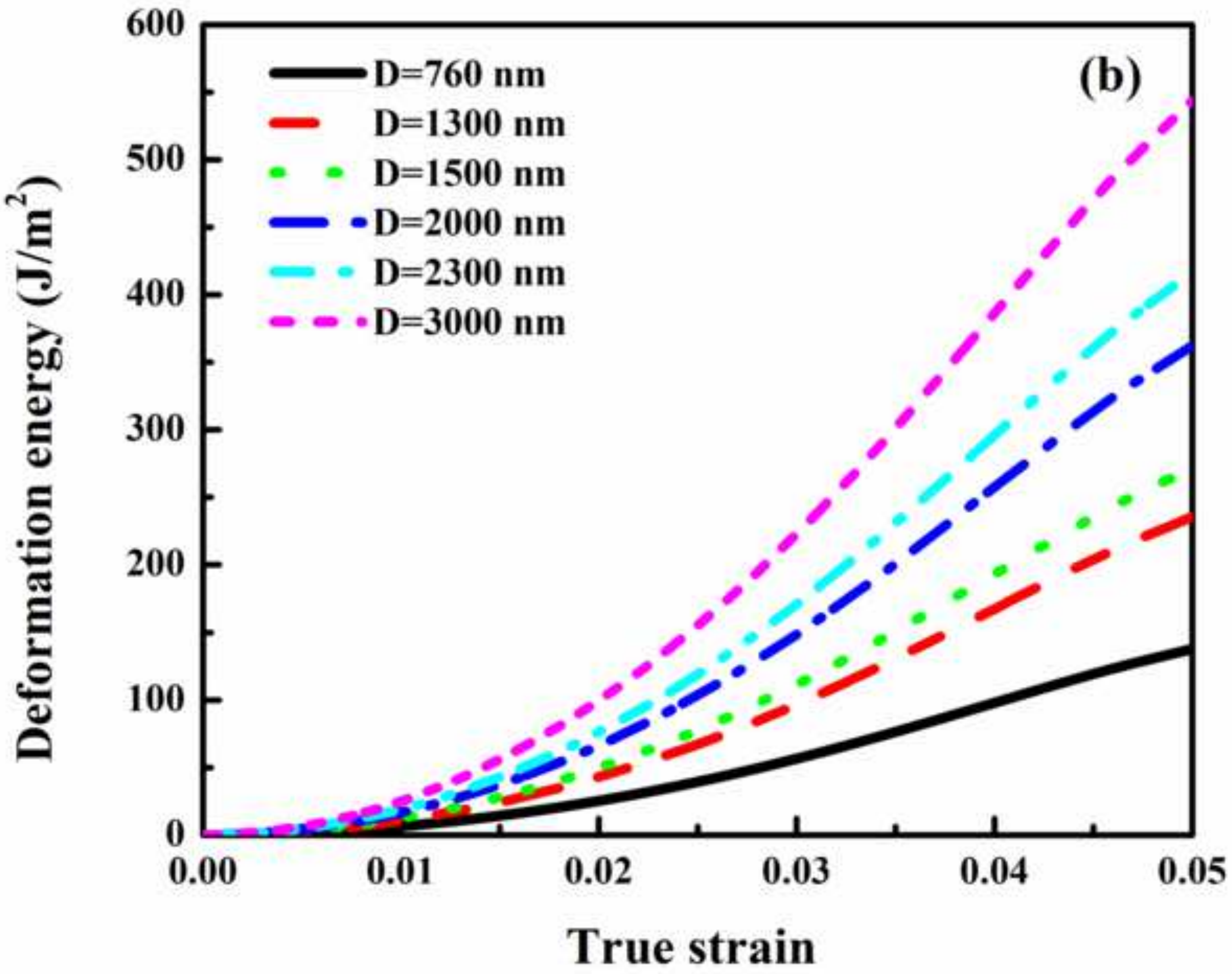
(b)
D=760 nm
D=1300 nm
D=1500 nm
D=2000 nm
D=2300 nm
D=3000 nm
Deformation energy (J/m^2)
0
100
200
300
400
500
600
0.00
0.01
0.02
0.03
0.04
0.05
True strain

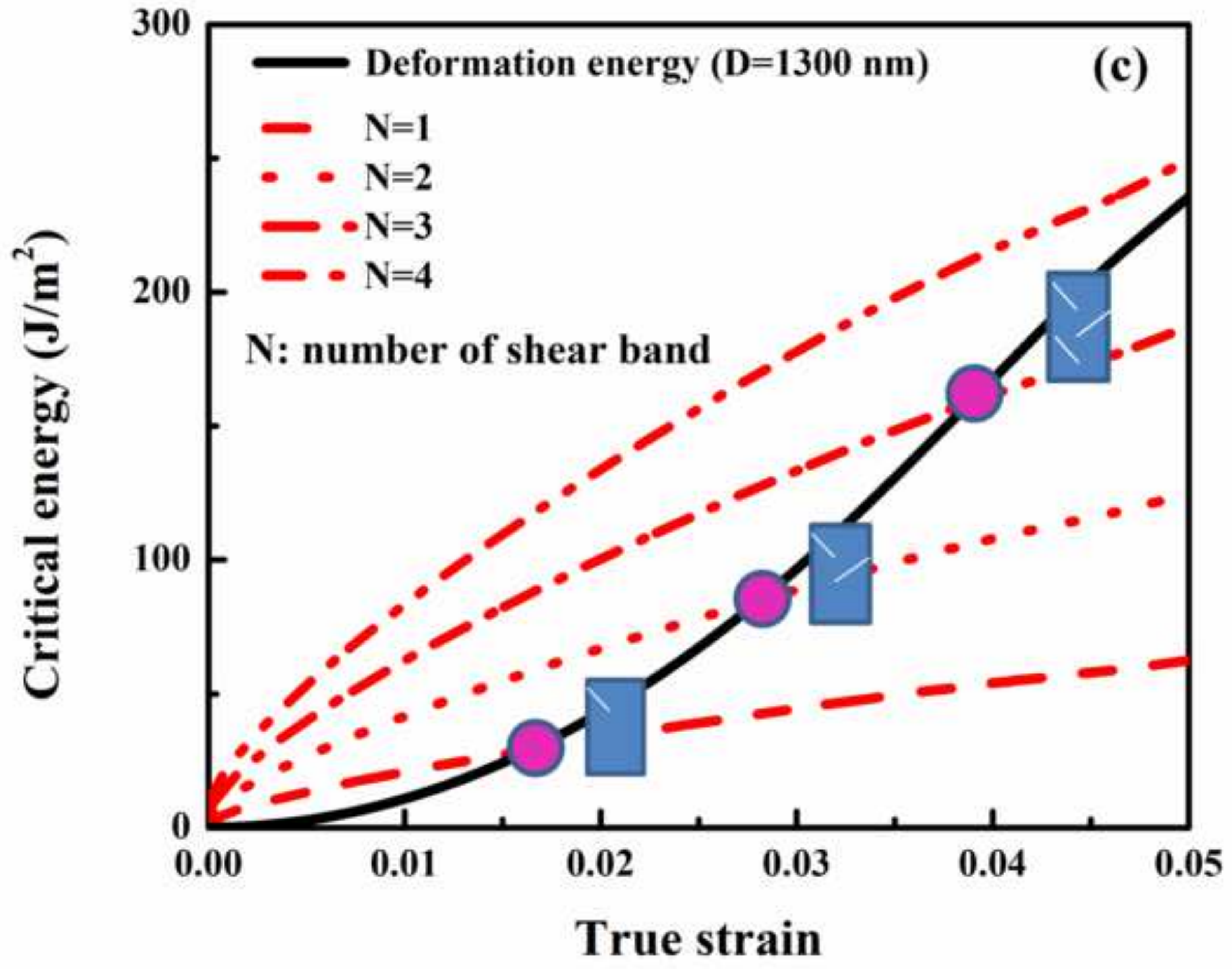
Deformation energy (D=1300 nm)
N=1
N=2
N=3
N=4
(c)
N: number of shear band
Critical energy (J/m^2)
300
200
100
0
0.00
0.01
0.02
0.03
0.04
0.05
True strain

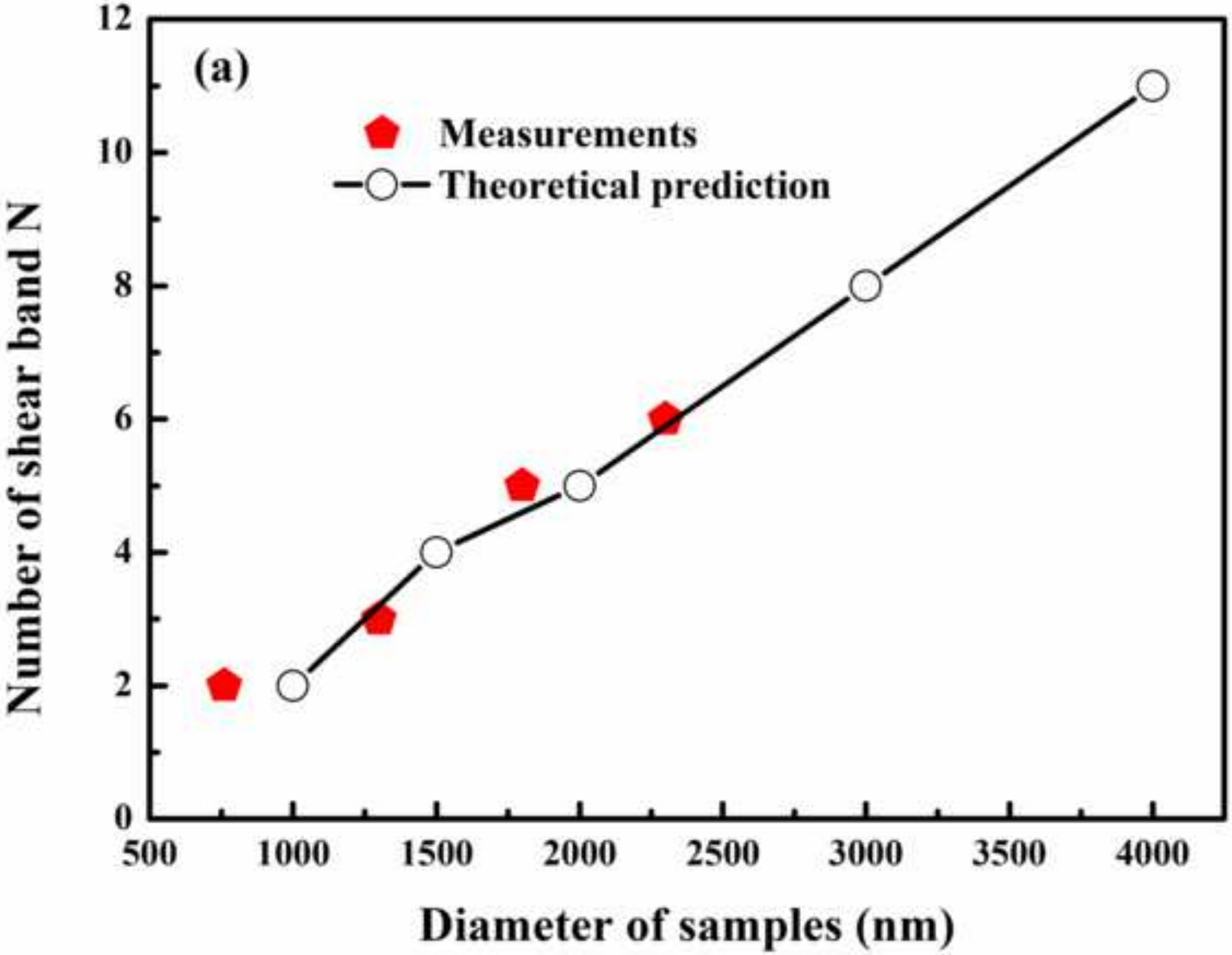
(a)
Measurements
Theoretical prediction
Number of shear band N
Diameter of samples (nm)
0
2
4
6
8
10
12
500
1000
1500
2000
2500
3000
3500
4000

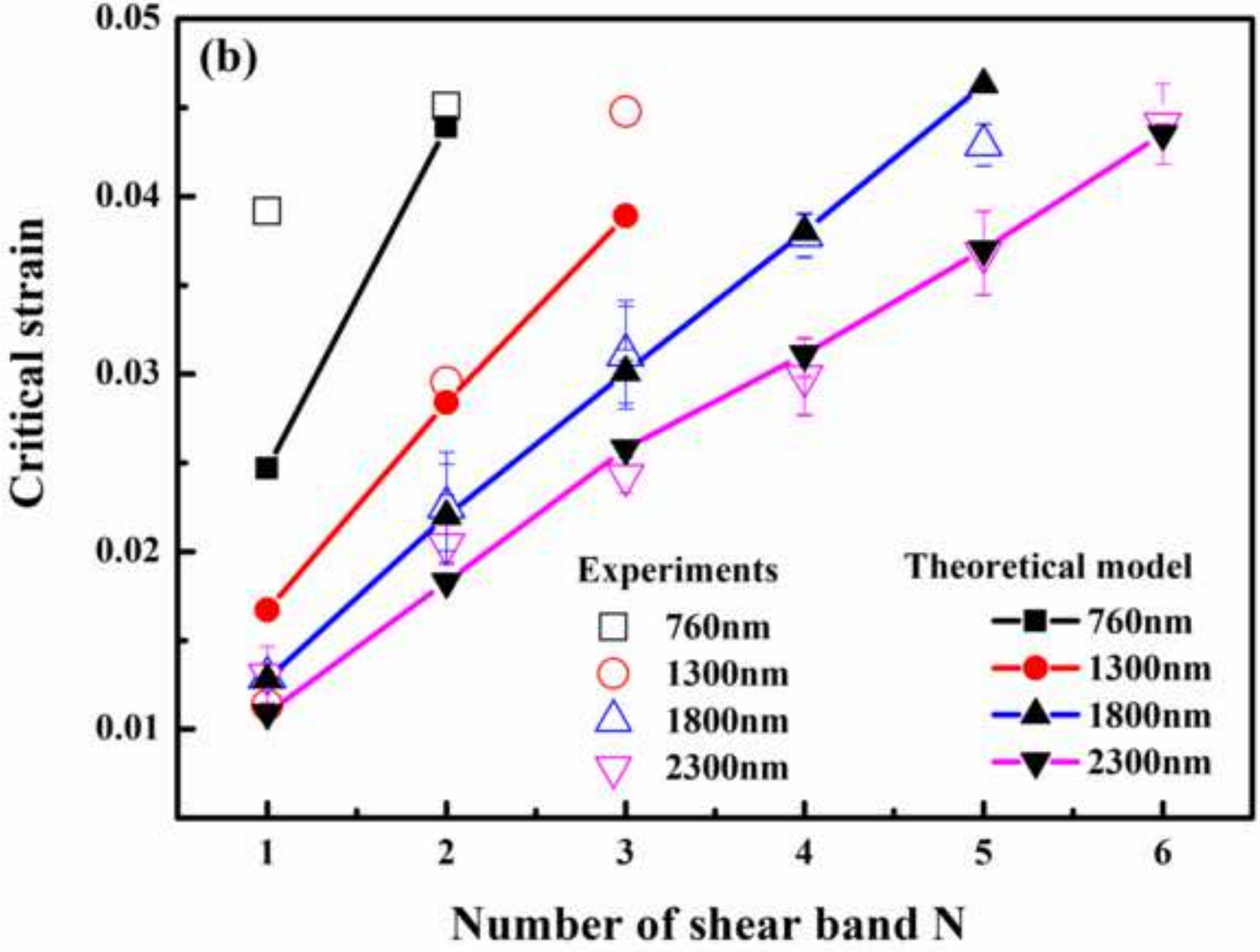
(b)
Critical strain
0.05
0.04
0.03
0.02
0.01
1
2
3
4
5
6
Number of shear band N
Experiments
□ 760nm
○ 1300nm
△ 1800nm
▽ 2300nm
Theoretical model
■ 760nm
● 1300nm
▲ 1800nm
▼ 2300nm

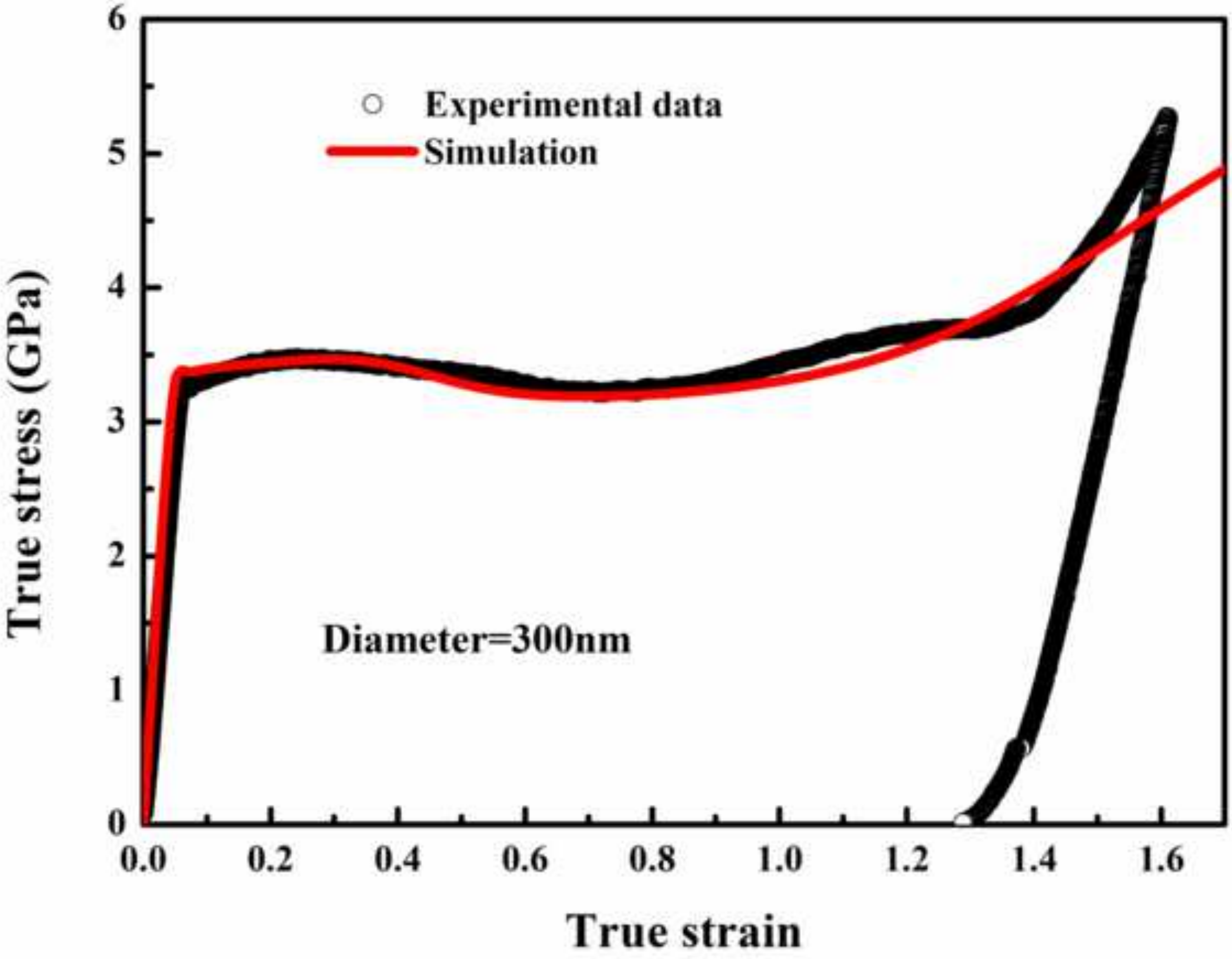
Experimental data
Simulation
Diameter=300nm
True stress (GPa)
True strain
0
1
2
3
4
5
6
0.0
0.2
0.4
0.6
0.8
1.0
1.2
1.4
1.6

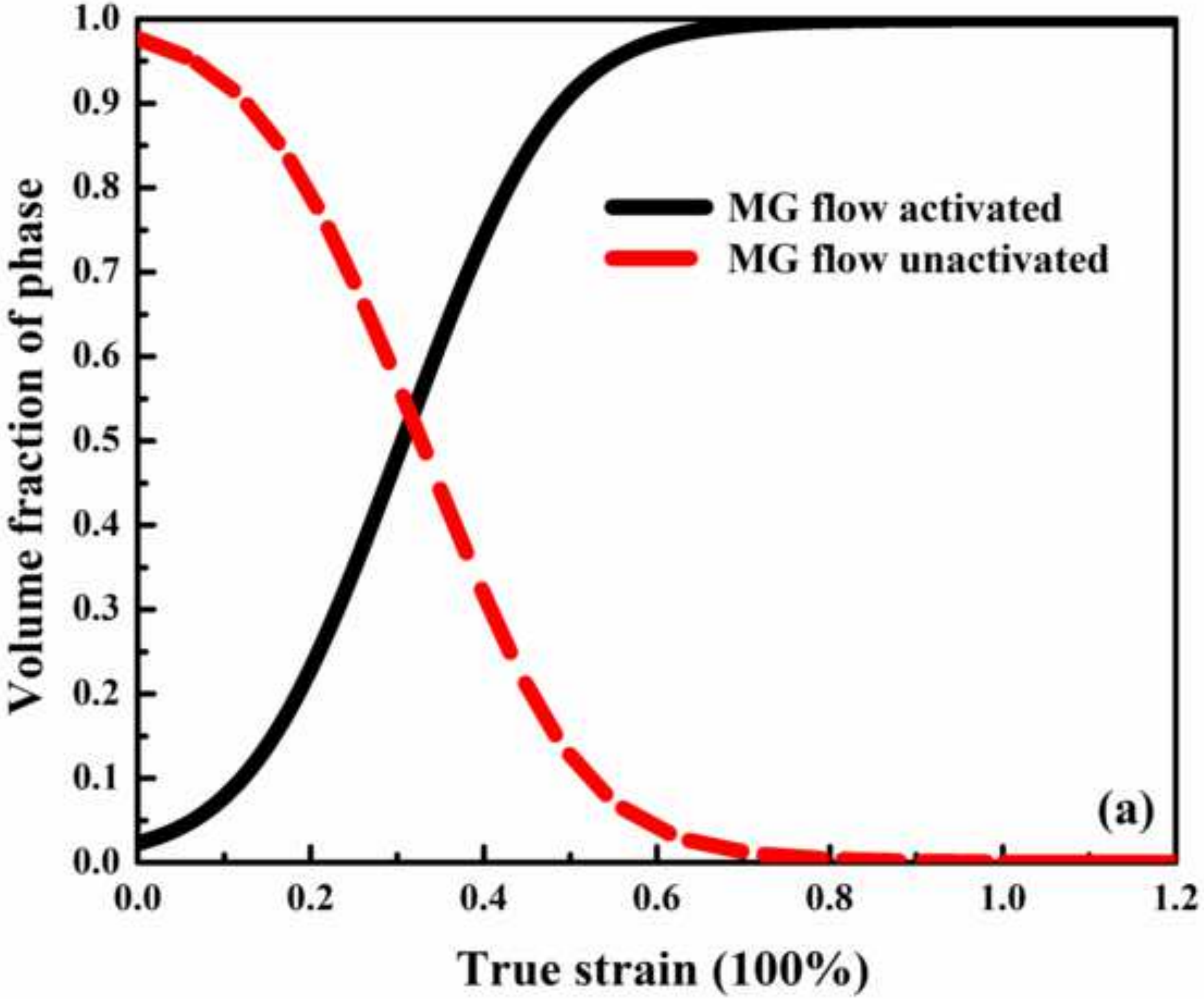
1.0
0.9
0.8
0.7
0.6
0.5
0.4
0.3
0.2
0.1
0.0
Volume fraction of phase
0.0
0.2
0.4
0.6
0.8
1.0
1.2
True strain (100%)
MG flow activated
MG flow unactivated
(a)

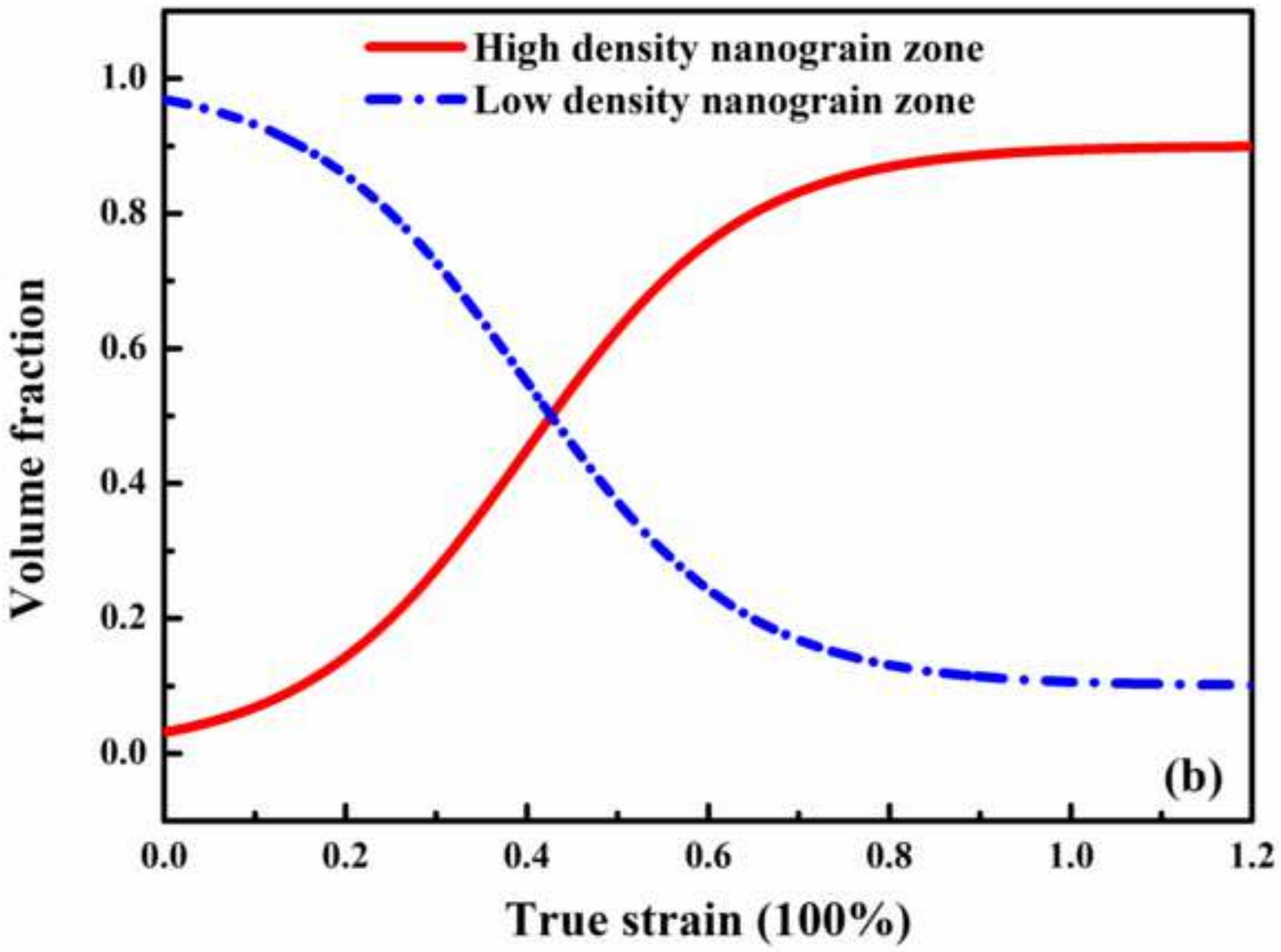
High density nanograin zone
Low density nanograin zone
Volume fraction
True strain (100%)
0.0
0.2
0.4
0.6
0.8
1.0
1.2
0.0
0.2
0.4
0.6
0.8
1.0
(b)

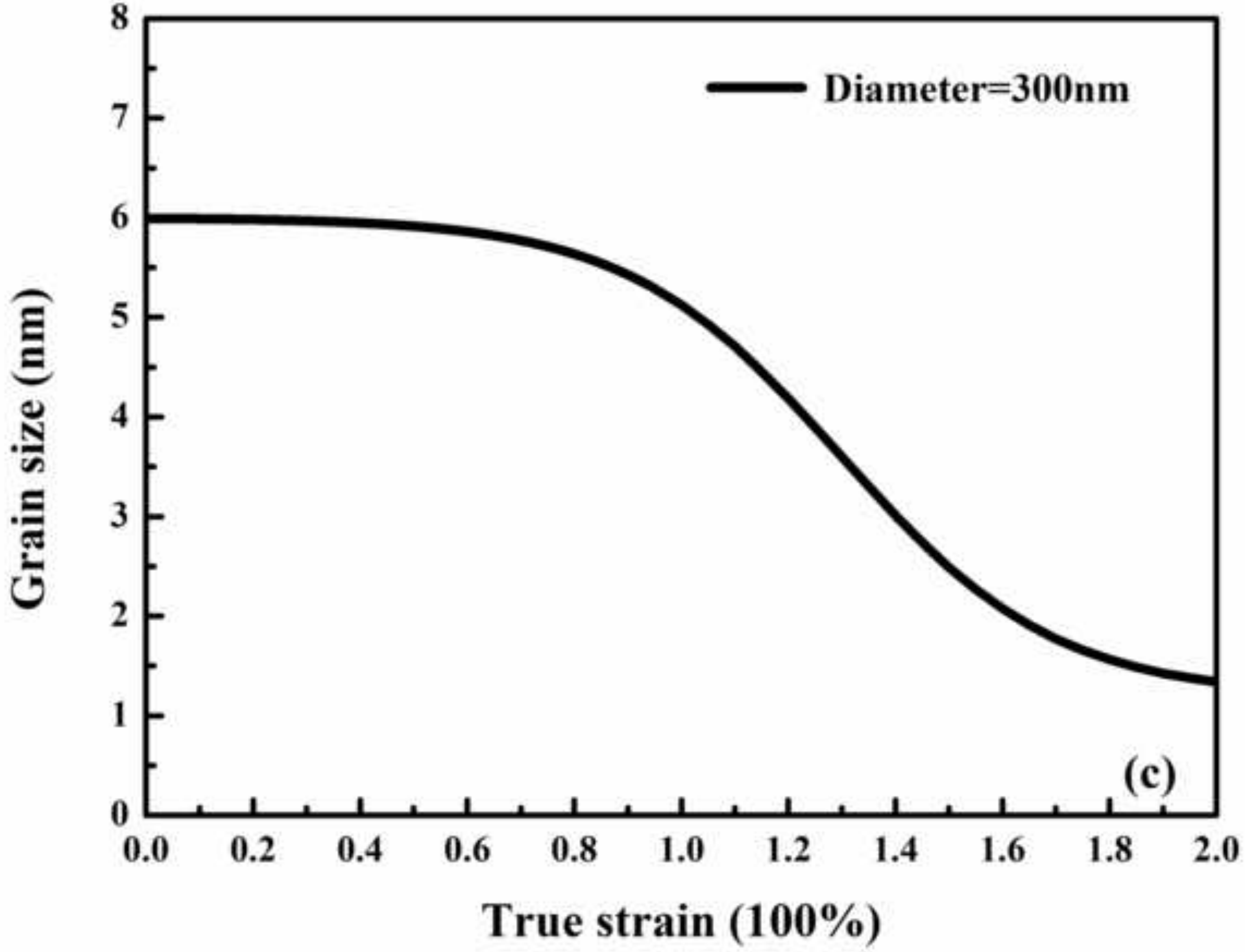
Grain size (nm)
0
1
2
3
4
5
6
7
8
True strain (100%)
0.0
0.2
0.4
0.6
0.8
1.0
1.2
1.4
1.6
1.8
2.0
Diameter=300nm
(c)

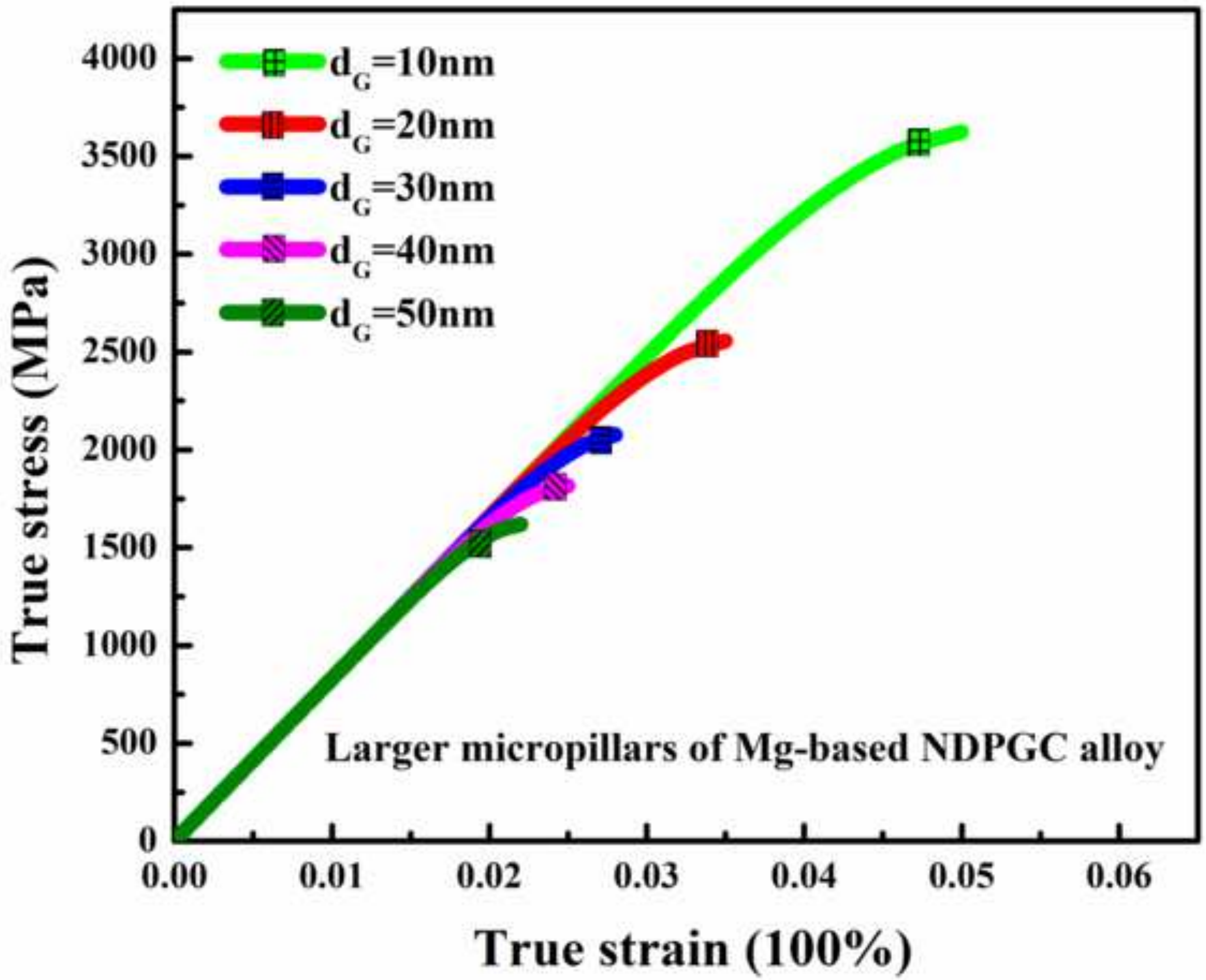
True stress (MPa)
4000
3500
3000
2500
2000
1500
1000
500
0
d_G=10nm
d_G=20nm
d_G=30nm
d_G=40nm
d_G=50nm
Larger micropillars of Mg-based NDPGC alloy
0.00
0.01
0.02
0.03
0.04
0.05
0.06
True strain (100%)

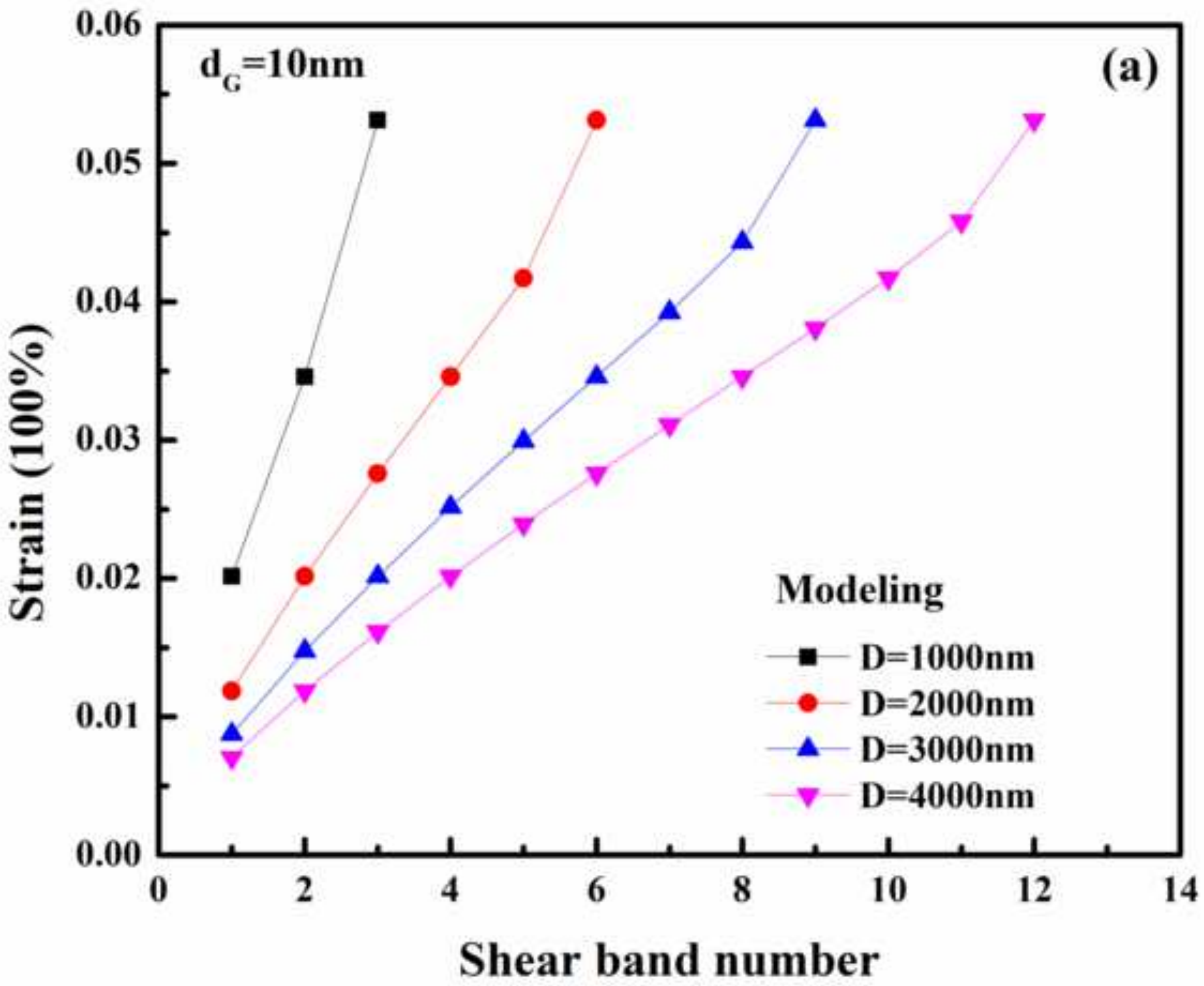

d$_G$=10nm
(a)
Strain (100%)
Shear band number
0.00
0.01
0.02
0.03
0.04
0.05
0.06
0
2
4
6
8
10
12
14
Modeling
D=1000nm
D=2000nm
D=3000nm
D=4000nm

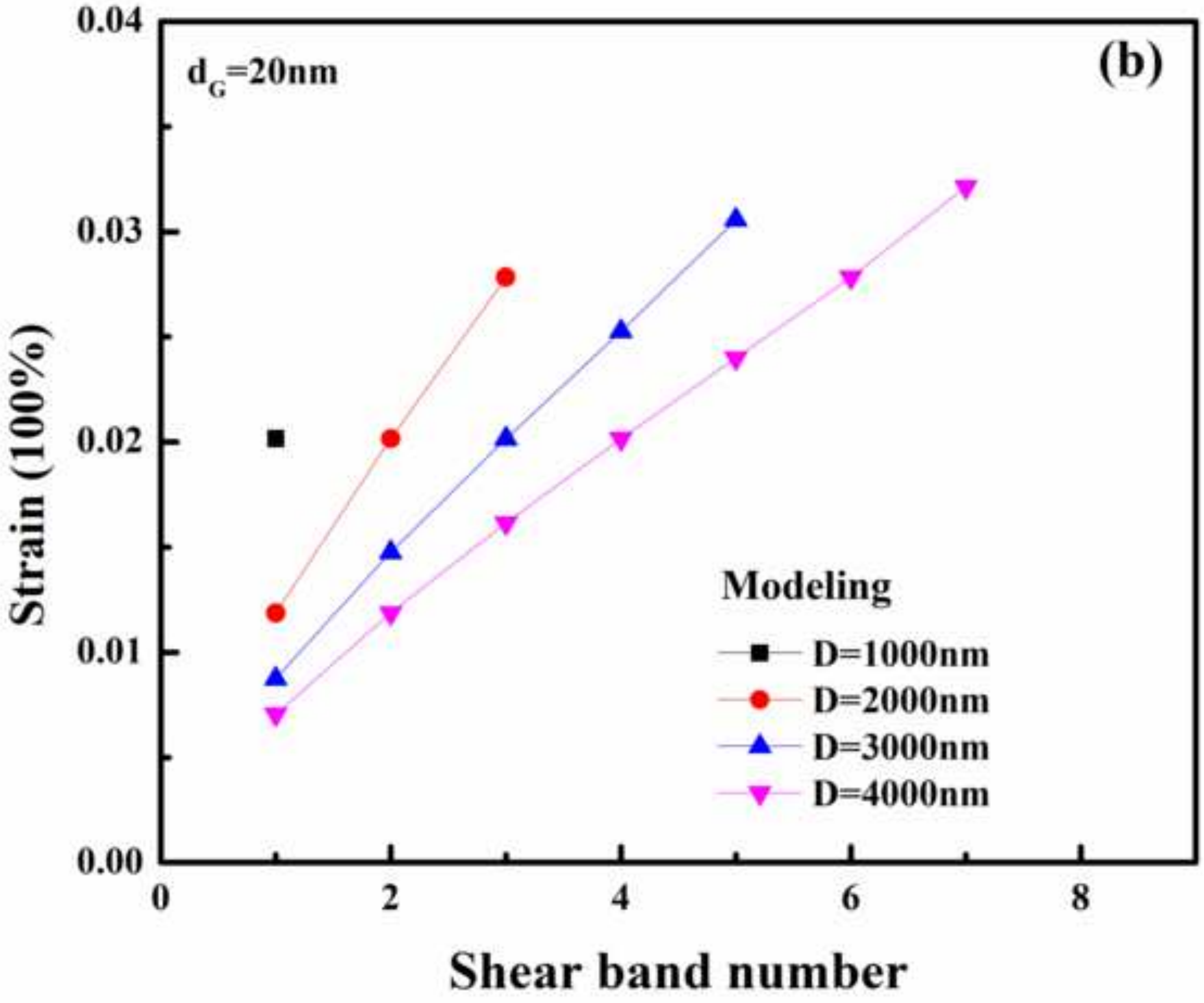
d$_G$=20nm
(b)
Strain (100%)
0.04
0.03
0.02
0.01
0.00
0
2
4
6
8
Shear band number
Modeling
D=1000nm
D=2000nm
D=3000nm
D=4000nm

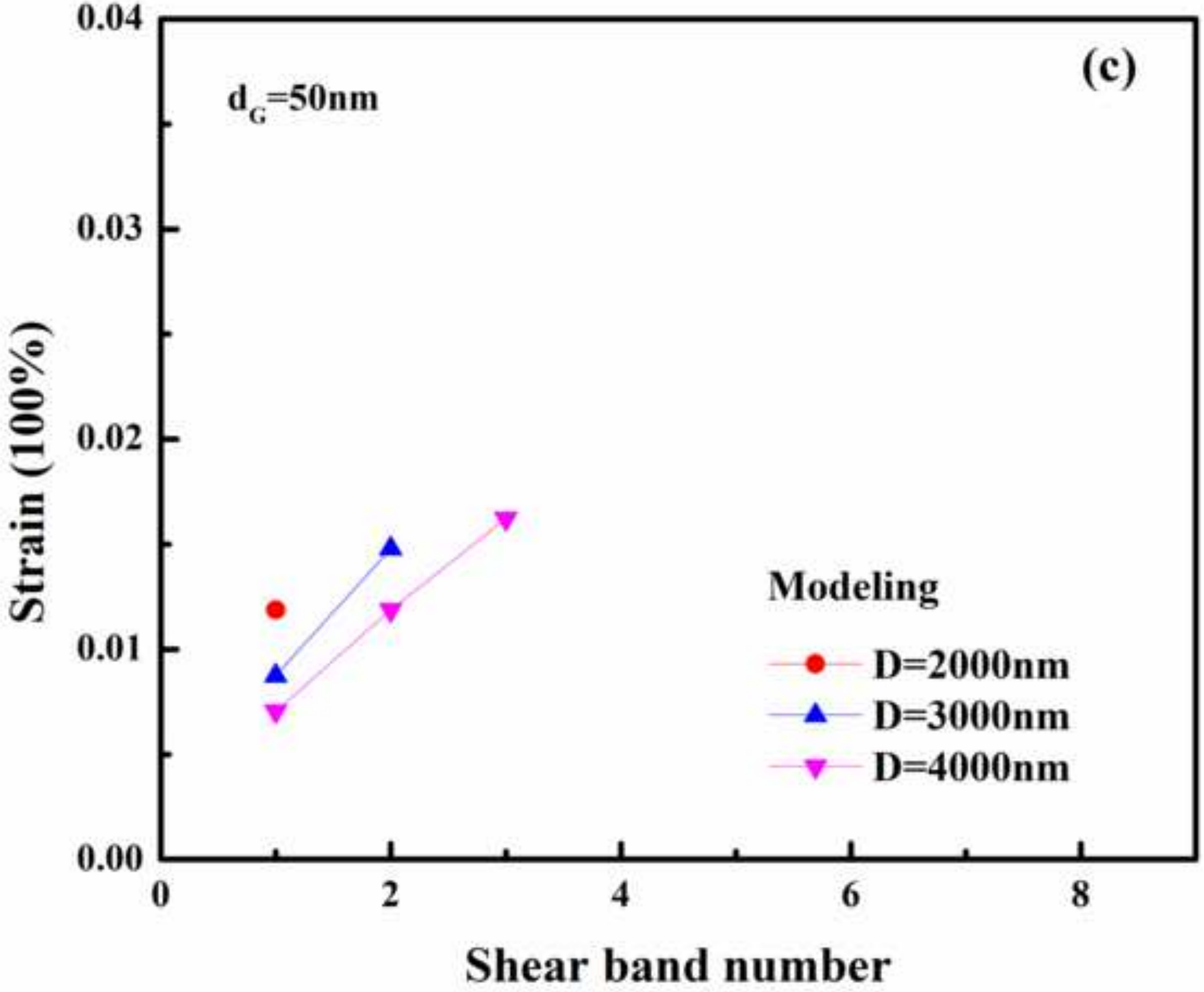

(c)
d_G=50nm
Strain (100%)
0.00
0.01
0.02
0.03
0.04
Shear band number
0
2
4
6
8
Modeling
D=2000nm
D=3000nm
D=4000nm

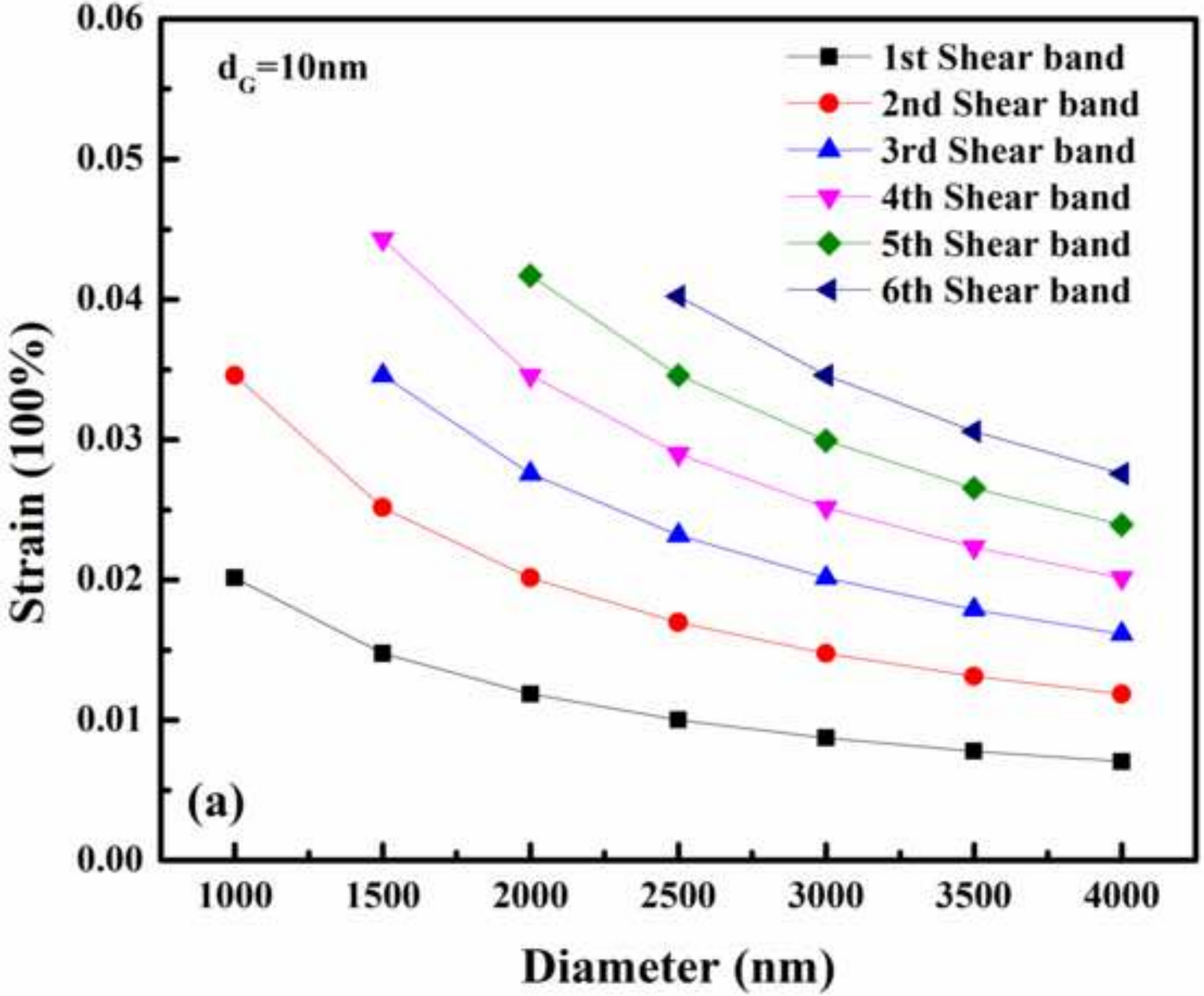
d_G=10nm
1st Shear band
2nd Shear band
3rd Shear band
4th Shear band
5th Shear band
6th Shear band
(a)
Strain (100%)
0.00
0.01
0.02
0.03
0.04
0.05
0.06
Diameter (nm)
1000
1500
2000
2500
3000
3500
4000

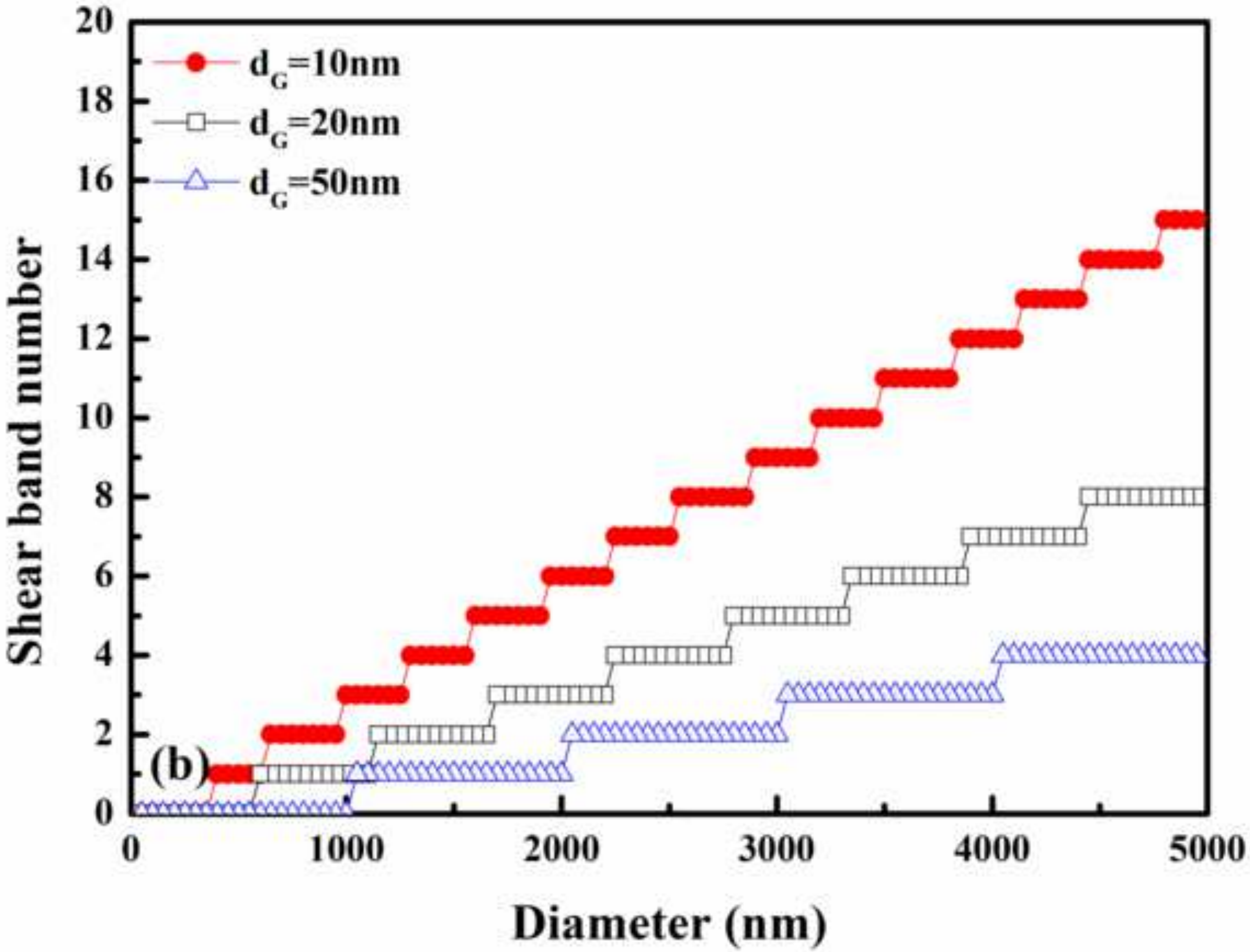

Shear band number
Diameter (nm)
0
2
4
6
8
10
12
14
16
18
20
0
1000
2000
3000
4000
5000
d_G=10nm
d_G=20nm
d_G=50nm
(b)

fig12c Click here to access/download;Figure;fig12c.tif

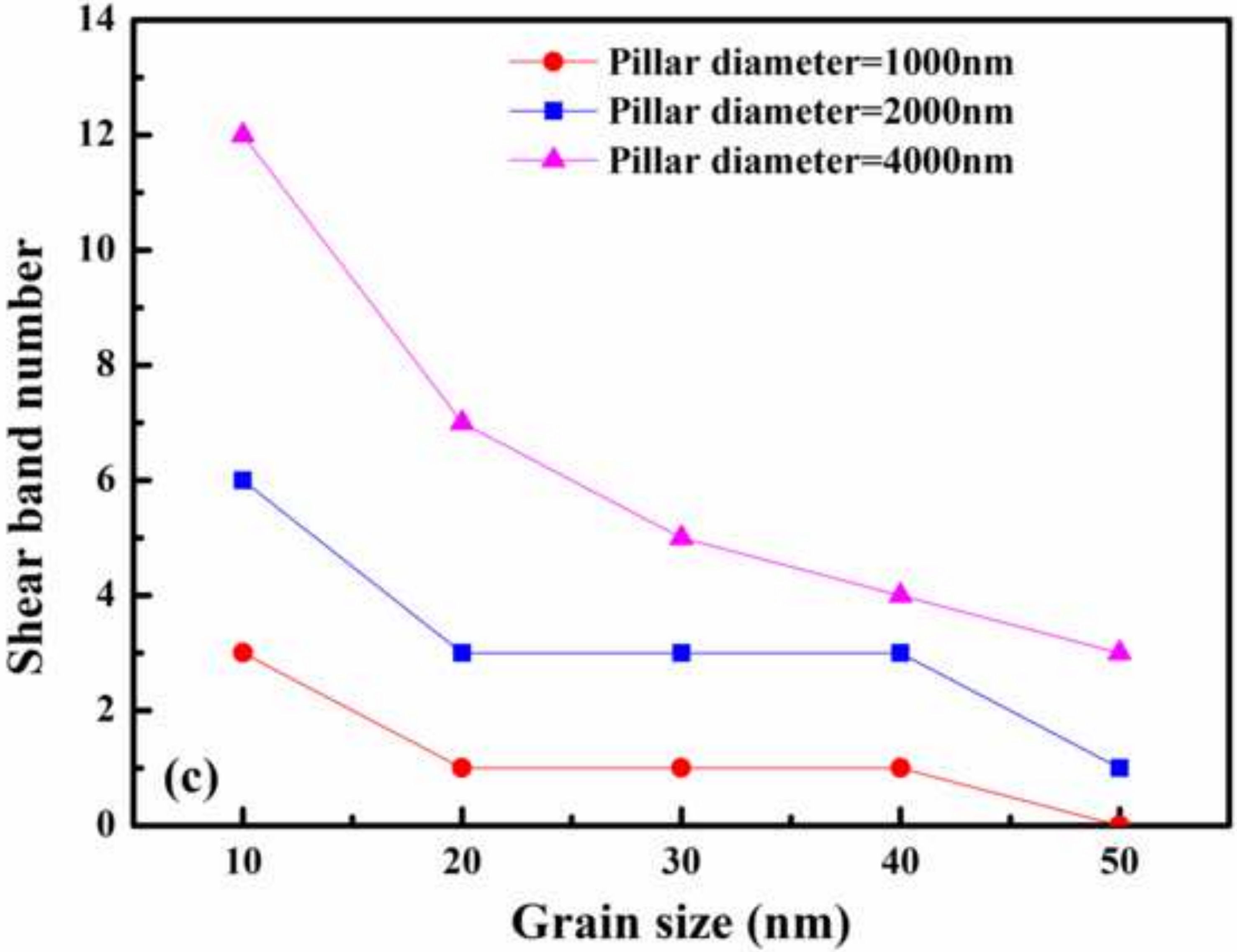

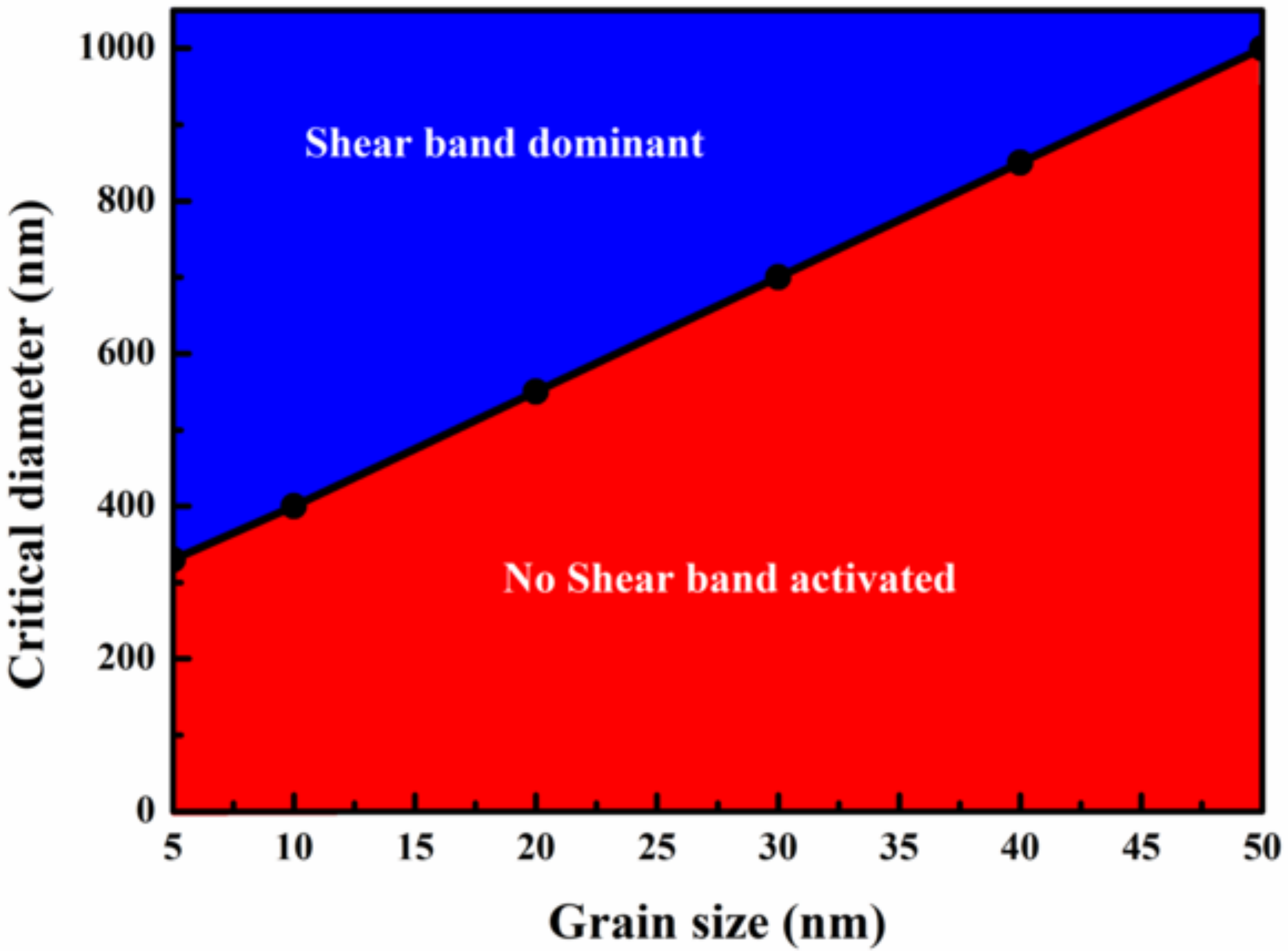
Shear band dominant
No Shear band activated
Critical diameter (nm)
0
200
400
600
800
1000
Grain size (nm)
5
10
15
20
25
30
35
40
45
50

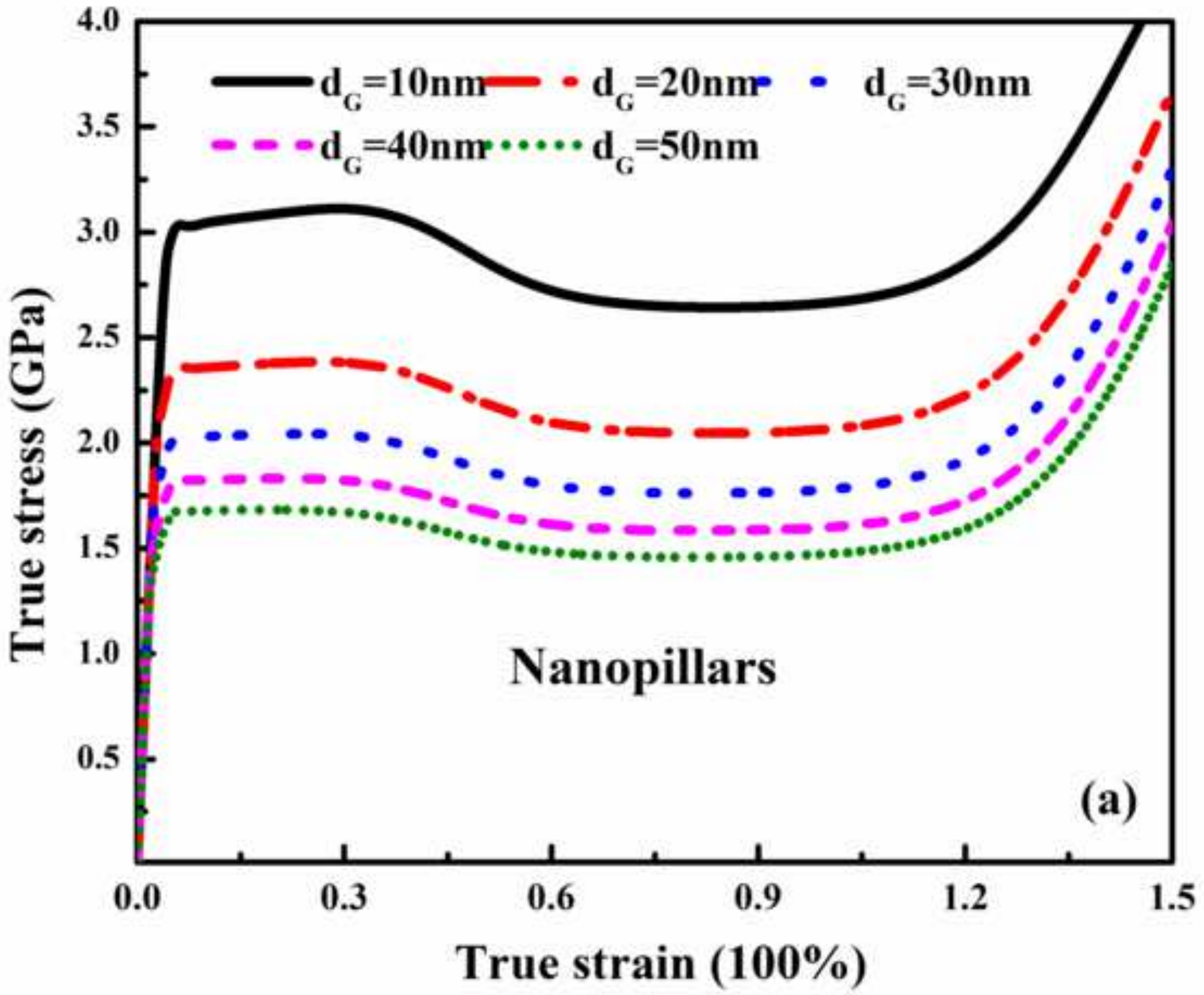

True stress (GPa)
4.0
3.5
3.0
2.5
2.0
1.5
1.0
0.5
0.0
0.3
0.6
0.9
1.2
1.5
True strain (100%)
d$_G$=10nm
d$_G$=20nm
d$_G$=30nm
d$_G$=40nm
d$_G$=50nm
Nanopillars
(a)

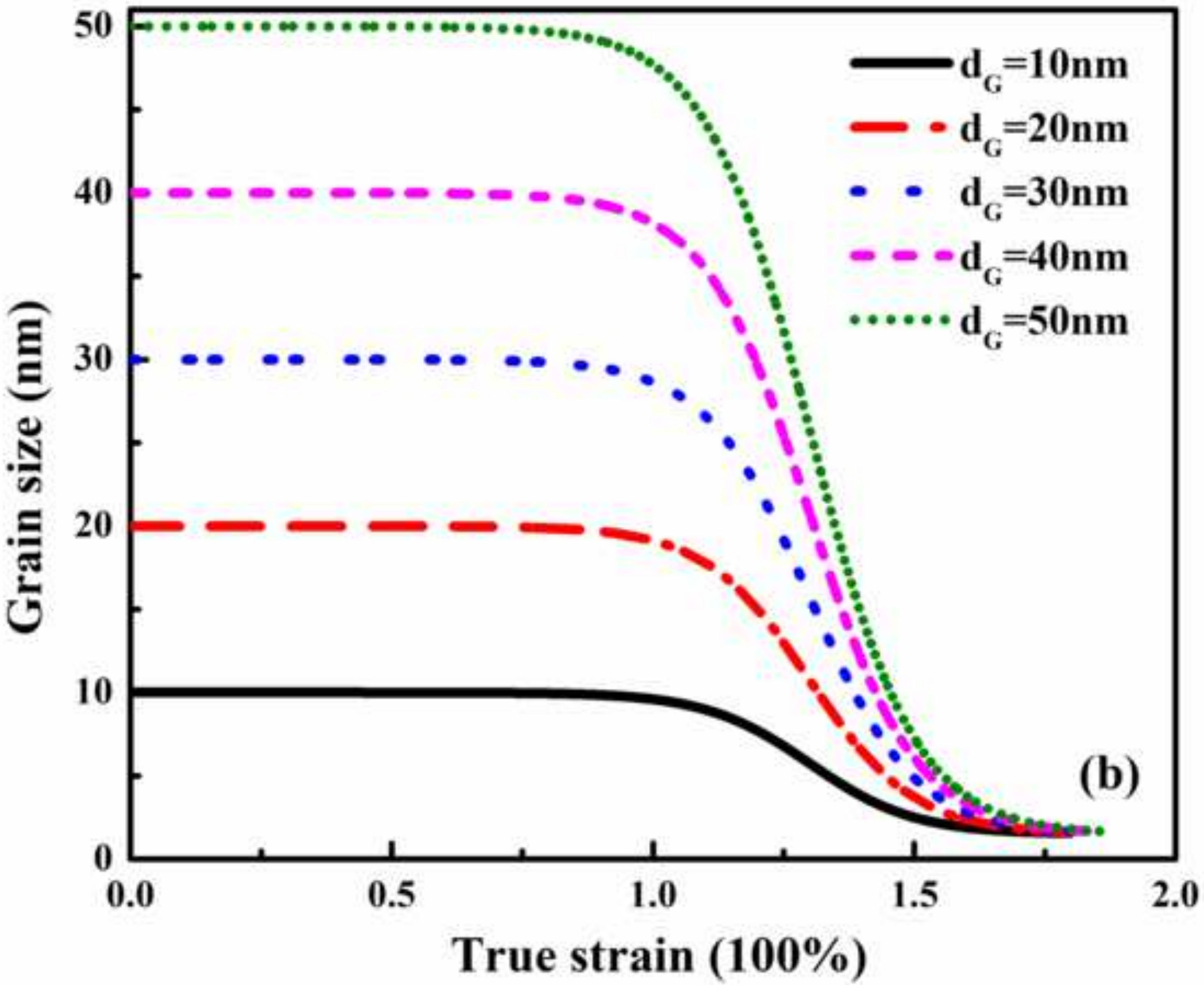
Grain size (nm)
True strain (100%)
0
10
20
30
40
50
0.0
0.5
1.0
1.5
2.0
d_G=10nm
d_G=20nm
d_G=30nm
d_G=40nm
d_G=50nm
(b)

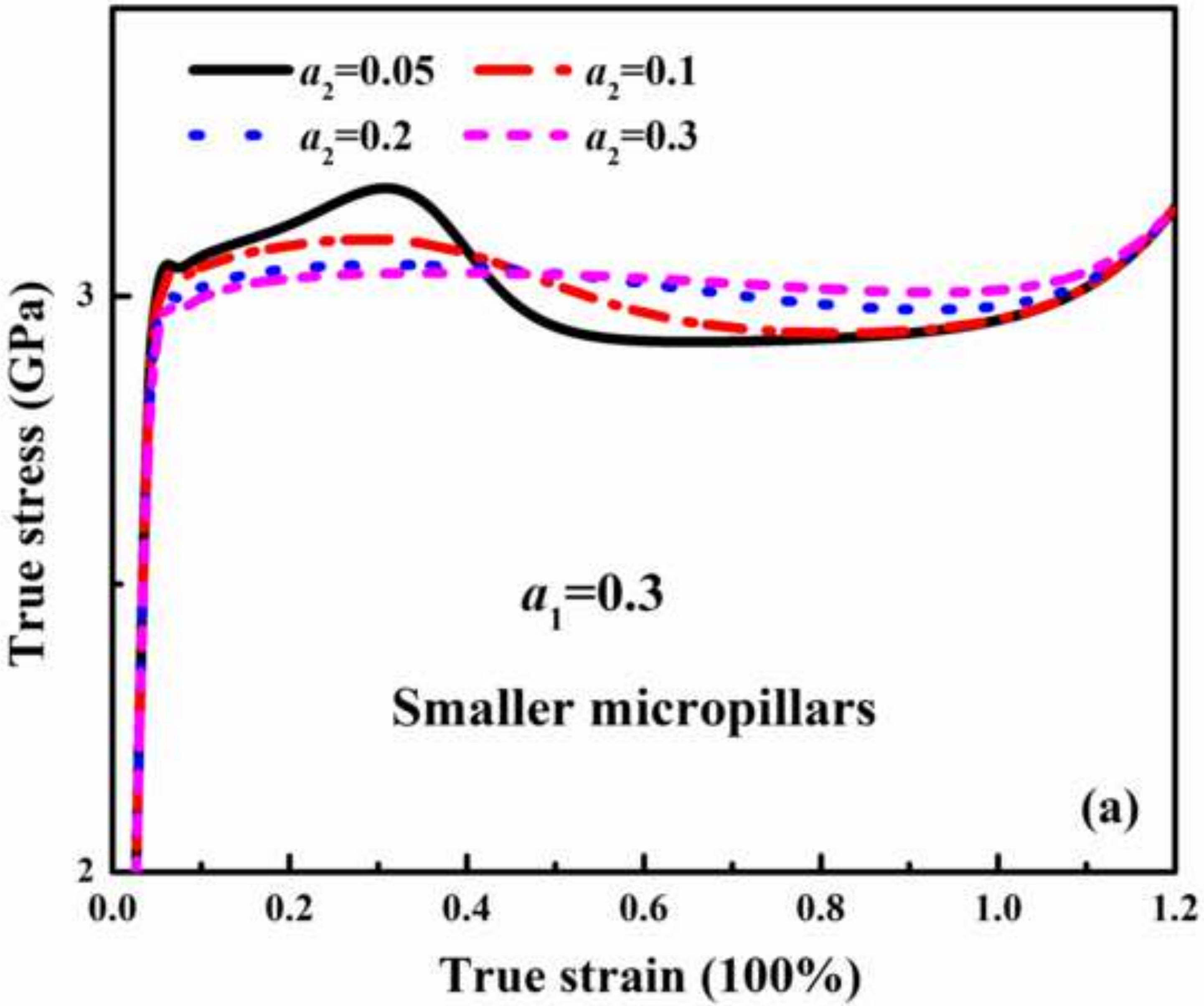
a_2=0.05
a_2=0.1
a_2=0.2
a_2=0.3
a_1=0.3
Smaller micropillars
(a)
True stress (GPa)
3
2
0.0
0.2
0.4
0.6
0.8
1.0
1.2
True strain (100%)

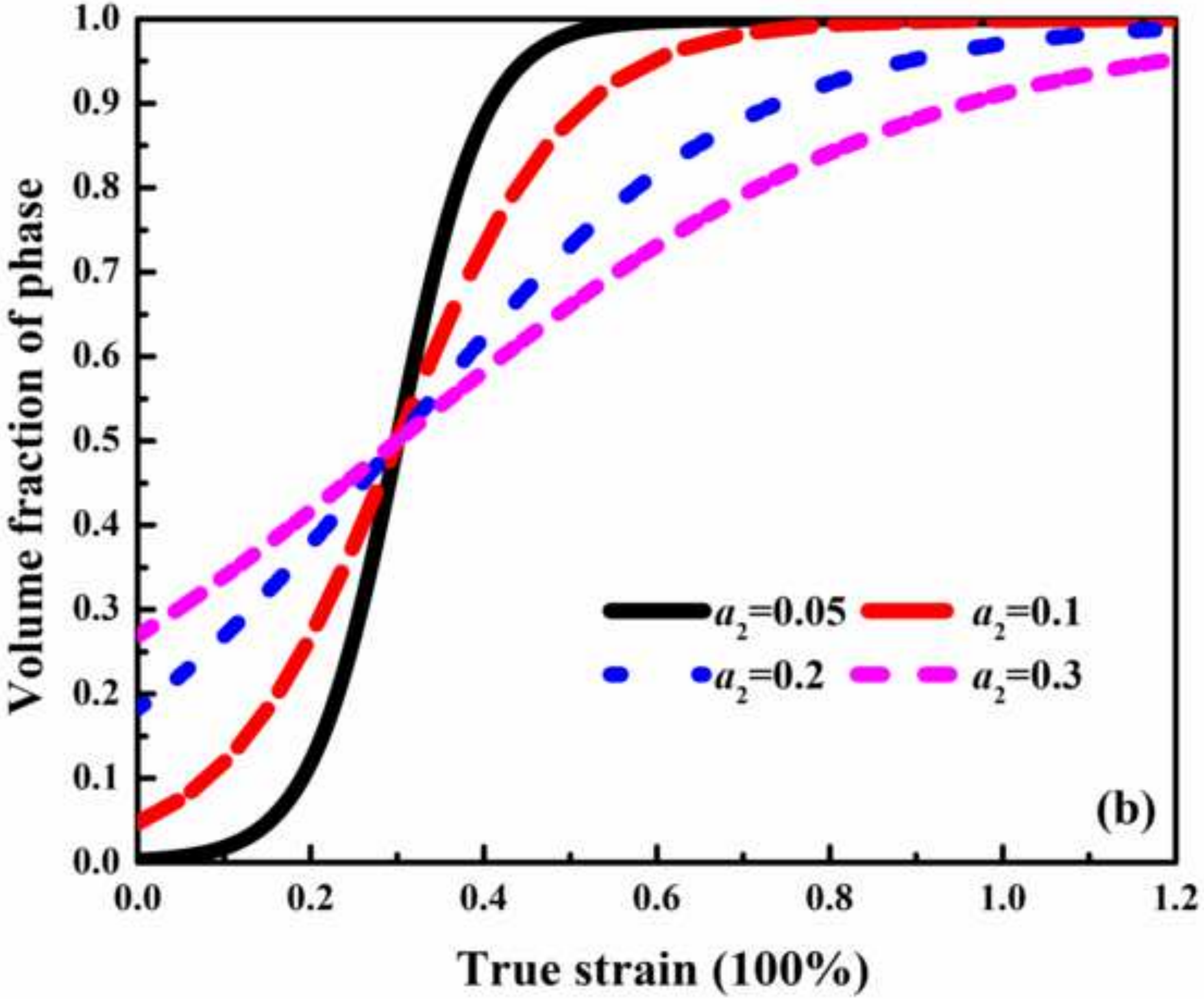
Volume fraction of phase
1.0
0.9
0.8
0.7
0.6
0.5
0.4
0.3
0.2
0.1
0.0
0.0
0.2
0.4
0.6
0.8
1.0
1.2
True strain (100%)
a_2=0.05
a_2=0.1
a_2=0.2
a_2=0.3
(b)

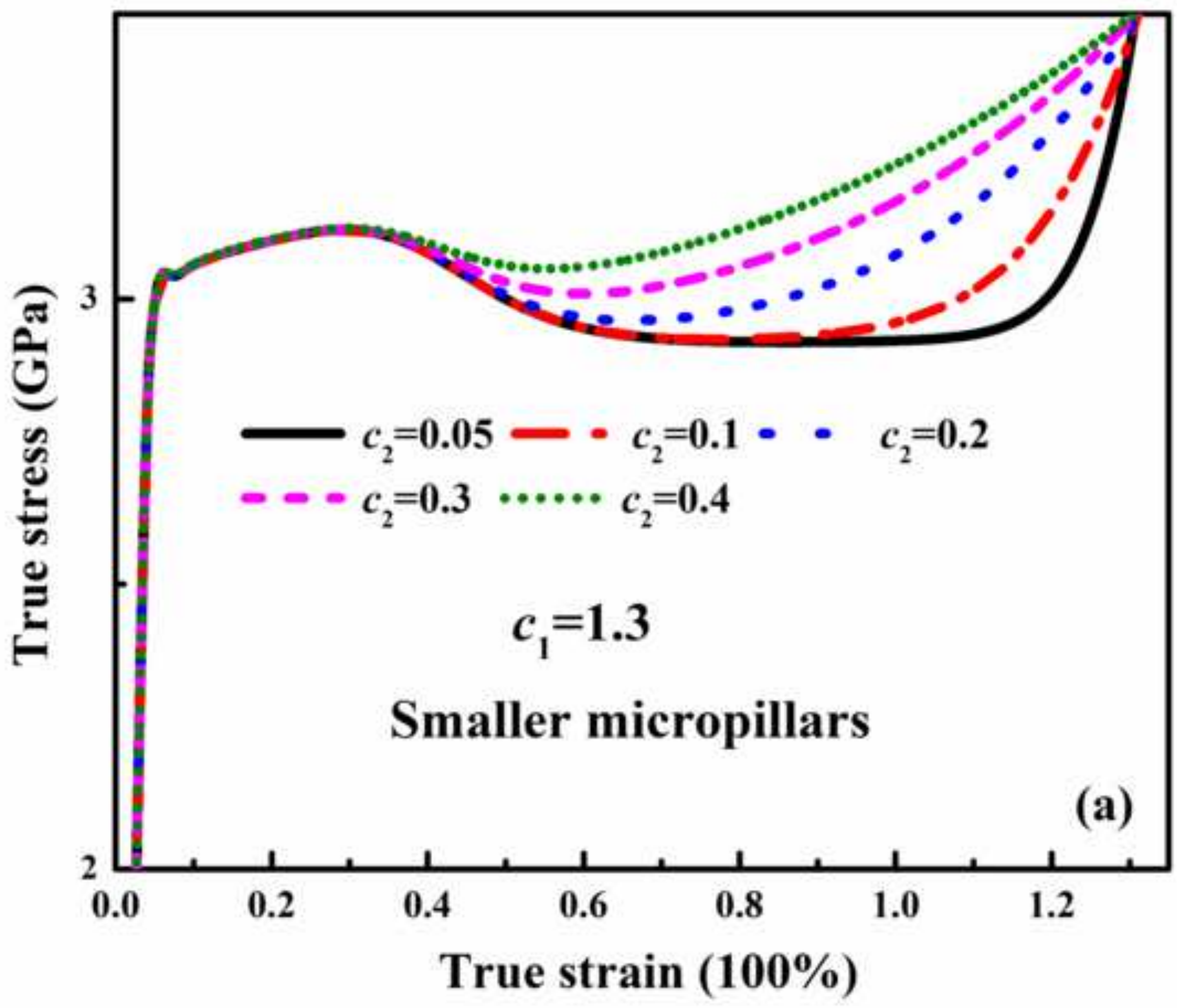
True stress (GPa)
3
2
0.0
0.2
0.4
0.6
0.8
1.0
1.2
True strain (100%)
c_2=0.05
c_2=0.1
c_2=0.2
c_2=0.3
c_2=0.4
c_1=1.3
Smaller micropillars
(a)

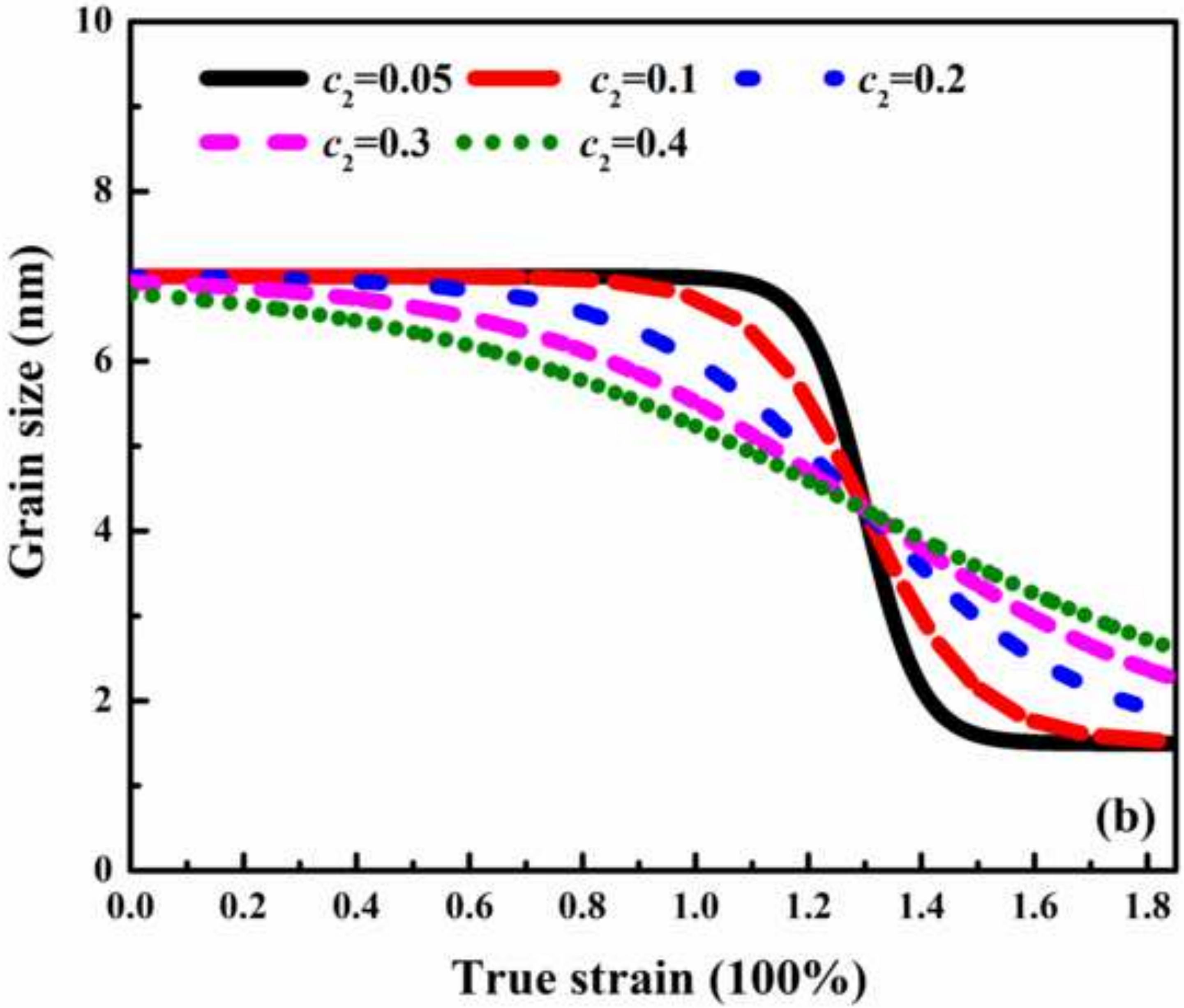

c_2=0.05
c_2=0.1
c_2=0.2
c_2=0.3
c_2=0.4
Grain size (nm)
True strain (100%)
0
2
4
6
8
10
0.0
0.2
0.4
0.6
0.8
1.0
1.2
1.4
1.6
1.8
(b)